2022

# Magnetic and Mechanical Properties of Ultrasoft Magnetorheological Elastomers

Andy T. Clark

**Magnetic and Mechanical Properties of Ultrasoft Magnetorheological Elastomers**

by Andy T. Clark

2022

Submitted to the Faculty of Bryn Mawr College
in partial fulfillment of the requirements for
the degree of Doctor of Philosophy
in the Department of Physics

Doctoral Committee:

Xuemei Cheng, Advisor
Kathryne Daniel
Michael Noel
Michael Schulz

ORCID iD: https://orcid.org/0000-0002-5758-257X

## Abstract

Magnetorheological elastomers (MREs), composite materials consisting of magnetic particles embedded in a non-magnetic elastomeric matrix, can reversibly modulate their mechanical and magnetic properties through tuning the applied magnetic field *H*. Recently, ultrasoft MREs have received tremendous attention due to their great potential in biomedical applications. However, the effects of the polymer stiffness and magnetic particle concentration on the magnetic and mechanical properties of ultrasoft MREs still need to be better understood. In this dissertation, the author presents a comprehensive investigation of the magnetic and mechanical properties of ultrasoft MREs as well as their biomedical applications.

The effect of polymer stiffness on magnetization reversal of MREs has been investigated using a combination of magnetometry measurements and computational modeling. The magnetic hysteresis loops of the softer MREs exhibit a characteristic pinched loop shape with almost zero remanence and loop widening at intermediate fields that monotonically decreases with increasing polymer stiffness. A two-dipole model that incorporates magneto-mechanical coupling not only confirms that micron-scale particle motion along the applied magnetic field direction plays a defining role in the magnetic hysteresis but also reproduces the observed loop shapes and widening trends for MREs with varying polymer stiffnesses.

Measurements of the moduli and surface roughness of ultrasoft MREs at various $H$'s reveal a sensitive dependence on the magnetic particle concentration $\Phi$ and $H$. As $\Phi$ increases from 0 to 23%, ultrasoft MREs at $H = 95.5$ kA/m (1200 Oe) show an increase of $\approx 41\times, 11\times, \text{and } 11\times$ in their shear storage, Young's modulus, and surface roughness, respectively. The moduli and surface roughness can be fit to quadratic functions of $\Phi$ and $H$.

The presented magnetic and mechanical properties of ultrasoft MREs provides the framework for applying the MREs as dynamic platforms in biomedical engineering. Ultrasoft MREs have been applied to investigate the response of cells to 2D and 3D dynamic mechanical stimuli. Furthermore, the field-dependent particle motion observed in ultrasoft MREs has inspired an application for creating 3D heterogeneous cellular gradients.

This work was performed under the guidance of the author's thesis advisor, Professor Xuemei Cheng.

## Dedication

To my incredible parents for their unconditional love, support, and guidance.

## Acknowledgements

I would like to first thank my thesis advisor, Professor Xuemei "May" Cheng, who has played an integral role in my graduate education, research, and completion of this work. She is an incredible physicist, and I am deeply grateful for her guidance along with the countless research opportunities that she has generated for me over the years. These will not just be experiences and skills I take with me, but memories I will cherish for a lifetime.

I am very thankful for the collaborations and invaluable help I received from Professor Kristen Buchanan, Professor Elise Corbin, and Dr. Alexander Bennett. It has also been wonderful collaborating with fellow graduate students: David Marchfield, Zheng Cao, Hannah Zlotnick, Kiet Tran, Emile Kraus, JiaJia Li and Nan Tang as well as Bryn Mawr College undergraduate students: Halcyon Hu, Tori Dang, Mallory Yu, Georgia Nelson, Zhongying Yan, Vidya Ramaswamy, Lila Hernandez, Zainab Batool, Ralista Mihaylova and Cassie Wang. Many thanks to Richard Willard, Robert Cunningham and Dr. Paul Hintz for their help in creating custom equipment for this work, and their assistance in fixing equipment when things went awry.

I would like to thank all the faculty members from the Department of Physics for their help along the way: Professor Peter Beckmann, Professor Katheryn Daniel, Professor Mark Matlin, Professor Michael Noel, Professor David Schaffner, and Professor Michael Schulz along with Professor Djordje Milićević from the Department of Mathematics for chairing my dissertation committee. To my fellow Bryn Mawr graduate students: Dr. Xiao

Wang, Carlos Cartagena-Sanchez, Hayley Johnson, Olivia McAuley, Amy Smock, Tyler DeMan, Joshua Carlson, Sarah Spielman, Cassandra Gates, Dr. Ziva Myer, and Dr. Samantha Pezzimenti for their friendships. I also greatly appreciate the experience and friendships I gained during my time as a teaching assistant for the postbaccalaureate premedical program.

Some special thanks are in order. First, to my undergraduate research advisor Professor Matthew Waite for being a great mentor, providing research opportunities and well… just simply being you! Second, to Thomas J. Pizzillo for his leadership, innovation, and guidance in research and development during my time in industry. Third, to my high school physics teacher Mrs. Kathleen Linaugh for introducing me to my passion in life – physics.

Finally, to my friends and family who kept me grounded and supported me throughout this long journey. My dog Reece for keeping me company while writing this dissertation and lastly, but most importantly, my partner Ryan Copelin for being my rock and reminding me of the important things in life during tough times.

## Table of Contents

## List of Figures

## List of Tables

# Chapter 1: Introduction

Magnetorheological elastomers (MREs), also known as magnetoactive elastomers (MAEs), are composite materials that consist of a non-magnetic polymer matrix with embedded micro- or nano- sized magnetic particles [1]. Elastomers, which are a class of polymers, can stretch to high extensions and recover to their original dimensions upon removal of the applied stress [2]. The combination of the magnetic properties of the embedded particles and the mechanical properties of the elastomer enables tuning of the mechanical properties of MREs by changing the applied magnetic field [3]. In particular, the specific usage of magnetically soft ferromagnetic particles (e.g. carbonyl iron powder) allows for reversible modulation of the mechanical properties of MREs. The magnetic field-dependent mechanical properties, such as the elastic moduli [4–10] and surface roughness [11–14], make MREs ideal candidates for a wide range of applications in the automotive industry, construction, electronics, biology, medicine, robotics and so on [3].

Over the past few decades, rubber-like MREs with a base Young's modulus $E$ on the order of MPa have been extensively studied both experimentally [15] and theoretically [16]. Recently, ultrasoft MREs ($E$ ~ kPa) have attracted great interest because they offer an innovative and physiologically relevant approach to mimicking biophysical mechanical cues and regulators of cells *in vitro* [8–10]. Various *in vitro* platforms with material stiffnesses tuned by external stimuli such as the application of light [17], pH

modifications [18,19], temperature changes [20,21], and addition of biomolecules [22–24] have been developed in the past, but these platforms only offer permanent unidirectional changes in stiffness. While ultrasoft MREs have the unique advantage of reversible and repeated modulation of their elastic moduli through application of a magnetic field, they do not involve complicated polymer chemistries. The simplicity of MRE synthesis allows for easy fabrication in cell culture dishes for 2D platforms or even 3D platforms by using hydrogels containing both magnetic particles and living cells [8,25].

More excitingly, a recent study on ultrasoft MREs [8] has revealed much larger magnetic field-dependent increases in their mechanical properties in comparison to rubber-like MREs with similar magnetic particle concentrations at similar applied magnetic field strengths [15,16]. Furthermore, the magnetic hysteresis behavior of soft MREs with a characteristic pinched loop shape is distinctively different from that of stiffer MREs. Softer MREs have also been shown to exhibit magnetic field-dependent particle motion within the polymer matrix [26,27]. Previous reports have shown that varying polymer stiffness by composition [28] or temperature [29–31] affects the shape of the hysteresis loops, which has been speculated to arise from the immobilization of magnetic particles within the polymer matrix.

While ultrasoft MREs have been more extensively investigated recently, there are still many remaining questions about the magnetic and mechanical properties of ultrasoft MREs. For example, the temperature-dependent experiments to date [29–31] only examine two stiffnesses, and a more comprehensive examination of the effect of polymer stiffness and spacing of magnetic particles on the magnetization reversal of MREs that includes experiments and modeling is needed. Furthermore, there lacks a thorough investigation of

the effect of magnetic particle concentration on the magnetic field-dependent mechanical properties of ultrasoft MREs, hindering more widespread applications of ultrasoft MREs in biomedical engineering. Lastly, applications of ultrasoft MREs that demonstrate their capabilities of applying 2D and 3D dynamic mechanical stimuli to cells and how magnetic particle motion within MREs inspires a method for creating complex distributions of cells are needed.

This dissertation reports a comprehensive investigation of the magnetic and mechanical properties of ultrasoft MREs as well as the biomedical applications of ultrasoft MREs with the intention to address the above questions. The dissertation is organized as follows. Chapter 2 provides the theoretical background for the mechanical and magnetic properties of MREs. Chapter 3 starts with the synthesis of ultrasoft MREs and then focuses on the experimental methods for characterizing the magnetic and mechanical properties of the MREs. Chapter 4 is devoted to the effect of polymer stiffness and magnetic particle concentration on the magnetization reversal of MREs. Chapter 5 presents the magnetic field-dependent mechanical properties of ultrasoft MREs and chapter 6 discusses the biomedical applications of ultrasoft MREs along with a tissue regeneration application inspired by ultrasoft MREs. Finally, chapter 7 summarizes the main results of this dissertation.

**References for Chapter 1**


[1] S. Odenbach, *Microstructure and Rheology of Magnetic Hybrid Materials*, Archive of Applied Mechanics **86**, 269 (2016).

[2] R. J. Young and P. A. Lovell, *Introduction to Polymers* (CRC Press, Boca Raton, 2011).

[3] M. Arslan Hafeez, M. Usman, M. A. Umer, and A. Hanif, *Recent Progress in Isotropic Magnetorheological Elastomers and Their Properties: A Review*, Polymers **12**, 3023 (2020).
[4] M. R. Jolly, J. D. Carlson, B. C. Muñoz, and T. A. Bullions, *The Magnetoviscoelastic Response of Elastomer Composites Consisting of Ferrous Particles Embedded in a Polymer Matrix*, Journal of Intelligent Material Systems and Structures **7**, 613 (1996).
[5] G. Y. Zhou, *Shear Properties of a Magnetorheological Elastomer*, Smart Mater. Struct. **12**, 139 (2003).
[6] M. Lokander and B. Stenberg, *Improving the Magnetorheological Effect in Isotropic Magnetorheological Rubber Materials*, Polymer Testing **22**, 677 (2003).
[7] L. Chen, X. L. Gong, and W. H. Li, *Microstructures and Viscoelastic Properties of Anisotropic Magnetorheological Elastomers*, Smart Mater. Struct. **16**, 2645 (2007).
[8] M. Mayer, R. Rabindranath, J. Börner, E. Hörner, A. Bentz, J. Salgado, H. Han, H. Böse, J. Probst, M. Shamonin, G. J. Monkman, and G. Schlunck, *Ultra-Soft PDMS-Based Magnetoactive Elastomers as Dynamic Cell Culture Substrata*, PLoS ONE **8**, e76196 (2013).
[9] E. A. Corbin, A. Vite, E. G. Peyster, M. Bhoopalam, J. Brandimarto, X. Wang, A. I. Bennett, A. T. Clark, X. Cheng, K. T. Turner, K. Musunuru, and K. B. Margulies, *Tunable and Reversible Substrate Stiffness Reveals a Dynamic Mechanosensitivity of Cardiomyocytes*, ACS Appl. Mater. Interfaces **11**, 20603 (2019).
[10] K. A. Tran, E. Kraus, A. T. Clark, A. Bennett, K. Pogoda, X. Cheng, A. Cēbers, P. A. Janmey, and P. A. Galie, *Dynamic Tuning of Viscoelastic Hydrogels with Carbonyl Iron Microparticles Reveals the Rapid Response of Cells to Three-Dimensional Substrate Mechanics*, ACS Appl. Mater. Interfaces **13**, 20947 (2021).
[11] V. V. Sorokin, B. O. Sokolov, G. V. Stepanov, and E. Yu. Kramarenko, *Controllable Hydrophobicity of Magnetoactive Elastomer Coatings*, Journal of Magnetism and Magnetic Materials **459**, 268 (2018).
[12] G. Glavan, P. Salamon, I. A. Belyaeva, M. Shamonin, and I. Drevenšek-Olenik, *Tunable Surface Roughness and Wettability of a Soft Magnetoactive Elastomer*, Journal of Applied Polymer Science **135**, 46221 (2018).
[13] S. Chen, R. Li, X. Li, and X. Wang, *Magnetic Field Induced Surface Micro-Deformation of Magnetorheological Elastomers for Roughness Control*, Frontiers in Materials **5**, 76 (2018).
[14] G. Glavan, W. Kettl, A. Brunhuber, M. Shamonin, and I. Drevenšek-Olenik, *Effect of Material Composition on Tunable Surface Roughness of Magnetoactive Elastomers*, Polymers **11**, 594 (2019).
[15] A. K. Bastola and M. Hossain, *A Review on Magneto-Mechanical Characterizations of Magnetorheological Elastomers*, Composites Part B: Engineering **200**, 108348 (2020).
[16] M. A. Cantera, M. Behrooz, R. F. Gibson, and F. Gordaninejad, *Modeling of Magneto-Mechanical Response of Magnetorheological Elastomers (MRE) and MRE-Based Systems: A Review*, Smart Mater. Struct. **26**, 023001 (2017).
[17] M. Guvendiren and J. A. Burdick, *Stiffening Hydrogels to Probe Short- and Long-Term Cellular Responses to Dynamic Mechanics*, Nat Commun **3**, 792 (2012).

[18] H. Y. Yoshikawa, F. F. Rossetti, S. Kaufmann, T. Kaindl, J. Madsen, U. Engel, A. L. Lewis, S. P. Armes, and M. Tanaka, *Quantitative Evaluation of Mechanosensing of Cells on Dynamically Tunable Hydrogels*, J. Am. Chem. Soc. **133**, 1367 (2011).
[19] J. Kim and R. C. Hayward, *Mimicking Dynamic in Vivo Environments with Stimuli-Responsive Materials for Cell Culture*, Trends in Biotechnology **30**, 426 (2012).
[20] K. A. Davis, K. A. Burke, P. T. Mather, and J. H. Henderson, *Dynamic Cell Behavior on Shape Memory Polymer Substrates*, Biomaterials **32**, 2285 (2011).
[21] D. M. Le, K. Kulangara, A. F. Adler, K. W. Leong, and V. S. Ashby, *Dynamic Topographical Control of Mesenchymal Stem Cells by Culture on Responsive Poly(ϵ-Caprolactone) Surfaces*, Advanced Materials **23**, 3278 (2011).
[22] J. L. West and J. A. Hubbell, *Polymeric Biomaterials with Degradation Sites for Proteases Involved in Cell Migration*, Macromolecules **32**, 241 (1999).
[23] M. P. Lutolf, F. E. Weber, H. G. Schmoekel, J. C. Schense, T. Kohler, R. Müller, and J. A. Hubbell, *Repair of Bone Defects Using Synthetic Mimetics of Collagenous Extracellular Matrices*, Nature Biotechnology **21**, 513 (2003).
[24] K. S. Straley and S. C. Heilshorn, *Dynamic, 3D-Pattern Formation Within Enzyme-Responsive Hydrogels*, Adv. Mater. **21**, 4148 (2009).
[25] Z. Liu, J. Liu, X. Cui, X. Wang, L. Zhang, and P. Tang, *Recent Advances on Magnetic Sensitive Hydrogels in Tissue Engineering*, Front. Chem. **8**, 124 (2020).
[26] T. Gundermann and S. Odenbach, *Investigation of the Motion of Particles in Magnetorheological Elastomers by X-μCT*, Smart Mater. Struct. **23**, 105013 (2014).
[27] G. Pessot, M. Schümann, T. Gundermann, S. Odenbach, H. Löwen, and A. M. Menzel, *Tunable Dynamic Moduli of Magnetic Elastomers: From Characterization by x-Ray Micro-Computed Tomography to Mesoscopic Modeling*, J. Phys.: Condens. Matter **30**, 125101 (2018).
[28] G. V. Stepanov, D. Y. Borin, Y. L. Raikher, P. V. Melenev, and N. S. Perov, *Motion of Ferroparticles inside the Polymeric Matrix in Magnetoactive Elastomers*, J. Phys.: Condens. Matter **20**, 204121 (2008).
[29] A. V. Bodnaruk, A. Brunhuber, V. M. Kalita, M. M. Kulyk, A. A. Snarskii, A. F. Lozenko, S. M. Ryabchenko, and M. Shamonin, *Temperature-Dependent Magnetic Properties of a Magnetoactive Elastomer: Immobilization of the Soft-Magnetic Filler*, Journal of Applied Physics **123**, 115118 (2018).
[30] A. V. Bodnaruk, A. Brunhuber, V. M. Kalita, M. M. Kulyk, P. Kurzweil, A. A. Snarskii, A. F. Lozenko, S. M. Ryabchenko, and M. Shamonin, *Magnetic Anisotropy in Magnetoactive Elastomers, Enabled by Matrix Elasticity*, Polymer **162**, 63 (2019).
[31] A. V. Bodnaruk, V. M. Kalita, M. M. Kulyk, A. F. Lozenko, S. M. Ryabchenko, A. A. Snarskii, A. Brunhuber, and M. Shamonin, *Temperature Blocking and Magnetization of Magnetoactive Elastomers*, Journal of Magnetism and Magnetic Materials **471**, 464 (2019).

# Chapter 2: Fundamentals of MREs

## 2.1 Introduction

MREs are composite materials with interestingly coupled magnetic and mechanical properties. **Figure 2-1** shows a photograph of an MRE and its microstructure consisting of a polymer with embedded magnetic microparticles. Various types of polymers and magnetic particles can be used to synthesize MREs with desired magnetic and mechanical properties. Typically, micron-sized magnetically soft ferromagnetic particles (e.g. carbonyl iron powder) are used in MREs due to their low remanence, and almost zero coercivity, which provide MREs with reversible magnetic field-dependent mechanical properties. The

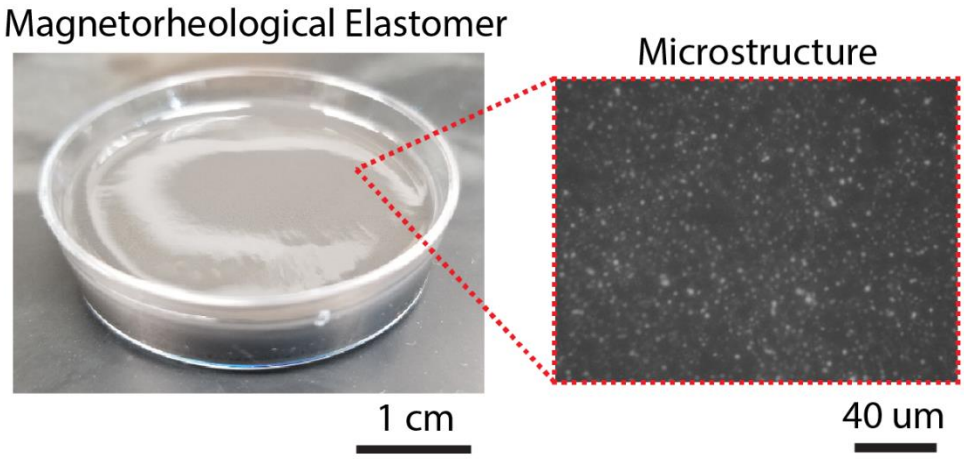


**Figure 2-1** A photograph of an MRE and an optical microscopy image of its microstructure, which is consists of a polymer with embedded magnetic microparticles.

viscoelastic properties of the polymer play a defining role in the zero-field mechanical properties of MREs. In particular, MREs synthesized with ultrasoft polymers have elastic moduli of just a few kPa, which is physiologically relevant to a wide range of biological systems. Investigating the magnetic field-dependent properties of ultrasoft MREs requires a detailed understanding of the viscoelastic properties of the polymer and the magnetic properties of the embedded particles.

This chapter first presents a general description of polymers and their mechanical properties in section 2.2. Next, an overview of magnetic materials and magnetism is presented in section 2.3. The magnetic properties of iron microparticles are presented in section 2.4. Finally, section 2.5 focuses on the magneto-mechanical coupling in MREs.

## 2.2 Polymers

**"**Polymer" is derived from the Greek words "poly" and "mer", which mean "many, much" and "part, segment" respectively. A polymer consists of molecular chains with long sequences of atoms that are usually connected by covalent chemical bonds [1]. These molecular chains can be cross-linked to form a large-scale 3D network through a chemical reaction known as polymerization. The average distance between cross-links, often referred to as the mesh size, ranges typically from a few nanometers to tens of nanometers [2]. The entanglement of these molecular chains, like a bowl of cooked spaghetti, gives polymers unique mechanical properties.

There are natural polymers [3], such as proteins, cellulose, silk, and deoxyribonucleic acid (DNA), or synthetic polymers [4], such as polydimethylsiloxane (PDMS), polystyrene, and polyethylene. While polymers are often classified into three

groups: elastomers, thermoplastics, and thermosets, this dissertation focuses on elastomers. Elastomers, such as rubber bands, are polymers that can stretch to high extensions (e.g. $3-10\times$ their original dimensions) and recover to their original dimensions when the applied load is removed [1]. In particular, this dissertation investigates a special type of elastomer, polydimethylsiloxane (PDMS), due to its excellent biocompatibility, commercial availability as a two-part resin (liquid state), ease of synthesis, room temperature vulcanization, insensitivity to temperature variations around room temperature and wide range in stiffnesses [5–7].

### 2.2.1 Tuning Stiffness of PDMS

A key benefit of using PDMS as the elastomer in MREs studied in this dissertation is its wide range in stiffness. For example, ultrasoft Sylgard™ 527 has a stiffness similar to tofu [8], while Sylgard™ 184 is stiff like rubber. Though the exact composition of Sylgard™ 527 and Sylgard™ 184 is proprietary, the main difference between the two is the inclusion of silica nanoparticles in Sylgard™ 184, which adds mechanical rigidity [9]. These two types of PDMS can be blended to synthesize elastomers with stiffnesses ranging from ultrasoft to rubber-like [6]. Additionally, the stiffness of PDMS can also be varied by temperature. When the temperature is reduced below the melting point of PDMS, $T_m \approx 230\,\mathrm{K}$, the polymer undergoes a phase transition into a semi-crystalline state and consequently becomes rigid [10–13]. The mechanical properties of elastomers (e.g. stiffness, elastic modulus) can be quantified by measuring the response of the elastomer to mechanical loading.

2.2.2 Mechanical Properties of Elastomers

Solids respond to small mechanical loading by elastic deformation, a reversible deformation. Solids returns to their original shape when the small mechanical load is removed. In contrast, fluids respond to even small mechanical loading by viscous deformation, a time-dependent irreversible deformation. Interestingly, elastomers are viscoelastic because they display both elastic and viscous responses to mechanical loading.

One of the main mechanical properties studied in this dissertation is a material's elastic modulus, which is of physiological relevance to biological systems [14,15]. The elastic modulus is an *intensive* property that depends only on the type of material and therefore is independent of geometry. The elastic modulus relates the applied stress $(\sigma)$, defined as the applied force per unit area to the resulting strain $(\gamma, \varepsilon)$, which is a normalized measure of the resulting deformation. Several different types of elastic moduli can be defined based on the type and direction of applied stress to the material [16]. In particular, cells on a substrate generate mechanical stresses that can be decomposed into two components, a component that acts parallel to the surface (shear), and a normal component that acts perpendicular to the surface (compression or tension) [17,18]. **Figure 2-2** shows two types of elastic moduli for a linear elastic material, the shear modulus $(G)$, and Young's modulus $(E)$, which are given by the following equations,

$$G = \frac{\sigma_{shear}}{\gamma} \tag{2-1}$$

$$E = \frac{\sigma_{uniaxial}}{\varepsilon} \tag{2-2}$$

where $\sigma_{shear}$ is the shear stress, $\gamma$ is the shear strain, $\sigma_{uniaxial}$ is the uniaxial stress, and $\varepsilon$ is the uniaxial strain.

It is important not to confuse elastic modulus (an *intensive* quantity) with stiffness (an *extensive* quantity). Stiffness is the measure of a material's ability to resist deformation in response to an applied force and it depends on the geometry of the material. A simple

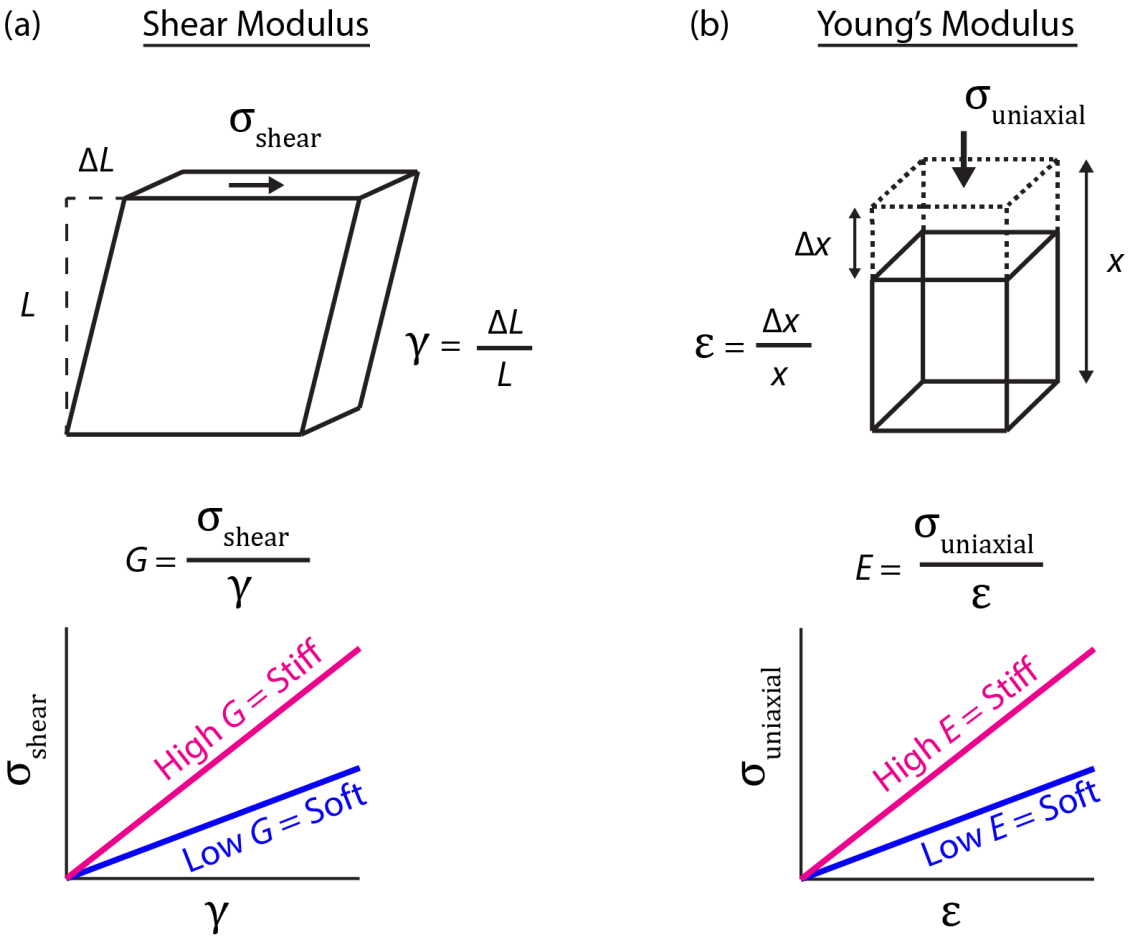


**Figure 2-2** Schematic of the deformation response of a linear elastic material to (a) shear stress ($\sigma_{shear}$) and (b) uniaxial stress ($\sigma_{uniaxial}$). $G$, $E$, $\gamma$, and $\varepsilon$ are the shear modulus, Young's modulus, shear strain and uniaxial strain, respectively.

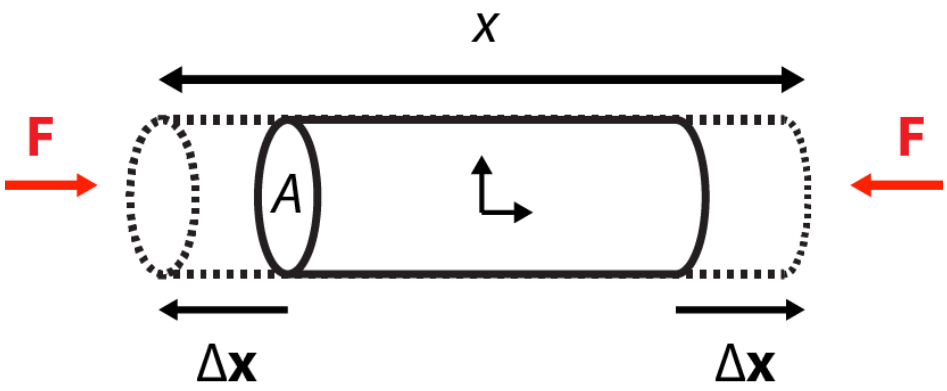


**Figure 2-3** Deformation of a linear elastic rod in response to an axial compression. **F** is the force, $x$ is the resting length of the rod, $\Delta\mathbf{x}$ is the deformation on each side, and $A$ is the cross-sectional area of the rod.

model of a linear elastic rod having length $x$ being compressed axially from both sides by force $F$, as shown in **Figure 2-3**, can be used to illustrate the difference between stiffness and Young's modulus. Under the assumptions that the applied uniaxial stress is uniform and the longitudinal strain is uniform through the cross-section ($A$) of the rod gives the relation between stiffness $k$ and Young's modulus $E$ as [16],

$$E = \frac{\sigma_{uniaxial}}{\varepsilon} = \frac{\left(\frac{k\Delta x}{A}\right)}{\left(\frac{2\Delta x}{x}\right)} = \frac{kx}{2A} \rightarrow k = \frac{2EA}{x} \qquad (2\text{-}3)$$

As can be seen from equation (2-3), the stiffness $k$ is proportional to the cross-sectional area of the rod, and inversely proportional to the length of the rod. Therefore, stiffness depends on the geometry of the material. The discussion so far has been limited to static mechanical loading; however dynamic mechanical loading can cause a time-dependent response in viscoelastic materials.

The viscous properties of a viscoelastic material can be measured by applying a dynamic stress and measuring the dynamic strain in the material. In the case of an

oscillatory shear stress applied in the linear viscoelastic regime, the strain response is described by the following equation,

$$\sigma_t = \gamma_0 (G' \sin(\omega t) + G'' \cos(\omega t)) \quad (2\text{-}3)$$

where $\sigma_t$ is the sinusoidal shear stress, $\gamma_0$ is the amplitude of the shear strain, $G'$ is the shear storage modulus, $G''$ is the shear loss modulus, $\omega$ is the angular frequency, and $t$ is the time [19].

### 2.3 Magnetic Materials and Magnetism

Based on the magnetic properties, all materials can be classified into five basic types: diamagnets, paramagnets, ferromagnets, antiferromagnets and ferrimagnets. Relevant to this dissertation are the first three types of materials, diamagnets, paramagnets, and ferromagnets, as illustrated in **Figure 2-4**. This section discusses the magnetic properties of diamagnets, paramagnets and ferromagnets with the focus on ferromagnets.

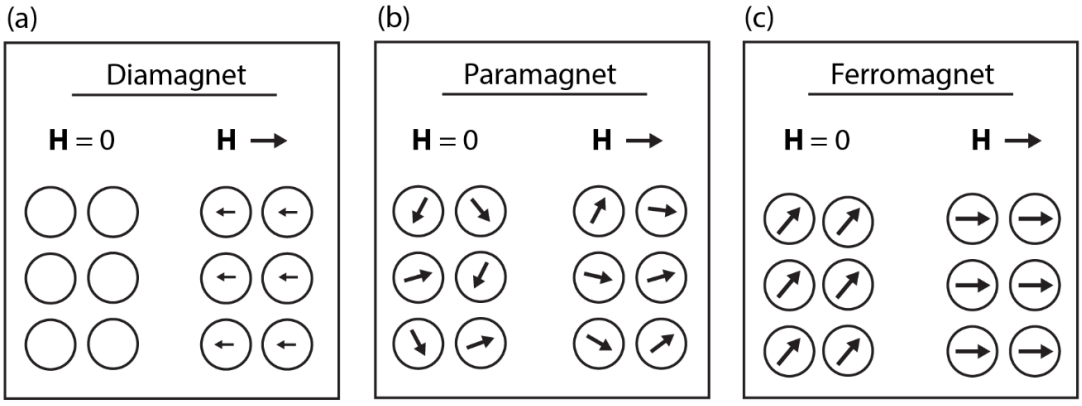


**Figure 2-4** Overview of (a) diamagnets, (b) paramagnets and (c) ferromagnets.

2.3.1 Diamagnets and Paramagnets

Diamagnets, also known as diamagnetic materials, are materials that can always be repelled by magnetic fields. As schematically shown in **Figure 2-4a**, diamagnets lack spontaneous atomic-scale magnetic moments in the absence of applied magnetic field. When an external magnetic field is applied, diamagnets will have small induced magnetic moments that oppose the applied magnetic field [20]. Such a response to applied magnetic field is called diamagnetism, which exists in all materials. Magnetic susceptibility $\chi$ is often defined as the ratio of the magnetization ($\mathbf{M} \equiv$ magnetic moment/volume) to the applied magnetic field, so $\mathbf{M} = \chi\mathbf{H}$. For diamagnets, $\chi < 0$ and in SI units is typically on the order of $|\chi| \approx 10^{-6}$ or less. Therefore, diamagnetism is very weak in comparison to other magnetisms and is only observable in diamagnets, where diamagnetism is the only contribution to the magnetism of the materials [21]. It is important to note that the magnetic susceptibility of diamagnets is independent of temperature because the induced moments are not affected by temperature. Common examples of diamagnets include water ($\chi = -9 \times 10^{-6}$) [22], Bismuth ($\chi = -1.6 \times 10^{-4}$) [23], and the vast majority of living cells ($\chi \approx -10^{-6}$) [24]. The diamagnetic behavior of living cells is utilized in chapter 6 to create heterogeneous distributions of cells for applications in tissue regeneration.

Similar to diamagnets, paramagnets have no macroscopic net magnetic moments so the magnetization ($\mathbf{M} \equiv$ magnetic moment/volume) in the absences of an applied magnetic field is zero. However, paramagnets consist of atomic-scale magnetic moments due to unpaired electrons. These magnetic moments do not magnetically interact, so they are randomly oriented (**Figure 2-4b**) due to thermal agitation in the absence of an applied

magnetic field. Application of an external magnetic field causes these atomic-scale magnetic moments to become more aligned along the field direction as they compete against the thermal energy [21]. In contrast to diamagnets, the magnetic susceptibility of paramagnets is $\chi > 0$ with a temperature dependent magnitude given by Curie's law, $\chi = C/T$, where C is a material-specific Curie constant [20]. At room temperature, paramagnets typically have a magnetic susceptibility on the order of $\chi \approx 10^{-3} - 10^{-5}$ in SI units [25]. One example of a paramagnet is the lanthanide ion gadolinium (III), which is commonly used in contrast agents for magnetic resonance imaging (MRI) [26]. The paramagnetic properties of gadolinium-based contrast agents are utilized in chapter 6 to enhance the magnetic properties of hydrogels.

### 2.3.2 Ferromagnets

Ferromagnets, like paramagnets, consist of atomic-scale magnetic moments due to unpaired electrons. However, ferromagnets exhibit spontaneous magnetization in the absence of an applied magnetic field due to the exchange interaction which favors parallel alignment between neighboring atomic-scale magnetic moments (**Figure 2-4c**). The ordering between neighboring atomic-scale magnetic moments is observed at temperatures below a critical temperature known as the Curie temperature $T_C$. At temperatures above $T_C$, thermal agitation becomes large enough that the spontaneous magnetization is observed to vanishes and the material becomes a paramagnet [21,27]. The internal magnetic configuration of a ferromagnet is determined by the minimization of the total magnetic energy, which arises from several different magnetic interactions.

2.3.3 Magnetic Interactions

The total magnetic energy associated with a common ferromagnet can be written as the sum of four terms,

$$U_{magnetic} = U_{exchange} + U_{dipolar} + U_{Zeeman} + U_{anisotropy} \quad (2\text{-}5)$$

where $U_{exchange}$ is the exchange interaction energy, $U_{dipolar}$ is the dipolar interaction energy, $U_{Zeeman}$ is the Zeeman energy, and $U_{anisotropy}$ is the energy related to the magnetic anisotropy.

The exchange interaction of a ferromagnet consisting of atoms $i$ and $j$ with magnetic spin $\mathbf{m_i}$ and $\mathbf{m_j}$, respectively, can be most commonly modeled by the Heisenberg exchange interaction, which is described by the equation,

$$U_{exchange} = -2\sum_{i>j} J_{ij}\,\mathbf{m_i}\cdot\mathbf{m_j} \quad (2\text{-}6)$$

where $J_{ij}$ is the exchange integral, which is related to the overlap of the charge distributions between the neighboring two atoms [20]. For ferromagnetic materials, the sign of the exchange integral $J_{ij}$ is mainly positive, which favors parallel alignment of adjacent spins [28].

In stark contrast to the short-range exchange interaction, the dipolar interaction is a long-range interaction that favors magnetic flux-closure. The dipolar interaction energy of a ferromagnet consisting of magnetic dipoles $\mathbf{m}_i$ and $\mathbf{m}_j$ is given by the equation,

$$U_{dipolar} = \sum_{i,j,i\neq j} \frac{\mu_0}{4\pi|\mathbf{r}|^3}\left[3(\mathbf{m}_i\cdot\hat{\mathbf{r}})(\mathbf{m}_j\cdot\hat{\mathbf{r}}) - \mathbf{m}_i\cdot\mathbf{m}_j\right] \quad (2\text{-}7)$$

where $\mu_0$ is the vacuum permeability and r is the distance between the two magnetic dipoles $\mathbf{m}_i$ and $\mathbf{m}_j$.

The Zeeman energy describes the potential energy of a magnetic dipole **m** in an external applied magnetic field **H** given by the equation,

$$U_{Zeeman} = -\mu_0 \mathbf{m} \cdot \mathbf{H} \tag{2-8}$$

The Zeeman energy favors alignment of the magnetic dipole in the direction of the applied magnetic field. Equation (2-8) can be extended to a magnetic material by integrating over the volume,

$$U_{Zeeman} = -\mu_0 \int_V \mathbf{M} \cdot \mathbf{H}\, dV \tag{2-9}$$

Magnetic anisotropy determines the favored (easy) direction of magnetization in a ferromagnetic material. One of the main sources for magnetic anisotropy is the magnetocrystalline anisotropy, which is a dependence of the magnetic energy on the orientation of the magnetization relative to the crystalline axes. The magnetocrystalline anisotropy stems from the spin-orbit interactions of the electrons in a crystalline solid, where the orbital moment of the electrons is strongly coupled with the crystal electric field [21].

The equilibrium magnetization configuration of a ferromagnet is determined by the minimization of equation (2-5). One example is the formation of magnetic domains in ferromagnets. Magnetic domains are regions within which the direction of magnetization is uniform. Neighboring domains in a macroscopic ferromagnet are separated by domain walls where the magnetization rotates gradually over a finite distance of about 10-100 nm [21]. From an energy perspective, magnetic domains result from the competition between minimizing the exchange interaction energy, which favors parallel alignment of neighboring atomic magnetic moments within the domains, and the long range magnetic

dipolar interaction, which favors flux-closure for multiple domains. The magnetic configuration of a ferromagnet can be changed by varying an applied magnetic field.

2.3.4 Magnetic Hysteresis Loops

A hallmark of ferromagnets is that they exhibit a history dependence, or hysteresis, in their magnetization as shown in **Figure 2-5a.** Saturation occurs at the saturating field $H_s$ where the magnetization is all aligned with applied magnetic field direction reaching a maximum value of $M_s$. The magnetization decreases as the applied magnetic field decreases down from $+H_s$. When the applied magnetic field is removed (i.e. $H = 0$) the ferromagnet retains a remanent magnetization $M_r$, or simply remanence, due to

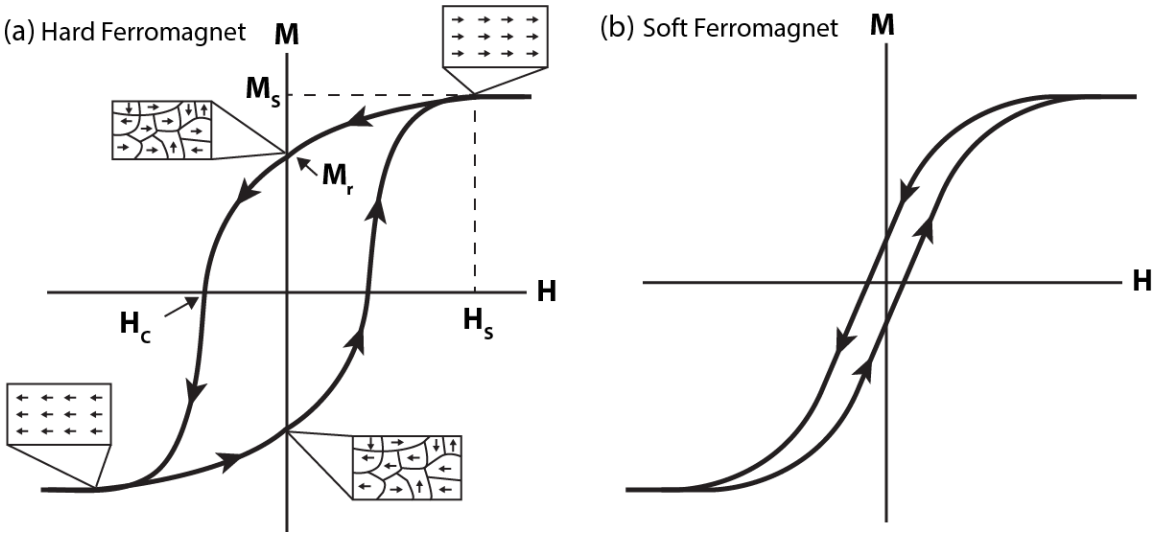


**Figure 2-5** Major magnetic hysteresis loops of ferromagnets. (a) Magnetic hysteresis loop for a typical hard ferromagnet with cartoon drawings depicting the internal magnetization direction of the domains at various points along the major hysteresis loop. $M_s$, $H_s$, $M_r$, and $H_c$ are the saturation magnetization, saturating field, remanent magnetization, and coercive field, respectively. (b) Magnetic hysteresis loop of a typical soft ferromagnet.

spontaneous magnetization. The field in the opposite direction of $H_s$ required to reduce the magnetization to zero is called the coercive field $H_c$. Decreasing the magnetic field further down to $-H_s$ results in saturation in the opposite direction. Increasing the magnetic field back up to $+H_s$ creates a complete cycle (i.e. $+H_s \rightarrow -H_s \rightarrow +H_s$) and such a closed M-H loop is called a major magnetic hysteresis loop. A minor hysteresis loop is a closed M-H loop cycled between $+H_{max}$ and $-H_{max}$, where $H_{max} < H_s$. Hysteresis loops contain a wealth of information about the magnetic properties of a ferromagnetic material. As an example, the area enclosed by a hysteresis loop can be used to determine the energy loss per cycle in magnetizing the ferromagnetic material [21].

Ferromagnets can be classified as magnetically hard or magnetically soft based on their coercivity. Hard ferromagnets have a large coercivity and exhibit a wide hysteresis loop shape (**Figure 2-5a**). In contrast, soft ferromagnets have a small coercivity and exhibit a narrow or overlapping hysteresis loop (**Figure 2-5b**). Ferromagnetic particles with cubic crystalline structure, such as iron, typically exhibit soft magnetic behavior [29].

### 2.4 Magnetic Properties of Iron Microparticles

Carbonyl iron powder (CIP, BASF™), consisting of high purity spherical iron particles with a mean diameter of $\approx 3$ μm, is widely used in MRE synthesis. These magnetically soft iron microparticles have attractive magnetic properties like high saturation magnetization, low coercivity, low remanent magnetization, high Curie temperature, and commercial availability. Magnetic hysteresis loops of these multi-domain iron particles highlight their near-zero remanence and small coercivity (**Figure 2-6**), which limit their agglomeration during MRE synthesis and provide reversible characteristics to

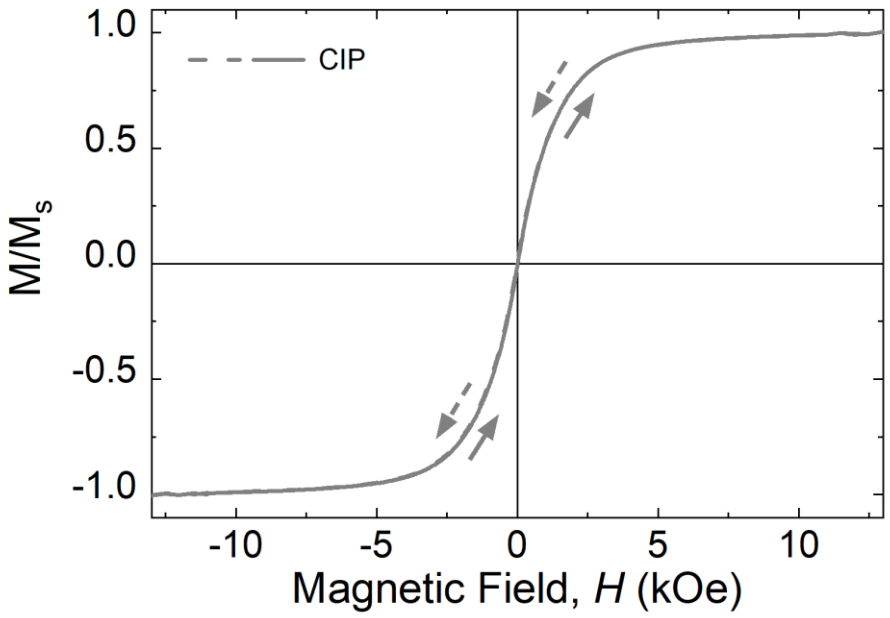


**Figure 2-6** Major magnetic hysteresis of carbonyl iron powder (BASF™) showing near-zero remanence, and small coercivity.

the MREs. The minimal area enclosed by the hysteresis loop indicates that the hysteresis losses in iron microparticles are small.

### 2.4.1 Micromagnetic Configuration of a Magnetic Particle

The complex magnetization reversal within an individual magnetic particle is not captured in magnetic hysteresis loops, which measure the net magnetic response from an ensemble of particles. However, it can be investigated using micromagnetic simulations. Due to the micron size of the iron particles, GPU-accelerated micromagnetic simulators, such as mumax$^3$ [30], are favored as they offer speeds up to 100 times that of CPU-based micromagnetic simulators (e.g. Object Oriented MicroMagnetic Framework). Mumax$^3$ simulations minimize the total magnetic energy given by equation (2-5) to determine the equilibrium magnetic configuration. Micromagnetic simulations in collaboration with

Tong Dang revealed complicated magnetic configurations within the particle during magnetization reversal. As an example, the formation of a vortex state in the plane perpendicular to the applied magnetic field direction was observed (**Figure 2-7**). Vortex states have also been observed experimentally in iron microparticles using electron beam holography [31]. Despite the complicated magnetic configuration, the iron particle's simulated hysteresis loop (**Figure 2-8a**) shows a linear response of the particle's magnetization to the applied magnetic field below magnetic saturation, similar to what was

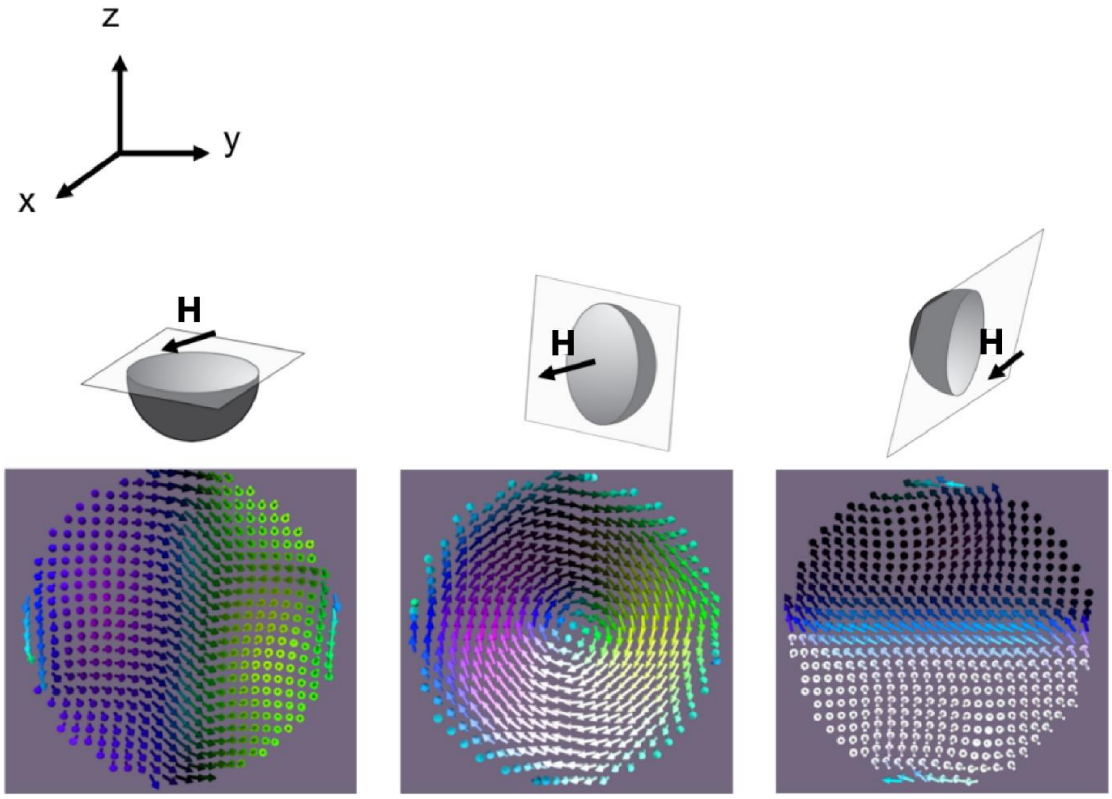


**Figure 2-7** Internal magnetic configuration on the xy, yz, and xz planes, respectively, of a 3μm iron particle subjected to $\mu_0 \mathbf{H} = 0.15$ T $\hat{\mathbf{x}}$. A magnetic vortex state forms on the plane normal to the applied magnetic field direction. Courtesy of Tong Dang.

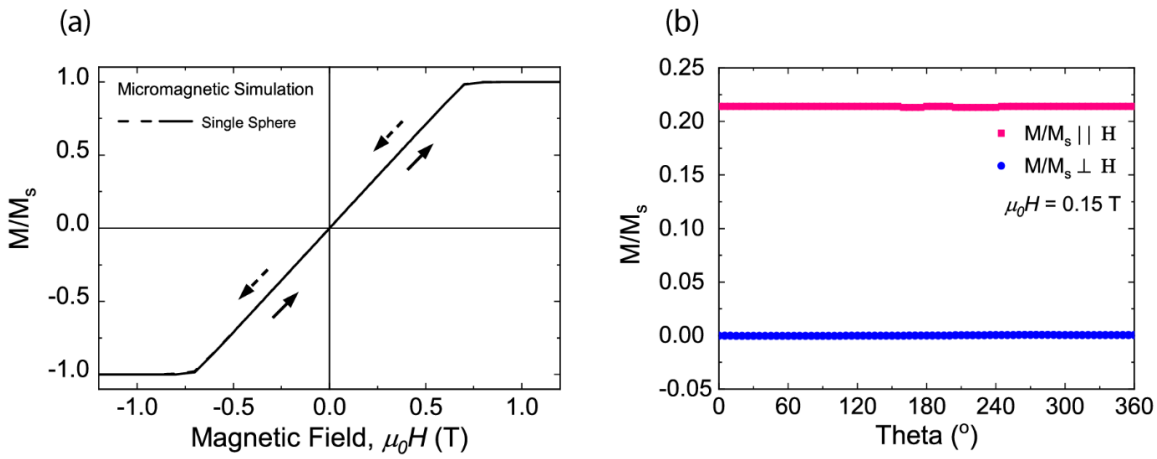


**Figure 2-8** Net magnetization along the applied magnetic field direction of a 3 μm diameter iron particle calculated from micromagnetic simulations. (a) Magnetic hysteresis loop showing increasing (solid) and decreasing (dashed) branches of the reduced magnetization. (b) Components of the magnetization parallel (square, magenta) and perpendicular (circle, blue) to the applied magnetic field $\mu_0\mathbf{H} = 0.15\ \mathrm{T}\,\hat{\mathbf{x}}$ as a function of the angle theta between the applied magnetic field and the positive x axis. Courtesy of Tong Dang.

observed experimentally (**Figure 2-6**). More importantly, as the filed direction is changed while the field magnitude is kept, these complex magnetization states at intermediate magnetic fields are found to rotate collectively with the magnetic field, evidenced by the constant $M/M_s$ at various field angles in **Figure 2-8b**. This collective rotation of magnetic configuration of a micron-sized iron particle indicates that the individual iron particles can be approximated as isotropic magnetic dipoles.

### 2.4.2 Force Between Two Magnetic Dipoles

The ability to model the iron particles as magnetic dipoles greatly simplifies various calculations, such as the magnetic force between two iron particles. The magnetic force between two dipoles is related to the dipolar energy by taking the negative gradient, $\mathbf{F} = -\boldsymbol{\nabla} U_{dipolar}$. As an example, the magnitude of the attractive force between two-point

magnetic dipoles each having magnetic moment $m$ oriented along the line that connects them, $S$, is given by the equation,

$$|F| = \left| -\frac{\partial}{\partial S}\left[\frac{\mu_0}{4\pi S^3}(3m^2 - m^2)\right]\right| = \frac{3\mu_0 m^2}{2\pi S^4} \quad (2\text{-}10)$$

In contrasts, if the magnetic dipoles are oriented perpendicular to $S$, the force becomes repulsive and is its magnitude is given by the equation,

$$|F| = \frac{3\mu_0 m^2}{4\pi S^4} \quad (2\text{-}11)$$

## 2.5 Modeling the Magneto-mechanical Coupling in MREs

Magneto-mechanical coupling in MREs leads to interesting magnetic and mechanical properties. The total energy associated with an MRE includes the magnetic energy of the particles as well as the mechanical energy from the polymer matrix and in general can be written as,

$$U_{Total} = U_{magnetic} + U_{mechanical} \quad (2\text{-}12)$$

where $U_{magnetic}$ generally include the exchange interaction, magnetic dipolar interaction, magnetic anisotropy and Zeeman energy. As indicated by the micromagnetic simulations in section 2.4.1, iron particles can be modeled as isotropic magnetic dipoles thus simplifying $U_{magnetic}$.

### 2.5.1 Two-dipole Model

A simple model for capturing the magneto-mechanical coupling in MREs is a two-dipole model (**Figure 2-9**) having magnetic dipoles $\mathbf{m_1}$ and $\mathbf{m_2}$ separated by a distance **S** connected by a Hookean spring having equilibrium length $S_o$. The total energy of this

system when a magnetic field is applied along the direction of the spring that connects the two dipoles is given by the equation,

$$U_{Total} = \frac{\mu_0}{4\pi|\mathbf{S}|^3}(3m^2 - m^2) - \frac{1}{2}k(S - S_o)^2 + \frac{\mu_0 m^2}{\chi V} \tag{2-13}$$

where the first term is the magnetic dipolar interaction energy, the second term is the elastic restoring force and the third term is the self-energy of the two dipoles. As mentioned in section 2.4.2, the force can be derived by taking the negative gradient of the potential energy. The net force experienced by either magnetic dipole is,

$$F = -k(S - S_o) - \frac{3\mu_0 m^2}{2\pi S^4} \tag{2-14}$$

where a negative (positive) $F$ represents an attractive (repulsive) net force. One of the limitations of this model is that it only captures translational motion for two specific cases, when the magnetic field is applied along the spring that connects the dipoles (attractive),

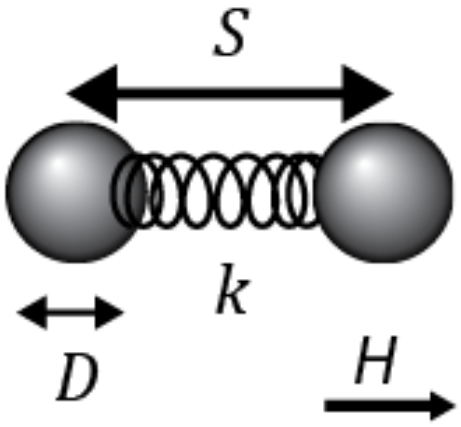


**Figure 2-9** Cartoon schematic of a simple two-dipole model that incorporates the magneto-mechanical coupling in MREs. The spheres shown represent the iron particles having diameter $D$, which are modeled as point magnetic dipoles located at the center of each sphere which are connected by a Hookean spring with stiffness $k$ and separated by distance $S$.

or perpendicular to the spring (repulsive). This two-dipole model is used in chapter 4 to investigate the effect of polymer stiffness on the magnetization reversal of MREs.

### 2.5.2 Mechanical Property Model

The magnetic field-dependent increase in shear modulus of MREs can be modeled by approximating the MRE as a homogenous material [32] with magnetic permeability $\mu$. Upon mechanical deformation, the magnetic permeability becomes a function of the deformation tensor [33] $u_{ik}$ and can be written in CGS units using Einstein summation notation as,

$$\mu_{ik} = \mu^0 \delta_{ik} + a_1 u_{ik} + a_2 u_{ll} \delta_{ik} \tag{2-15}$$

where $\mu^0$ is the relative permeability of the undeformed MRE, $\delta_{ik}$ is the Kronecker delta, and $a_1$ and $a_2$ are constants. Since PDMS is incompressible [34], $u_{ll} = 0$, the last term vanishes. Using magnetic liquids as a guide, the magnetic antisymmetric stress can be written as,

$$\sigma_{ik} = \frac{1}{2} \epsilon_{ikl} [\mathbf{M} \times \mathbf{H_0}]_l \tag{2-16}$$

where $\epsilon_{ikl}$ is the Levi-Civita symbol, $\mathbf{M}$ is the magnetization and $\mathbf{H_0}$ is the externally applied magnetic field. If the z-direction is taken to be the axial direction of the rheometer plate, the shear stress can then be written as,

$$\sigma_{ik} = \frac{1}{2} M_x H_z \tag{2-17}$$

The deformation tensor for oscillatory rheometry can be modeled by assuming a linear shear resulting in,

$$u_{xz} = \frac{1}{2} \frac{\partial u_x}{\partial z} \tag{2-18}$$

The component of the magnetization along the x direction can then be written as,

$$M_x = \frac{\mu_{xz}}{4\pi} H_z \tag{2-19}$$

where $\mu_{xz}$ is the xz component of the magnetic permeability of the MRE and $H_z$ is the z component of the internal magnetic field within the MRE, which includes the demagnetization. Writing $\mu_{xz}$ in terms of equation (2-15) and accounting for linear strain in equation (2-18) results in,

$$\mu_{xz} = a_{1u_{xz}} = a_1 \left( \frac{1}{2} \frac{\partial u_x}{\partial z} \right) \tag{2-20}$$

Since PDMS is incompressible, $H_z = \frac{H_0}{\mu^0}$, the shear stress can be written as,

$$\sigma_{xz} = \frac{1}{16\pi} a_1 \left( \frac{H_0}{\mu^0} \right)^2 \frac{\partial u_x}{\partial z} \tag{2-21}$$

Using the value of constant $a_1$ from a previous work [35], and noting that $\sigma_{xz} = G' \frac{\partial u_x}{\partial z}$, where $G'$ is the shear storage modulus, results in

$$G' = \frac{1}{40\pi} \frac{(\mu^0 - 1)^2}{\mu^0} H_0^2 \tag{2-22}$$

indicating a quadratic dependence on the applied magnetic field, which is similar to other models that consider individual iron particles [36,37]. The quadratic dependence of the applied magnetic field on the shear storage modulus provides a foundation for fitting the field-dependent mechanical properties of ultrasoft MREs in chapter 5.

**References for Chapter 2**

[1] R. J. Young and P. A. Lovell, *Introduction to Polymers: Third Edition*, 3rd ed. (CRC Press, United States, 2011).

[2] V. Drebezghova, H. Gojzewski, A. Allal, M. A. Hempenius, C. Nardin, and G. J. Vancso, *Network Mesh Nanostructures in Cross-Linked Poly(Dimethylsiloxane) Visualized by AFM*, Macromol. Chem. Phys. 2000170 (2020).
[3] B. ter Horst, N. S. Moiemen, and L. M. Grover, *Natural Polymers*, in *Biomaterials for Skin Repair and Regeneration* (Elsevier, 2019), pp. 151–192.
[4] D. A. McQuarrie, *General Chemistry*, 4th ed. / Ethan B. Gallogly; illustrations by George Kelvin and Laurel Muller. (University Science Books, Mill Valley, CA, 2011).
[5] A. K. Bastola and M. Hossain, *A Review on Magneto-Mechanical Characterizations of Magnetorheological Elastomers*, Compos. Part B Eng. **200**, 108348 (2020).
[6] R. N. Palchesko, L. Zhang, Y. Sun, and A. W. Feinberg, *Development of Polydimethylsiloxane Substrates with Tunable Elastic Modulus to Study Cell Mechanobiology in Muscle and Nerve*, PloS One **7**, e51499 (2012).
[7] I. Miranda, A. Souza, P. Sousa, J. Ribeiro, E. M. S. Castanheira, R. Lima, and G. Minas, *Properties and Applications of PDMS for Biomedical Engineering: A Review*, J. Funct. Biomater. **13**, 2 (2021).
[8] Y. Cheng, N. Shimizu, and T. Kimura, *The Viscoelastic Properties of Soybean Curd (Tofu) as Affected by Soymilk Concentration and Type of Coagulant*, Int. J. Food Sci. Technol. **40**, 385 (2005).
[9] A. Oláh, H. Hillborg, and G. J. Vancso, *Hydrophobic Recovery of UV/Ozone Treated Poly(Dimethylsiloxane): Adhesion Studies by Contact Mechanics and Mechanism of Surface Modification*, Appl. Surf. Sci. **239**, 410 (2005).
[10] A. V. Bodnaruk, A. Brunhuber, V. M. Kalita, M. M. Kulyk, A. A. Snarskii, A. F. Lozenko, S. M. Ryabchenko, and M. Shamonin, *Temperature-Dependent Magnetic Properties of a Magnetoactive Elastomer: Immobilization of the Soft-Magnetic Filler*, J. Appl. Phys. **123**, 115118 (2018).
[11] A. V. Bodnaruk, A. Brunhuber, V. M. Kalita, M. M. Kulyk, P. Kurzweil, A. A. Snarskii, A. F. Lozenko, S. M. Ryabchenko, and M. Shamonin, *Magnetic Anisotropy in Magnetoactive Elastomers, Enabled by Matrix Elasticity*, Polymer **162**, 63 (2019).
[12] A. V. Bodnaruk, V. M. Kalita, M. M. Kulyk, A. F. Lozenko, S. M. Ryabchenko, A. A. Snarskii, A. Brunhuber, and M. Shamonin, *Temperature Blocking and Magnetization of Magnetoactive Elastomers*, J. Magn. Magn. Mater. **471**, 464 (2019).
[13] J. Osicka, M. Mrlik, M. Ilcikova, B. Hanulikova, P. Urbanek, M. Sedlacik, and J. Mosnacek, *Reversible Actuation Ability upon Light Stimulation of the Smart Systems with Controllably Grafted Graphene Oxide with Poly (Glycidyl Methacrylate) and PDMS Elastomer: Effect of Compatibility and Graphene Oxide Reduction on the Photo-Actuation Performance*, Polymers **10**, 832 (2018).
[14] D. E. Discher, P. Janmey, and Y. Wang, *Tissue Cells Feel and Respond to the Stiffness of Their Substrate*, Science **310**, 1139 (2005).
[15] R. G. Wells, *The Role of Matrix Stiffness in Regulating Cell Behavior*, Hepatology **47**, 1394 (2008).
[16] J. Lubliner and P. Papadopoulos, *Elasticity*, in *Introduction to Solid Mechanics: An Integrated Approach*, edited by J. Lubliner and P. Papadopoulos (Springer International Publishing, Cham, 2017), pp. 247–321.

[17] W. R. Legant, C. K. Choi, J. S. Miller, L. Shao, L. Gao, E. Betzig, and C. S. Chen, *Multidimensional Traction Force Microscopy Reveals Out-of-Plane Rotational Moments about Focal Adhesions*, Proc. Natl. Acad. Sci. **110**, 881 (2013).
[18] W. J. Polacheck and C. S. Chen, *Measuring Cell-Generated Forces: A Guide to the Available Tools*, Nat. Methods **13**, 415 (2016).
[19] J. J. Aklonis and W. J. MacKnight, *Introduction to Polymer Viscoelasticity*, 3rd ed (Wiley-Interscience, Hoboken, N.J, 2005).
[20] C. Kittel, *Introduction to Solid State Physics*, 8th ed. (John Wiley & Sons, New York, NY, 2004).
[21] R. O'Handley, *Modern Magnetic Materials: Principles and Applications* (John Wiley & Sons, New York, NY, 2000).
[22] G. P. Arrighini, M. Maestro, and R. Moccia, *Magnetic Properties of Polyatomic Molecules. I. Magnetic Susceptibility of $H_2O$, $NH_3$, $CH_4$, $H_2O_2$*, J. Chem. Phys. **49**, 882 (1968).
[23] S. Otake, M. Momiuchi, and N. Matsuno, *Temperature Dependence of the Magnetic Susceptibility of Bismuth*, J. Phys. Soc. Jpn. **49**, 1824 (1980).
[24] V. Zablotskii, T. Polyakova, O. Lunov, and A. Dejneka, *How a High-Gradient Magnetic Field Could Affect Cell Life*, Sci. Rep. **6**, 37407 (2016).
[25] D. R. Lide, *CRC Handbook of Chemistry and Physics*, Handb. Chem. Phys. Online (2001).
[26] Y.-D. Xiao, R. Paudel, J. Liu, C. Ma, Z.-S. Zhang, and S.-K. Zhou, *MRI Contrast Agents: Classification and Application (Review)*, Int. J. Mol. Med. **38**, 1319 (2016).
[27] X. Cheng, Magnetization Reversal and Magnetotransport Properties of Cobalt/Platinum Multilayers with Perpendicular Magnetic Anisotropy, Ph.D. Thesis, Johns Hopkins University, 2006.
[28] J. Stohr and H. Siegmann, *Magnetism : From Fundamentals to Nanoscale Dynamics*, Vol. 152 (Springer, Berlin, 2007).
[29] Q. Lu, K. Choi, J.-D. Nam, and H. J. Choi, *Magnetic Polymer Composite Particles: Design and Magnetorheology*, Polymers **13**, 512 (2021).
[30] A. Vansteenkiste, J. Leliaert, M. Dvornik, M. Helsen, F. Garcia-Sanchez, and B. Van Waeyenberge, *The Design and Verification of MuMax3*, AIP Adv. **4**, 107133 (2014).
[31] K. Sugimura, Y. Miyajima, M. Sonehara, T. Sato, F. Hayashi, N. Zettsu, K. Teshima, and H. Mizusaki, *Formation of High Electrical-Resistivity Thin Surface Layer on Carbonyl-Iron Powder (CIP) and Thermal Stability of Nanocrystalline Structure and Vortex Magnetic Structure of CIP*, AIP Adv. **6**, 055932 (2016).
[32] K. A. Tran, E. Kraus, A. T. Clark, A. Bennett, K. Pogoda, X. Cheng, A. Cēbers, P. A. Janmey, and P. A. Galie, *Dynamic Tuning of Viscoelastic Hydrogels with Carbonyl Iron Microparticles Reveals the Rapid Response of Cells to Three-Dimensional Substrate Mechanics*, ACS Appl. Mater. Interfaces **13**, 20947 (2021).
[33] L. D. Landau, E. M. Lifshitz, and A. L. King, *Electrodynamics of Continuous Media*, 3 (2014).
[34] A. Müller, M. C. Wapler, and U. Wallrabe, *A Quick and Accurate Method to Determine the Poisson's Ratio and the Coefficient of Thermal Expansion of PDMS*, Soft Matter **15**, 779 (2019).
[35] Y. M. Shkel and D. J. Klingenberg, *Electrostriction of Polarizable Materials: Comparison of Models with Experimental Data*, J Appl Phys **83**, 11 (2014).

[36] M. R. Jolly, J. D. Carlson, and B. C. Muñoz, *A Model of the Behaviour of Magnetorheological Materials*, Smart Mater. Struct. **5**, 607 (1996).
[37] L. Chen and S. Jerrams, *A Rheological Model of the Dynamic Behavior of Magnetorheological Elastomers*, J. Appl. Phys. **110**, 013513 (2011).

# Chapter 3: Synthesis and Characterization of MREs

## 3.1 Introduction

This chapter describes the synthesis and characterization methods used to investigate the magnetic and mechanical properties of MREs. First, section 3.2 presents the method for synthesizing magnetorheological elastomers. Then, the methods used to characterize the structural, magnetic, and mechanical properties are described in sections 3.3, 3.4 and 3.5, respectively.

## 3.2 Synthesis of MREs

**Figure 3-1** shows an overview of the MRE synthesis process. Ultrasoft ($E\sim$ kPa) PDMS-based MREs were synthesized using Sylgard™ 527 (Dow Corning™), prepared by mixing equal parts by weight of monomer and crosslinker and then mixing in magnetically soft carbonyl iron powder (CIP, BASF™) at volume fractions of $\Phi = 0, 3, 9, 17, 23, 30, \text{and } 40\%$. The volume fraction $\Phi$ was estimated using,

$$\Phi = \frac{V_{CIP}}{V_{Total}} = \frac{\frac{M_{CIP}}{\rho_{CIP}}}{\frac{M_{CIP}}{\rho_{CIP}} + \frac{M_{PDMS}}{\rho_{PDMS}}} \tag{3-1}$$

where $V_{CIP}$ and $V_{Total}$ are the volume of the CIP and total volume of the MRE, respectively, $m_{CIP}$ and $m_{PDMS}$ are the masses of the CIP and PDMS, respectively, and $\rho_{CIP} = 7.874$ kg/L and $\rho_{PDMS} = 0.95$ kg/L are the densities of CIP and PDMS, respectively.

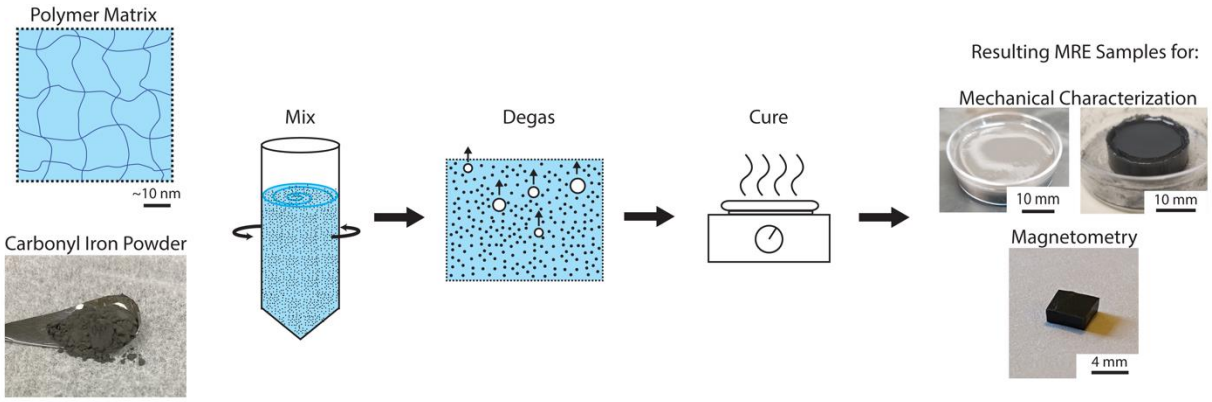


**Figure 3-1** Synthesis process of MREs

| $\Phi(\%)$ | Polymer Composition: Sylgard™ 527:Sylgard™ 184 (by weight) | $E$ (kPa) at $H = 0$ |
|---|---|---|
| 0 | 1:0 | $9.2 \pm 0.1$ |
| 3 | 1:0 | $8.7 \pm 0.6$ |
| 3 | 10:1 | $50 \pm 2$ |
| 3 | 5:1 | $106 \pm 1$ |
| 3 | 0:1 | $2{,}400 \pm 400$ |
| 9 | 1:0 | $15.8 \pm 0.1$ |
| 17 | 1:0 | $24.2 \pm 0.3$ |
| 23 | 1:0 | $27.5 \pm 1$ |
| 30 | 1:0 | Not Measured |
| 40 | 1:0 | Not Measured |

**Table 3-1** List of MRE samples synthesized and their respective volume fraction of iron particles and Young's moduli measured by compressive indentation for this thesis project.

Stiffer MREs with $E$ that range over two orders of magnitude [1] were synthesized by adding different amounts of a stiffer rubber-like ($E \sim$ MPa) PDMS Sylgard™ 184 (Dow Corning™). Prior to adding, Sylgard™ 184 was prepared by mixing ten parts monomer to one-part crosslinker. The mixtures were poured into 35 mm diameter culture dishes to a thickness of $\approx$ 5 mm and placed on a hotplate at 60°C for four hours and then left overnight at room temperature to ensure full crosslinking of the polymers. MRE samples used for rheology were poured into a 20 mm diameter Teflon™ mold to a thickness of $\approx$ 5 mm to match the rheometer plate. A list of MREs synthesized is displayed in **Table 3-1**.

## 3.3 Structure Characterization Methods

### 3.3.1 Surface Interferometry

Surface interferometry is a non-contact, non-destructive technique for measuring the topography and surface roughness of a material by using the interference of coherent light [2]. In particular, modern scanning white light interferometers (SWLI) are widely used for surface metrology due to their ability to image a millimeter wide area with nanometer resolution and larger dynamic range compared to traditional monochromatic interferometers [3,4]. SWLI consists of three main components, a broadband "white" light source, interferometric objectives, and a charge-coupled device (CCD) camera. A simplified schematic of a SWLI is shown in **Figure 3-2a**. Collimated white light is sent through a beam splitter resulting in an object beam, which reflects off the sample surface, and a reference beam that reflects off a reference mirror. The object and reference beams are then superimposed and focused onto the CCD camera for imaging. Surface topography of the sample creates changes in the path length difference between the object beam and

reference beam creating an interference pattern known as an interferogram. An interferogram is generated for each pixel on the CCD camera. The sample is then scanned through focus changing the irradiance of the interferogram as a function of optical path length difference as shown in **Figure 3-2b** for a monochromatic light source. The usage of white light as the illumination source creates a condition where there is only one maxima in the irradiance of each interferogram imaged (**Figure 3-2c**) and the corresponding height associated with the maxima is determined by tracking the sample motion during the scan [2,5].

SWLI was used to characterize the magnetic-field dependent surface topography and roughness of ultrasoft MREs studied in this dissertation. A Zygo NW 6100 SWLI

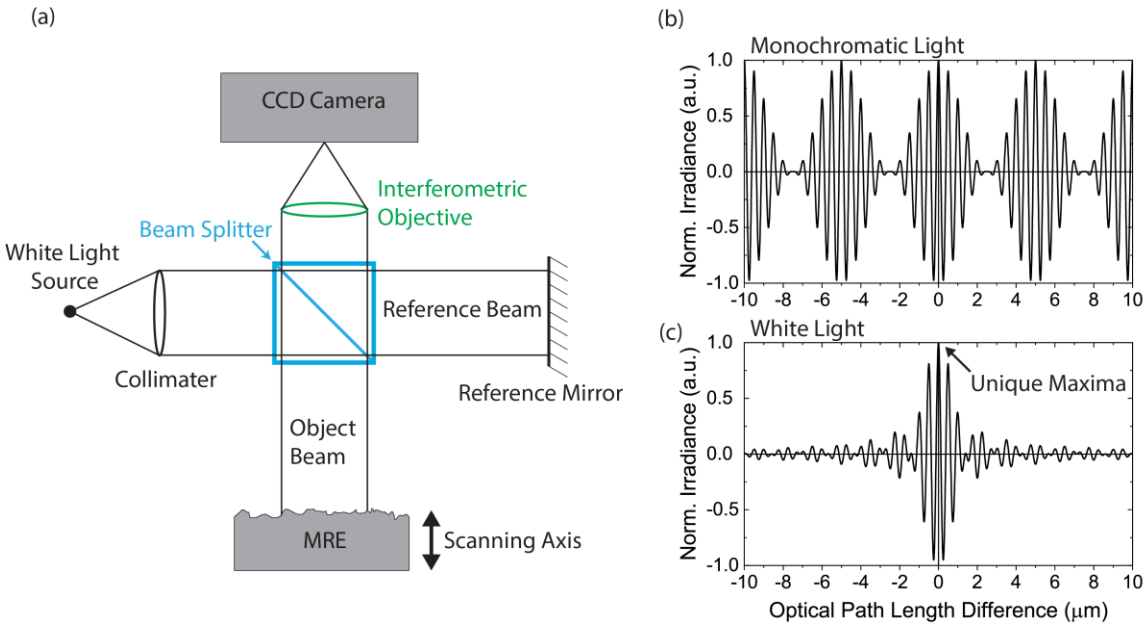


**Figure 3-2** Scanning white light interferometry. (a) Simplified schematic layout of a scanning white light interferometer. Normalized irradiance of an interferogram measured by a pixel on the CCD camera when (b) monochromatic and (c) white light is used.

equipped with a 20x objective set at 0.5x optical zoom (10x magnification) was used to image a $\approx 500 \times 700$ μm rectangular region of the MRE surface located at the center of the culture dish. The average surface roughness ($R_a$) and root-mean-squared surface roughness ($R_q$) of MREs were recorded at each magnetic field strength. SWLI was performed in collaboration with Dr. Alexander Bennett at the University of Pennsylvania.

### 3.3.2 Confocal Fluorescence Microscopy

Confocal fluorescence microscopy is a powerful and widely used technique for 3-dimensional imaging. In contrast to wide field fluorescence microscopy which excites the fluorophores in the entire sample during imaging, a confocal fluorescence microscope operates by point excitation and uses a pinhole to reject out-of-focus light (**Figure 3-3a)**.

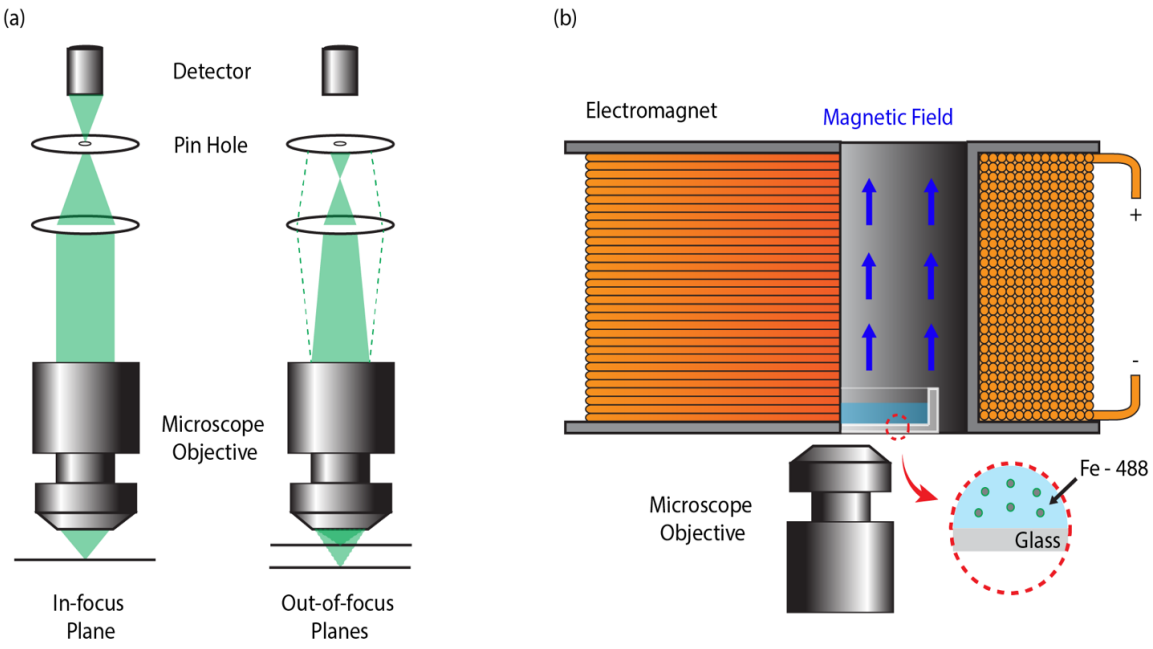


**Figure 3-3** Principal of confocal fluorescence microscopy. (a) A pin hole placed in front of the detector is used to reject light from out-of-focus planes. (b) Schematic of experimental setup for magnetic field-dependent confocal fluorescence microscopy.

The laser, used as the excitation source, is scanned over the specimen point by point to build the complete image on the camera [6,7]. The improved contrast of confocal fluorescence microscopy provides a slight gain in resolution, but it is still diffraction limited in all three dimensions.

Confocal microscopy imaging for this dissertation was performed at the Bio Imaging Center at the University of Delaware in collaboration with Dr. Sylvain Le Marchand, graduate student Zheng Cao, and Professor Elise Corbin. A Zeiss LSM880 confocal microscope equipped with a 20x/1.0 water immersion objective lens was used to image the magnetic field-dependent trajectory of fluorescently labeled CIP in ultrasoft MREs. **Figure 3-3b** displays a schematic of the experimental setup including the electromagnet used to apply the magnetic field to the ultrasoft MRE. The resolution of each stack of images, called a z-stack (**Figure 3-4a**), was $1772 \times 1772 \times 28$ pixels$^3$ with a voxel size of $120 \times 120 \times 410$ nm$^3$.

Image analysis was performed in MATLAB™ to quantitatively measure the trajectory of six iron particles (**Figure 3-4b**) as the applied magnetic field was increased from 0 to 500 Oe and back to 0 Oe in steps of 250 Oe. Prior to any applied magnetic field, an in-focus cropped image around each particle was selected. The initial in-focus images of each particle were then used as input for a 2D cross correlation to quantitatively determine the in-focus images for each particle at every magnetic field increment. **Figure 3-5** shows the magnetic field-dependent trajectory of one of the particles. The magnetic particle moves primarily along the magnetic field direction and the magnitude of the particle motion is larger when the magnetic field is increased from 250 to 500 Oe that it is for the 0 to 250 Oe field step. The observed motion is several microns in magnitude.

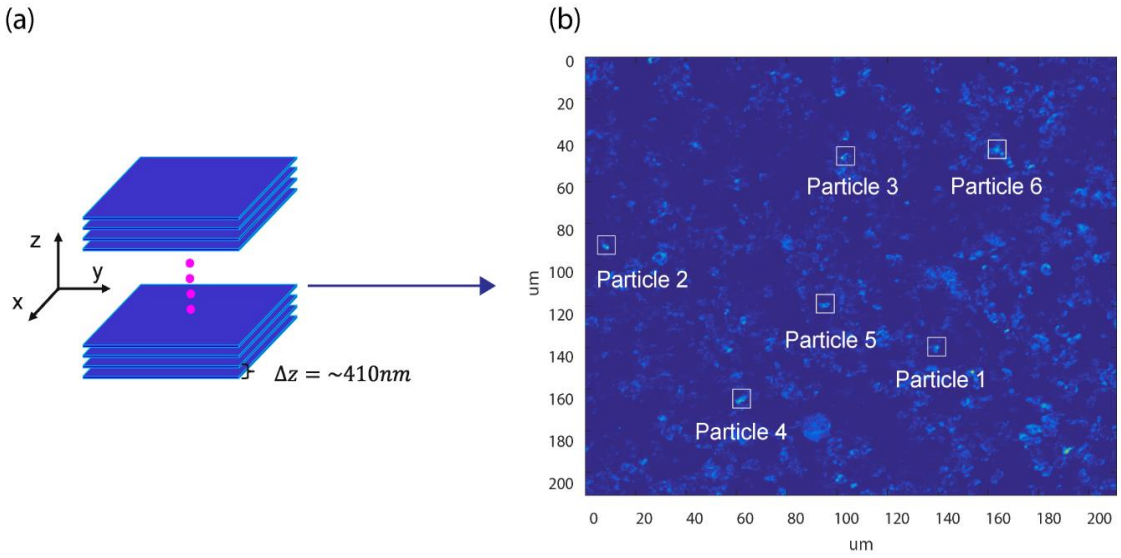


**Figure 3-4** Confocal microscopy image of image of an MRE. (a) Schematic of a z-stack. (b) A single image at $z = 5.3$ μm showing the six fluorescently labeled iron particles whose trajectories were tracked during application of a magnetic field.

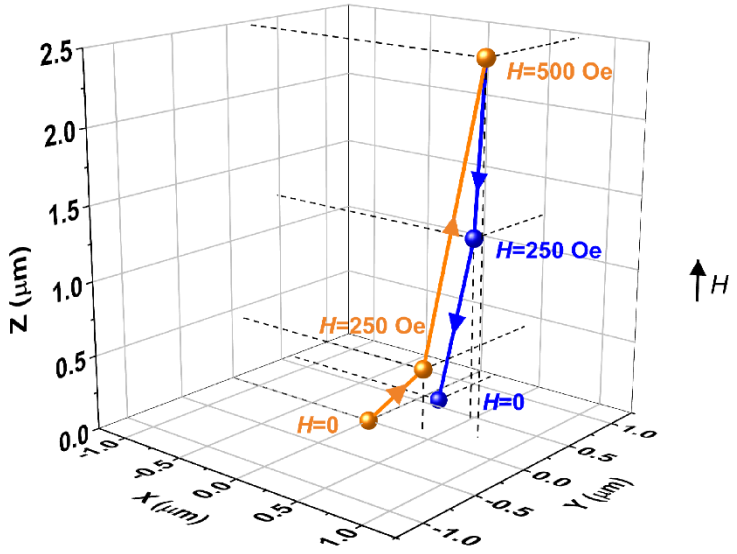


**Figure 3-5** Magnetic field-dependent trajectory of an iron particle within an ultrasoft MRE by confocal microscopy. Measurements were performed on an MRE having a volume fraction $\Phi = 3\%$ of iron particles that were fluorescently labeled with $H$ applied along the z direction. The uncertainty in the z-position is $\pm$ 400 nm and that for the x- and y- position is $\pm 1$ μm. Reproduced from [15], with the permission of AIP Publishing.

Additionally, **Figure 3-5** indicates that the magnetic field-dependent particle motion is reversible within the measurement uncertainty.

## 3.4 Magnetometry Measurements

### 3.4.1 Vibrating Sample Magnetometry

Vibrating sample magnetometer (VSM) is a scientific instrument used to characterize the magnetic properties of a sample as a function of magnetic field and temperature. A schematic of a VSM is shown in **Figure 3-6**. A VSM consists of two main components, a detection system used to measure the magnetic moment of a vibrating sample and an electromagnet to provide the magnetic field. The detection system includes a sample holder attached to a vibration unit and a set of detection coils surrounding the sample. The electromagnet provides a uniform magnetic field perpendicular to the sample vibration axis. During a measurement, the sample vibrates at frequency $\omega$ and amplitude $A$ creating a change in magnetic flux within the detection coils which induces a voltage $V$,

$$V \propto A\frac{de^{i\omega t}}{dt}m \propto \omega A e^{i\omega t}m \tag{3-2}$$

where $m$ is the magnetic moment of the vibrating sample. A lock-in amplifier is used to measure the voltage signal, which allows for determination of the magnetic moment of the sample as a function of externally applied magnetic field.

A PMC MicroMag 3900 VSM (Lake Shore Cyrotronics™) was used to measure the magnetic properties of MREs at room temperature. Temperature dependent major and minor hysteresis loops were measured by graduate student Nan Tang at the University of

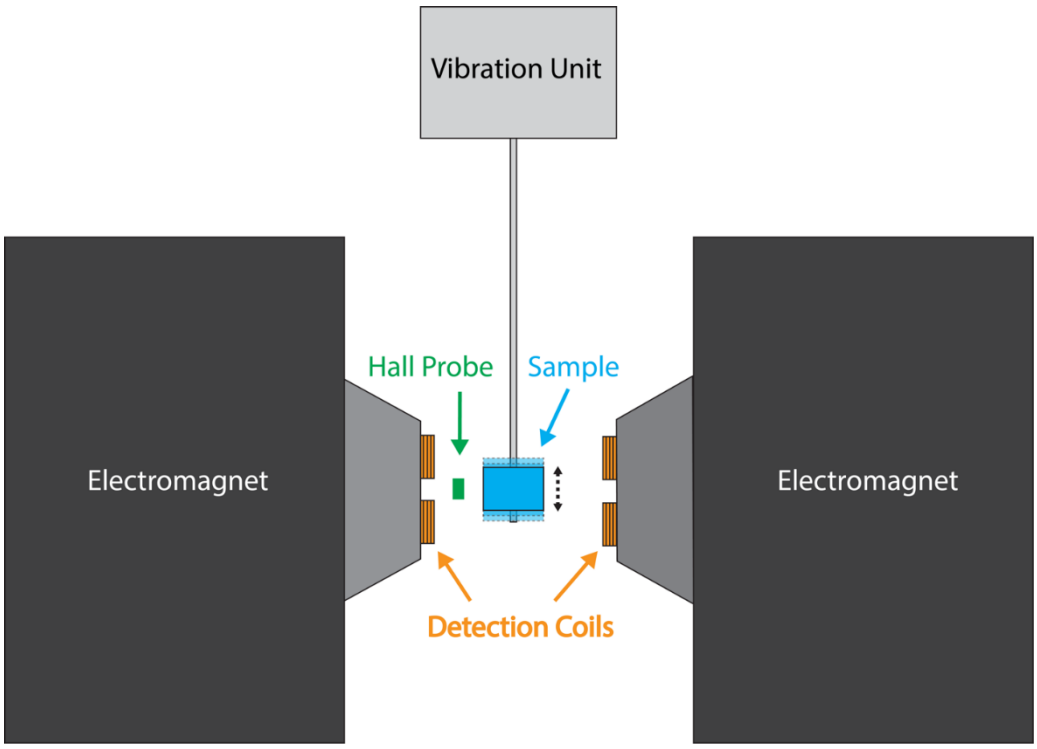


**Figure 3-6** Schematic of a vibrating sample magnetometer.

Tennessee at Knoxville in Professor Dustin Gilbert's laboratory using a Physical Properties Measurement System VSM (Quantum Design).

### 3.4.2 MRE Sample Preparation for VSM Measurements

The MRE samples for VSM measurements were carefully sectioned from the middle of the fabricated MREs and cut to a size of $4 \times 4 \times 1$ mm$^3$ to prevent saturation of the detection system. While the shape of the MRE samples used for magnetometry were all cut to a specific, consistent size to reduce effects of shape anisotropy between the samples, the application of a magnetic field causes the MREs samples to deform along the applied field direction. To understand if this deformation, which changes the sample shape, affects the magnetization reversal, an ultrasoft MRE sample with a volume fraction $\Phi =$

3% of iron particles was measured before and after the sample volume was constrained (**Figure 3-7**). The volume of the sample was constrained by placing the MRE sample on a silicon wafer and encasing it in a two-part epoxy preventing magnetic field-dependent deformation of the sample shape. The first quadrant of the major magnetic hysteresis loops are identical indicating that changes in shape anisotropy due to magnetic field-dependent deformation do not play an important role in the magnetization reversal of MREs.

### 3.4.3 VSM Measurements

The VSM was calibrated before each use by measuring the magnetic saturation moment of an yttrium iron garnet sphere standard (NIST) with known saturation moment of $m_s = 75.13$ memu. Major magnetic hysteresis loops of the MRE samples were measured by decreasing the magnetic field $H$ from 15 kOe to -15 kOe and then increased back up to 15 kOe with a field sweep rate of 100 Oe/s, where 15 kOe is well above the

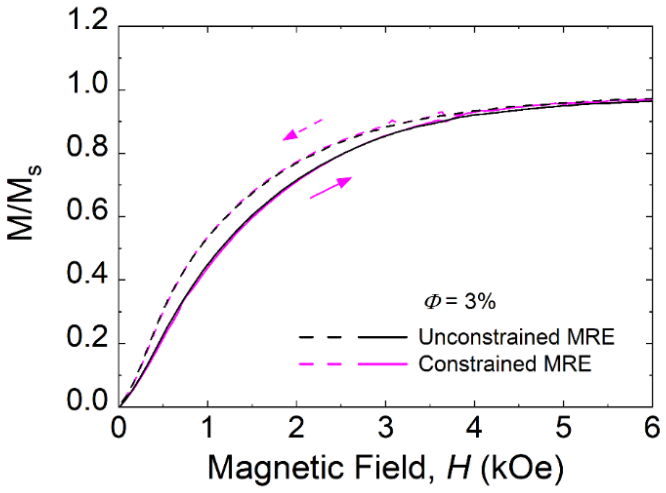


**Figure 3-7** Effect of constraining the MRE sample shape on the magnetization reversal of an ultrasoft MRE. Decreasing (dashed) and increasing (solid) branches of the field-dependent magnetization of an MRE sample with volume fraction $\Phi = 3\%$ of iron particles taken before (black) and after (pink) the sample shape was constrained.

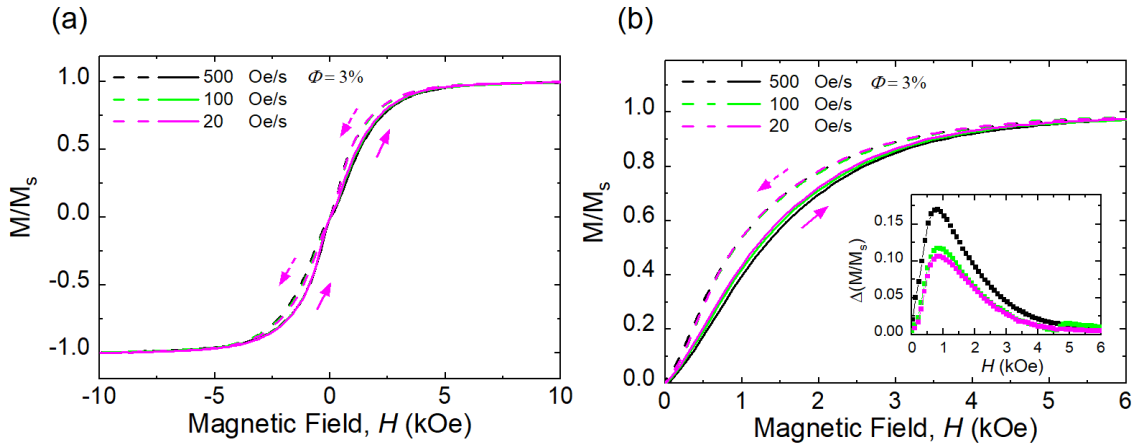


**Figure 3-8** Comparison of varying magnetic field sweep rate on the major magnetic hysteresis loops for an ultrasoft MRE containing volume fraction $\Phi = 3\%$ of iron particles. (a) Major magnetic hysteresis loop for three different magnetic field sweep rates. (b) Zoomed-in view of the first quadrant of the magnetic hysteresis loops with inset showing the field dependence of the calculated loop widening, defined as $\Delta(M/M_s)$, for each sweep rate.

saturation field for all the MRE samples. Similarly, major magnetic hysteresis loops were measured with $H$ cycled between $\pm 15$ kOe and minor hysteresis loops with $H$ cycled between $\pm 5$ kOe using a field sweep rate of 20 Oe/s for MRE sample 1 at selective temperatures between 300 K and 2 K. In all measurements, the magnetic field was applied along the sample plane to remove the effect of shape anisotropy. Caution needs to be taken for selecting the sweep rate of the magnetic field during magnetic hysteresis measurements of MREs. **Figure 3-8** shows magnetic hysteresis loops for an ultrasoft MRE containing volume fraction $\Phi = 3\%$ of iron particles measured at magnetic field sweep rates ranging from $500 - 20$ Oe/s. While the hysteresis loops show a $\approx 30\%$ decrease in the peak widening $(\Delta M/M_s)$ as the magnetic field rate is lowered from 500 Oe/s to 100 Oe/s, the difference between the hysteresis loops measured at the field rates of 100 Oe/s

and 20 Oe/s is negligible. The field sweep rates were chosen to provide sufficient time for the carbonyl iron particles within the MREs to respond to the change in magnetic field.

## 3.5 Characterization of Magnetic Field-dependent Mechanical Properties

### 3.5.1 Custom Design of Magnetic-field Control

Application of a magnetic field to MREs requires careful consideration of the field strength, tunability, uniformity, and geometric restrictions imposed by the characterization equipment. Permanent magnets containing rare earth elements provide a low cost, ergonomic method for applying static magnetic fields. In contrast, electromagnets provide a method for applying dynamic magnetic fields with excellent spatial uniformity. However, electromagnets are expensive, bulky, require active cooling (e.g. water) to maintain a safe operating temperature, and a power supply.

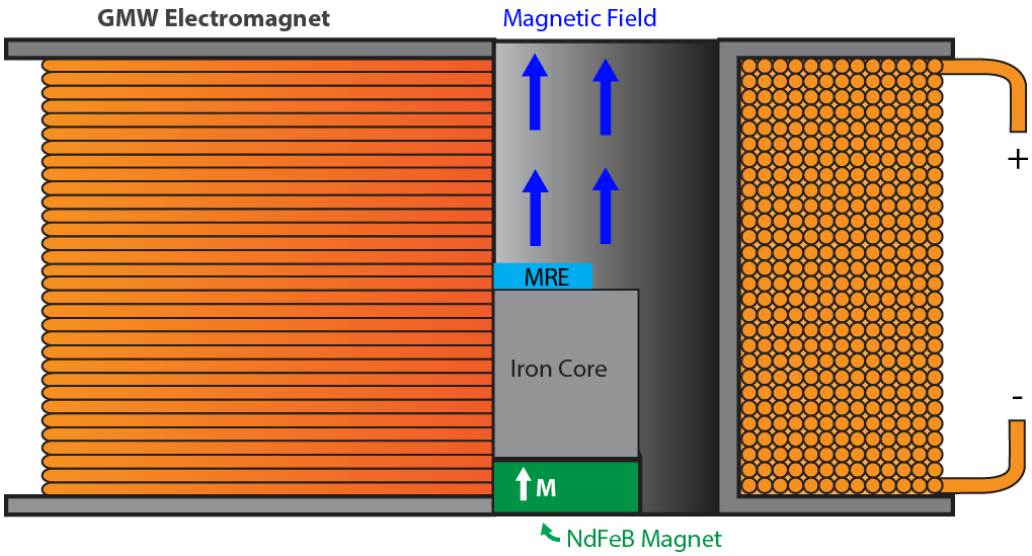


**Figure 3-9** Schematic showing a cross-section of the custom magnetic field application device used to apply magnetic field to the MRE sample during mechanical measurements.

**Figure 3-9** shows a schematic of the custom magnetic field application device used during the mechanical characterization of the MREs, which consists of an electromagnet (GMW Associates©), a soft iron core, and a neodymium iron boride (NdFeB) permanent magnet (CMS Magnets Inc.). The cylindrical iron core, 31.75 mm in diameter and 19.05 mm in height placed inside electromagnet, was used to separate the samples from the NdFeB magnet, magnify the field strength, and improve the field uniformity at the sample. The cylindrical N45 NdFeB magnet, 31.75 mm in diameter and 6.35 mm in height, was placed under the soft iron core. The net magnetic field applied to the MRE is the vector sum of the fields from the electromagnet and the NdFeB magnet, which were also magnified by the iron core. For example, to achieve zero magnetic field at the sample, the current through the electromagnet was set so the magnetic field generated by the electromagnet cancelled that from the permanent magnet.

### 3.5.2 Magnetic Field-dependent Shear Rheology

A Shear rheometer is used to characterize the mechanical properties of a material by measuring its response to a shear deformation. **Figure 3-10** shows a schematic of the main components of the Kinexus™ lab+ rheometer (Malvern Instruments Ltd.) used in this dissertation. The rheometer consists of a stationary bottom plate and a top plate, which moves vertically down onto the sample surface and then rotates. During a measurement, the top plate applies a sinusoidal angular displacement of amplitude $\theta_A$ at frequency $f$, and the torque is measured. The angular displacement and torque are used to calculate the shear strain and shear stress of the disc shaped MRE samples using the following equations,

$$\gamma(t) = \frac{\rho\varphi(t)}{h} \tag{3-3}$$

$$\sigma(t) = \frac{2\tau(t)}{\pi\rho^3} \tag{3-4}$$

where $\rho$ is the radius of the disk sample, $h$ is the height (i.e. thickness) of the sample, $\varphi(t)$ is the angular displacement, $\tau(t)$ is the torque applied by the rheometer plate, $\gamma(t)$ is the shear strain and $\sigma(t)$ is the shear stress. The shear storage modulus ($G'$) and shear loss modulus ($G''$) can be calculated using the following equations,

$$G' = \frac{\sigma_A}{\gamma_A} \tag{3-5}$$

$$G'' = G' \tan(\delta_{lag}) \tag{3-6}$$

where $\gamma_A$ and $\sigma_A$ are the amplitudes of the sinusoidal shear strain and shear stress, respectively and $\delta$ is the phase lag between the shear stress and shear strain.

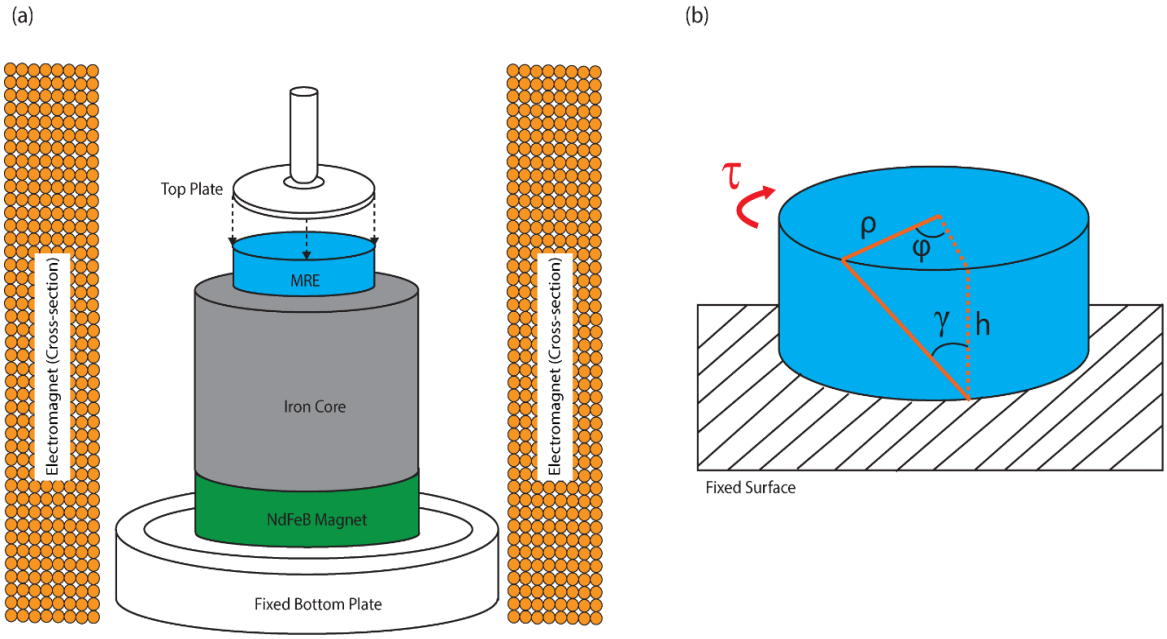


**Figure 3-10** Magnetic field-dependent shear rheology. (a) Schematic of magnetic field-dependent shear rheology measurements. (b) Schematic showing geometry of key parameters in shear rheology.

Shear rheology measurements were performed at Professor Janmey's laboratory at the University of Pennsylvania with guidance provided by graduate student Emile Kraus.

### 3.5.3 Magnetic Field-dependent Compressive Indentation

A microindenter is a scientific instrument used to characterize the mechanical properties of a material in response to compressive indentation. **Figure 3-11** shows a schematic of the custom microindenter used in this dissertation. The microindenter is comprised of a 4 mm diameter spherical ruby probe connected to a 5 mm long cylindrical aluminum rod was mounted onto the end of a calibrated titanium cantilever having normal stiffness $k_{normal} = 1385.9$ N/m. A capacitance probe (Capacitec) having a resolution of 25 µm/V and an optical, linear encoder (Renishaw) was used to measure the deflection of the titanium cantilever. During a measurement, the spherical indenter is brought into

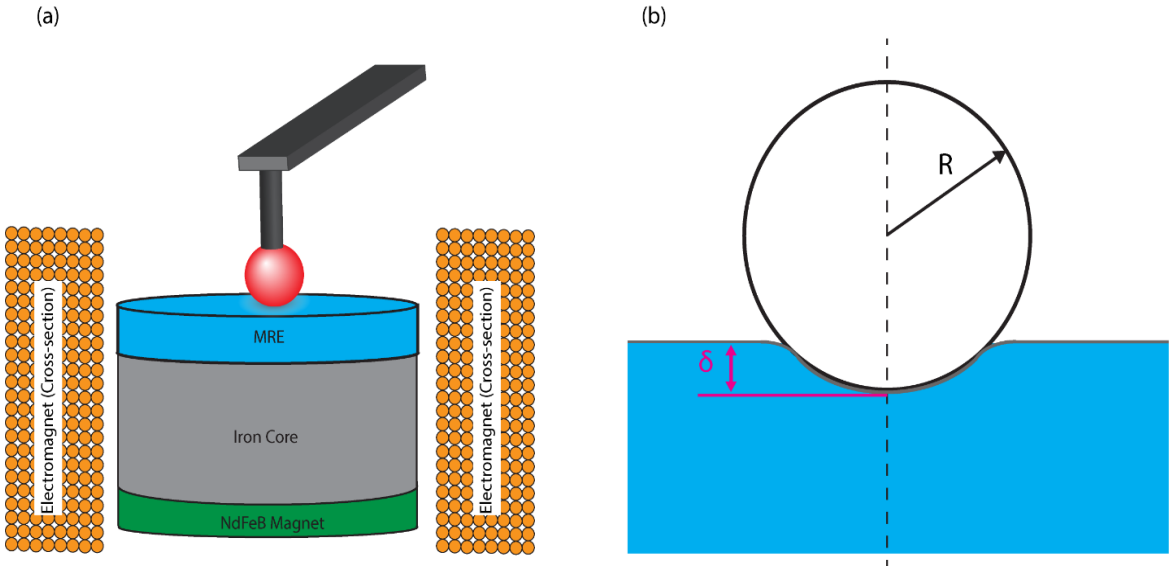


**Figure 3-11** Magnetic field-dependent compressive indentation. (a) Schematic of magnetic field-dependent compressive indentation measurements. (b) Schematic showing spherical probe indenting the MRE surface to indentation depth $\delta$.

contact with the MRE surface up to a target load of $5$ mN at $50$ μm/s and then retracted at the same rate. The elastic modulus was determined by fitting the unloading portion of the indentation force versus depth curve with the JKR adhesive contact model given by the equation,

$$\delta_{depth} = \frac{1}{R}\left[\frac{3R}{4E}(F + 3\Delta\gamma_{fit}\pi R + \sqrt{6\Delta\gamma\pi RF + \left(3\Delta\gamma_{fit}\pi R\right)^2}\right]^{\frac{2}{3}} \qquad (3\text{-}7)$$

where $R$ is the radius of the indenter and the fit parameters are $\Delta\gamma_{fit}$ and $E$ is the elastic modulus. Compressive indentations were performed at Professor Kevin Turner's laboratory at the University of Pennsylvania in collaboration with Dr. Alexander Bennett and at Professor Corbin's laboratory at the University of Delaware in collaboration with graduate student Zheng Cao.

**References for Chapter 3**


[1] R. N. Palchesko, L. Zhang, Y. Sun, and A. W. Feinberg, *Development of Polydimethylsiloxane Substrates with Tunable Elastic Modulus to Study Cell Mechanobiology in Muscle and Nerve*, PloS One **7**, e51499 (2012).

[2] P. Hariharan, *Optical Interferometry*, 2nd ed. (Academic Press, Amsterdam ;, 2003).

[3] M. Quinten, *A Practical Guide to Surface Metrology* (Springer International Publishing, 2019).

[4] R. Dandliker, E. Zimmermann, and G. Frosio, *Electronically Scanned White-Light Interferometry - A Novel Noise-Resistant Signal-Processing*, Opt. Lett. **17**, 679 (1992).

[5] J. Wyant and O. Center, *White Light Interferometry*, **4737**, 10 (n.d.).

[6] A. D. Elliott, *Confocal Microscopy: Principles and Modern Practices*, Curr. Protoc. Cytom. **92**, (2020).

[7] J. Young, Applications of Confocal Microscopy, Master's Thesis, University of Central Oklahoma, 2019.

# Chapter 4: The Effect of Polymer Stiffness and Magnetic Particle Concentration on the Magnetization Reversal of MREs

## 4.1 Introduction

There is an intricate interplay between the mechanical and magnetic properties of MREs. The constituent polymers have a profound effect on the mechanical properties of MREs, which can lead to an interesting change in the magnetization reversal of MREs. For example, magnetic hysteresis loops of MREs consisting of soft polymers display a characteristic pinched loop shape, which has not been observed in rubber-like stiff MREs [1]. Investigations of ultrasoft MREs to date [2] have revealed much larger increases in the elastic moduli than predicted by analytic models that consider stationary magnetic dipoles [3,4]. In contrast to rubber-like MREs, MREs fabricated with soft polymers have been shown to exhibit magnetic field-dependent motion of the magnetic particles within the polymer matrix [1,5,6]. The field-dependent motion of particles within the polymer matrix is thought to be an important contributing factor to the observed loop shape [7–10]. Recent experiments on an MREs that are stiffened by lowering the temperature [11–13] provide compelling evidence that magnetic particle motion is indeed linked to the widening of the magnetic hysteresis loops at intermediate fields. However, temperature-dependent experiments can only examine two stiffnesses. Therefore, a more comprehensive examination of the effect of polymer stiffness and magnetic particle concentration that includes both experiments and modeling is needed.

This chapter presents a systematic investigation of the effect of polymer stiffness and magnetic particle concentration on the magnetization reversal of MREs. A series of MREs with elastic moduli systematically varied over the range from ultrasoft to rubber-like, achieved by varying polymer composition, and ultrasoft MREs with varied concentration of magnetic particles were studied by magnetometry. While cooling an ultrasoft polymer has the advantage that the measurements can be done on the same sample, only two stiffnesses can be reliably accessed. The measurements presented in this chapter cover a wide range of stiffnesses and confirm that hysteresis loops measured in the same ultrasoft MRE at low temperatures where the polymer is rigid are identical to the room temperature hysteresis loops from rubber-like MREs synthesized with stiffer polymers. Furthermore, the hysteresis loops are compared to theoretical hysteresis loops calculated using a simple two-dipole model that captures the magneto-mechanical coupling in MREs. The model reproduces the key features of the experimentally observed trends in the hysteresis loops and provides insight into the physical mechanisms of the MRE hysteresis. Moreover, the results provide evidence that motion of the magnetic particles, particularly along the direction of the applied field, plays a defining role in the magnetic hysteresis loop widening.

### 4.2 Magnetization Reversal of Ultrasoft MREs

A major magnetic hysteresis loop of an ultrasoft MRE containing $\Phi = 3\%$ volume fraction of iron particles (sample 1) is shown in **Figure 4-1a** with a zoomed-in view of the first quadrant shown in **Figure 4-1b**. The hysteresis loops show a remanence of almost 0 ($M_r/M_s = (3.92 \pm 0.01) \times 10^{-3}$) and a small coercive field ($H_C = 14 \pm 1$ Oe). More

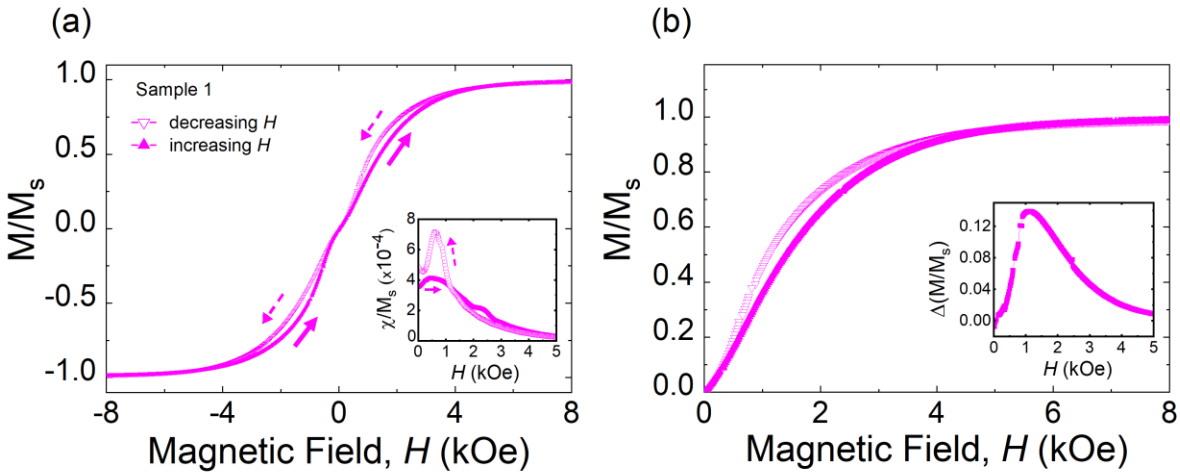


**Figure 4-1** Room temperature magnetic properties of an ultrasoft MRE. (a) Major magnetic hysteresis loop of an ultrasoft MRE with a volume fraction $\Phi = 3\%$ of iron particles (sample 1) showing zero remanent magnetization and a characteristic loop widening at intermediate fields. The inset compares the normalized differential magnetic susceptibility $\chi/M_s$ for increasing and decreasing $H$ branches, where a 5-point averaging was applied to reduce random noise. (b) Zoomed-in view of the first quadrant of the major magnetic hysteresis loop shown in (a) highlighting the characteristic loop widening. Inset shows the field dependence of the loop widening, $\Delta(M/M_s)$, defined as the difference in magnetization between the two branches at each specific $H$. Reproduced from [15], with the permission of AIP Publishing.

importantly, the loop opens up at intermediate fields and close again near the saturation field, which is referred to as loop widening. The loop widening is quantified by $\Delta M/M_s$, defined as the difference in magnetization between the two branches of the hysteresis loop at each $H$. The field-dependence of the loop widening is shown in the inset of **Figure 4-1b**. The loop widening can also be highlighted by comparing the differential magnetic susceptibility, defined as $\chi = dM/dH$, for both increasing and decreasing branches, as shown in the inset of **Figure 4-1a** normalized by $M_s$. The observed loop widening in ultrasoft MREs shown in **Figure 4-1** is consistent with previous reports where the authors attributed the loop widening to the magnetic particle motion in MREs [1,11–13].

### 4.3 The Effect of Polymer Stiffness on Magnetization Reversal of MREs

The stiffness of the constituent polymer can be tuned to impede the field-dependent motion of magnetic particles. If the observed loop widening indeed arises from the motion of magnetic particles within the polymer, then the loop widening should systematically decrease as the polymer stiffness is increased. The effect of polymer stiffness on the magnetization reversal of MREs was investigated by measuring major magnetic hysteresis loops of MREs having Young's moduli $E$ ranging from $\approx 9\ kPa$ (ultrasoft) to $\approx 2{,}400\ kPa$ (rubber-like) as listed in **Table 4-1**. **Figure 4-2** shows the major magnetic hysteresis loops of MRE samples 1-4. A zoomed-in view of the first quadrant is shown in **Figure 4-2**, where the measured loop widening (inset **Figure 4-2b**) monotonically decreases with increasing constituent polymer stiffness. The peak value of the characteristic loop widening for MRE sample 4 (stiffest) is about 10% of the peak value for MRE sample 1 (softest).

The effects of polymer stiffness on the magnetization reversal of MREs can also be investigated on a single MRE sample by varying the temperature. Reducing the temperature below the melting point of PDMS $T_m \approx 230$ K results in a phase transition of

| MRE Sample | Polymer type | Sylgard™ 527: Sylgard™184 (by w.t.) | $E$ (kPa) |
|---|---|---|---|
| 1 | Polymer A | 1:0 | $8.7 \pm 0.6$ |
| 2 | Polymer B | 10:1 | $50 \pm 2$ |
| 3 | Polymer C | 5:1 | $106 \pm 1$ |
| 4 | Polymer D | 0:1 | $2{,}400 \pm 400$ |

**Table 4-1** MRE samples containing $\Phi = 3\%$ of iron particles and varying Young's moduli $E$ by mixing different ratios by weight of commercial polymers Sylgard™ 527 and Sylgard™ 184. The Young's moduli were measured at zero magnetic field by compressive indentation.

the polymer to a crystalline state, and consequently, the Young's modulus increases by several orders of magnitude [11–14]. The first quadrant of the temperature-dependent major magnetic hysteresis loops of MRE sample 1 is shown in **Figure 4-3a**. The major magnetic hysteresis loops measured at 300 K and 250 K (above $T_m$) overlap and both show loop widening. However, when the temperature is lowered to 200 K (below $T_m$), no characteristic loop widening is observed similar to what was observed for the MRE sample 4 (stiffest) measured at 300 K. The field dependence of that magnetic susceptibility $\chi$, shown in the inset of **Figure 4-3a**, suggest that it is easier for the magnetic moments in softer MREs to be aligned along the applied field direction. **Figure 4-3b** shows the field-cooled (FC) minor hysteresis loops where the applied magnetic field was cycled between $\pm 5$ kOe at selected temperatures between 300 K and 2 K. The minor loops measured above $T_m$ all overlap with loop widening as expected, and those measured below $T_m$ also overlap but exhibit no loop widening. Interestingly, the slope trend observed for FC minor loops suggest the opposite –it is easier for the magnetic moments at lower temperatures (stiffer) to align along the applied field direction.

**Figure 4-3c** compares the major loops and FC-minor loops of the same MRE sample 1 measured at 300 K $> T_m$ (softer) and 200 K $< T_m$ (stiffer). At 300 K, the major loops both overlap as expected. However, the normalized magnetization of the major loop at 200 K is significantly smaller than that of the FC-minor loops at the same field. This difference, which is explained below, suggests that the magnetic particle spacing in MREs affects the magnetization reversal. Lowering the temperature below $T_m$ increases the stiffness of the MRE by several orders of magnitude such that the particles are frozen in place. Decreasing the temperature from above to below $T_m$ in $H = 5$ kOe freezes the

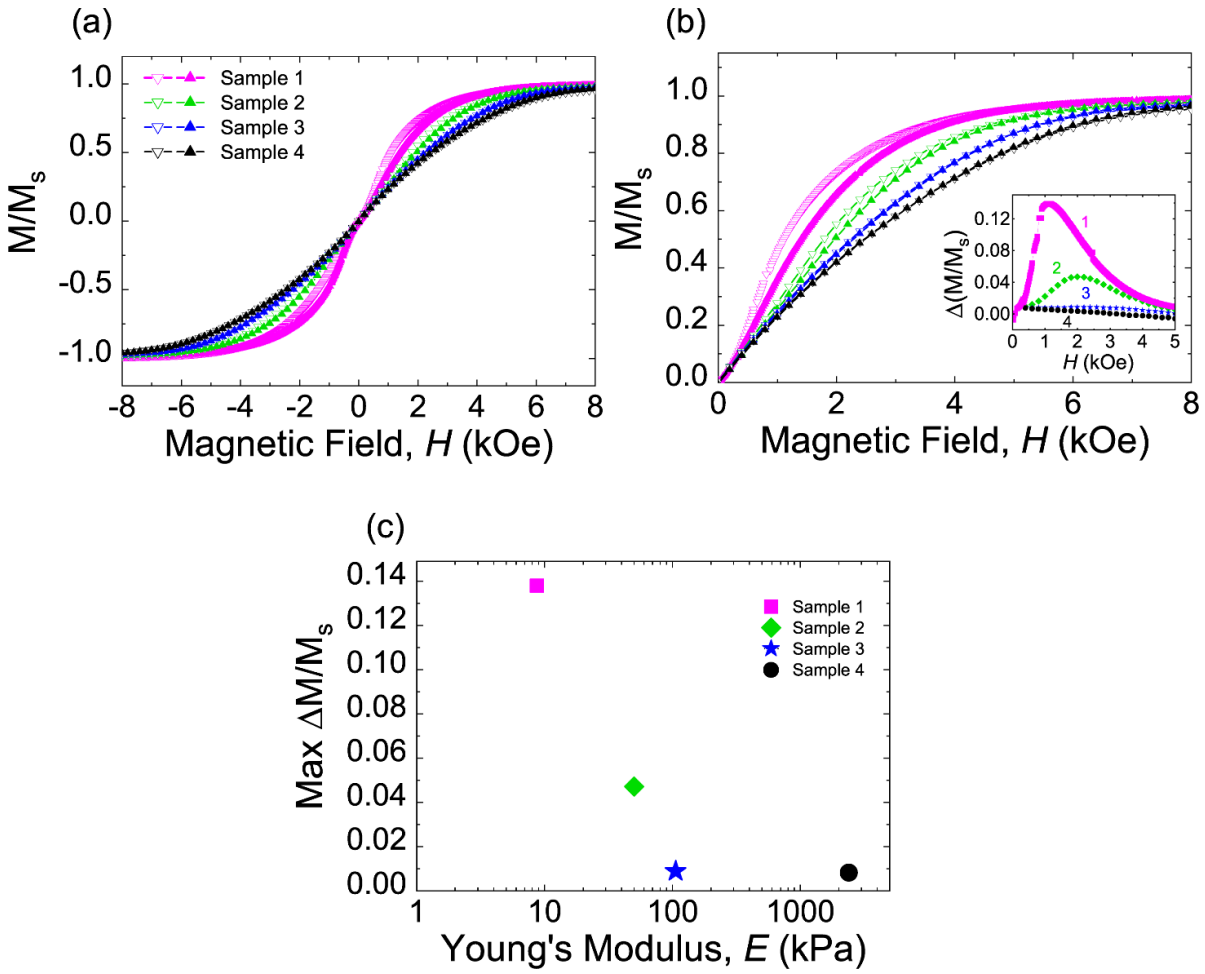


**Figure 4-2** The effect of varying constituent polymer stiffness by composition on the magnetization reversal of MREs. (a) Major magnetic hysteresis loops on MREs samples synthesized with polymers having different stiffnesses ranging from ultrasoft (A) to rubber-like (D) with volume fraction $\Phi = 3\%$ of iron particles. (b) Zoomed-in view of the first quadrant showing a decrease in characteristic loop widening and magnetic susceptibility with increasing constituent polymer stiffness. Inset shows the field-dependent loop widening at each specific $H$. (c) Maximum $\Delta(M/M_s)$ as a function of Young's modulus for MRE samples 1-4. Reproduced from [15], with the permission of AIP Publishing.

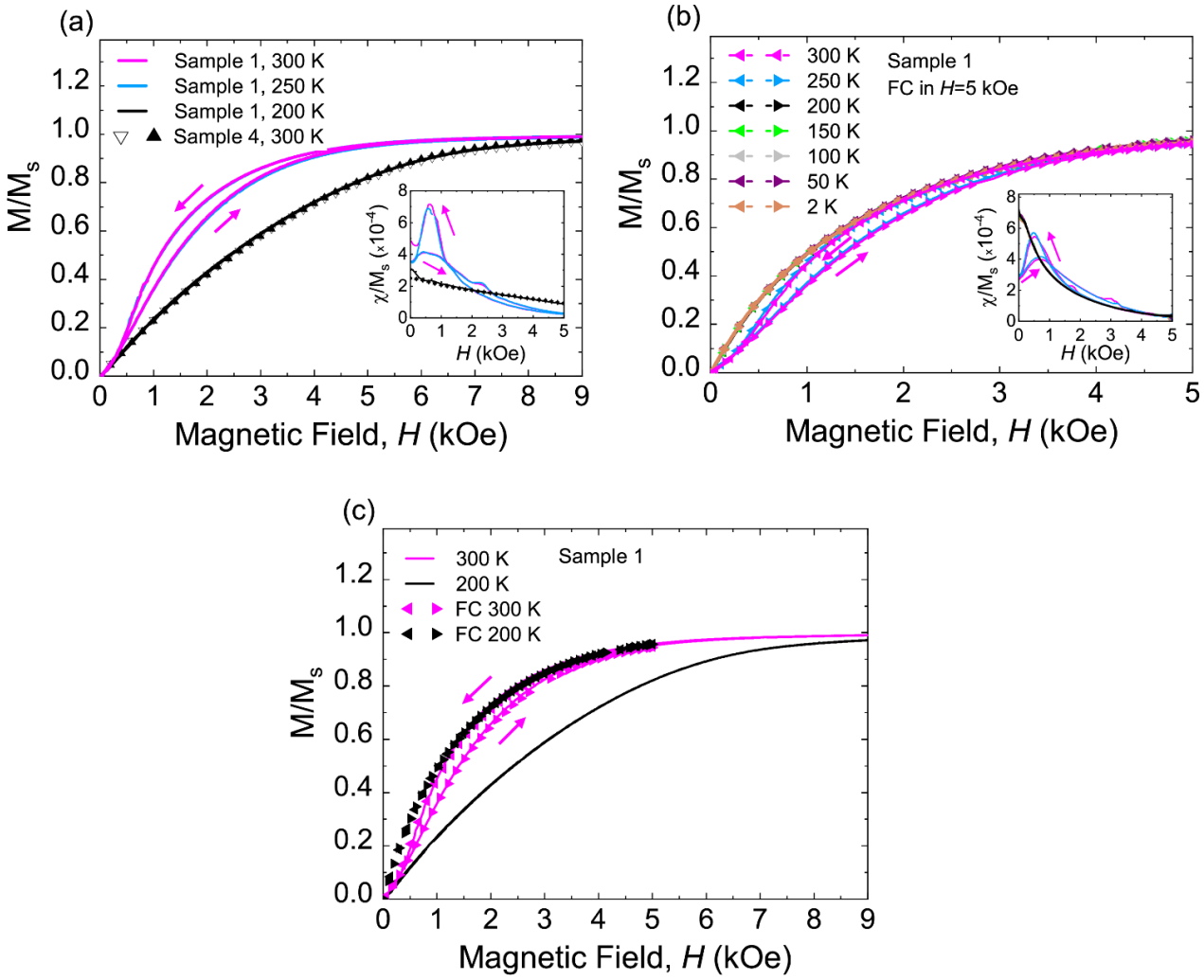


**Figure 4-3** The effect of tuning the constituent polymer stiffness by temperature on the magnetization reversal of MRE sample 1. Zoomed-in view of the first quadrant of the major magnetic hysteresis loops of ultrasoft MRE sample 1 measured at 300K, 250K, and 200K where a rubber-like (D) MRE measured at 300 K is included for comparison. The inset shows the slope of the normalized magnetization, $\chi/M_s$ at each specific $H$. (b) Field-cooled minor magnetic hysteresis loops on the same ultrasoft (A) MRE sample measured in (a) with inset showing field-dependent $\chi/M_s$ at each specific $H$ at different temperatures. (c) Comparison of major loops and FC minor loops of MRE sample 1 at temperatures above (softer) and below (stiffer) $T_P$. Reproduced from [15], with the permission of AIP Publishing.

particles at their locations from the previous FC-minor loop measured above $T_m$. The magnetic particles are consequently closer together on average, which results in larger dipolar interactions between neighboring particles, as compared to the zero-field cooling case at 200 K for the same $H$. Thus, the normalized magnetization of the FC-minor loop is larger at low to intermediate fields than the zero-field cooling case, which can be further highlighted by comparing $\chi/M_s$ values near zero field. As shown in the insets of **Figure 4-3**, the $\chi/M_s$ near remanence below $T_m$ is approximately 2.6 times larger for the minor loop as compared to the major loop, and the minor loop $\chi/M_s$ is larger than the corresponding value measured above $T_m$.

### 4.4 The Effect of Magnetic Particle Concentration on the Magnetization Reversal of Ultrasoft MREs

Magnetic particle spacing can also be tuned by adjusting the concentration of magnetic particles in the MRE. To further investigate the effect of magnetic particle spacing on the magnetization reversal of MREs, room temperature major magnetic hysteresis loops were measured of MREs containing the same ultrasoft polymer, but with varying volume fraction of iron particles ranging from $\Phi = 3 - 40\%$ (**Figure 4-4a**). As $\Phi$ increases, the average iron particle spacing decreases, and consequently, the particles have less available space to move, which reduces the loop widening (**Figure 4-4b**). Since the iron particles at higher volume fractions are closer together, they also experience larger stray magnetic fields resulting in larger magnetic moments for each particle at a given $H$. As expected, $\chi/M_s$ near remanence is largest for the highest volume fraction $\Phi = 40\%$ of

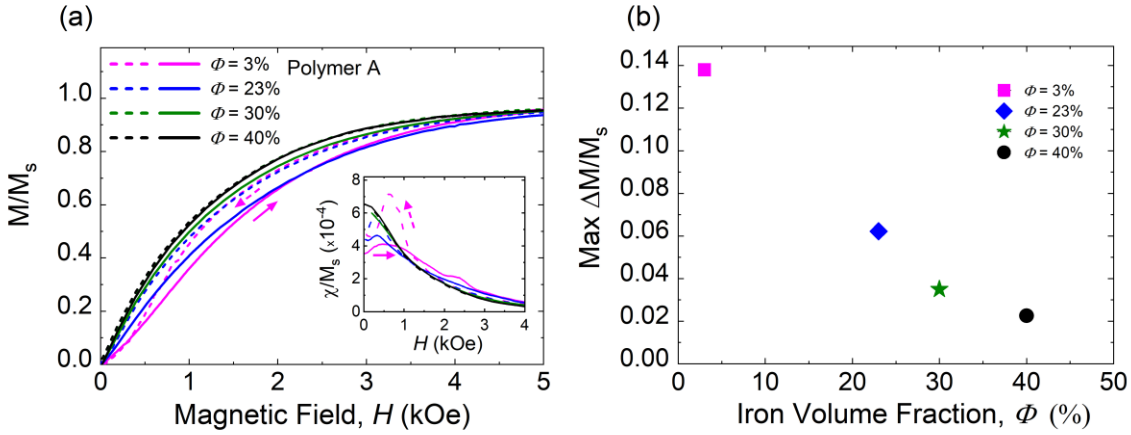


**Figure 4-4** The effect of varying iron particle spacing on the magnetization reversal of ultrasoft MREs. Zoomed-in view of the major magnetic hysteresis loops of MREs synthesized with polymer A and varying volume fractions $\Phi$ of iron particles. The inset shows the field slope of the normalized magnetization, $\chi/M_s$, at each specific $H$ where a 5-point averaging was applied to reduce random noise. (b) Maximum $\Delta(M/M_s)$ as a function of volume fraction of iron particles. Reproduced from [15], with the permission of AIP Publishing.

iron particles and decreases monotonically as the volume fraction of iron particles decreases, as shown in the inset of **Figure 4-4a**.

### 4.5 Role of Magnetic Particle Motion on the Magnetization Reversal of MREs

The results presented in this chapter so far have highlighted the importance of polymer stiffness and particle spacing on the magnetization reversal of MREs. To further understand the effect of stiffness and particle spacing on the magnetization reversal of MREs, a simple two-dipole model that captures the magneto-mechanical coupling in MREs was developed in collaboration with graduate student David Marchfield. The model, similar to approaches used recently in the field [7–10], consists of two spherical particles having diameter $D$, saturation magnetization $M_s$, and connected to each other via a spring

having stiffness constant $k$ as shown in the inset of **Figure 4-5d**. Each magnetic particle was modeled as a point magnetic dipole, a valid assumption despite the complex internal spin distributions an individual particle undergoes during their magnetization reversal (see section 2.4.1). The net magnetic moment of each particle when below magnetic saturation is,

$$m = MV = \chi_{sph} H_{eff} V \tag{4-1}$$

where $\chi_{sph}$ is the magnetic susceptibility of a single sphere, $H_{eff}$ is the effective field at the center of each particle due to applied magnetic field and the stray magnetic field from the other particle, and $V$ is the volume of the sphere. At or above magnetic saturation, the dipole moment equals $m = M_s V$. The magneto-mechanical force between the two particles when **H** is applied parallel to the spring is given by,

$$F = -k(S - S_o) - \frac{3\mu_o m^2}{2\pi S^4} \tag{4-2}$$

where $S$ is the inter-particle separation, and $S_o$ is the elastic equilibrium separation at $H = 0$. The first term in Equation 4-2 is the elastic restoring force modeling the elastomeric polymer matrix, and the second term is the magnetic dipole-dipole interaction force which is attractive when **H** is applied along the line connecting the two spheres. Major magnetic hysteresis loops were calculated by finding the equilibrium (i.e. $F = 0$) at each $H$ value as $H$ was cycled from $+15$ kOe to $-15$ kOe and back. The energy of the system is related to the force by $F = -\nabla E_{Total}$ and a non-linear conjugate gradient method was used to determine the $m$ and $S$ associated with the local energy minimum. Modeling was conducted for two selected $k$ values, $k = 9 \times 10^{-3}$ N/m and $k = 9 \times 10^{-1}$ N/m with $S_o = 12.0$ μm, particle diameter $D = 3$ μm, $M_s = 1.4 \times 10^6$ A/m, and $\chi_{sph} = 2$.

**Figure 4-5** compares the magnetic field-dependent particle motion and corresponding major magnetic hysteresis loops calculated for $S_o = 12$ μm with spring constants: $k = 9 \times 10^{-3}$ N/m and $k = 9 \times 10^{-1}$ N/m. An approximate equivalent Young's modulus $E$ can be obtained by considering the spring as a cylinder being compressed from both sides, as described in section 2.2.2, giving a relationship between $k$ and $E$ given by $E = 2kS_0/\pi D^2$. Thus, the softest and stiffest spring constants have an

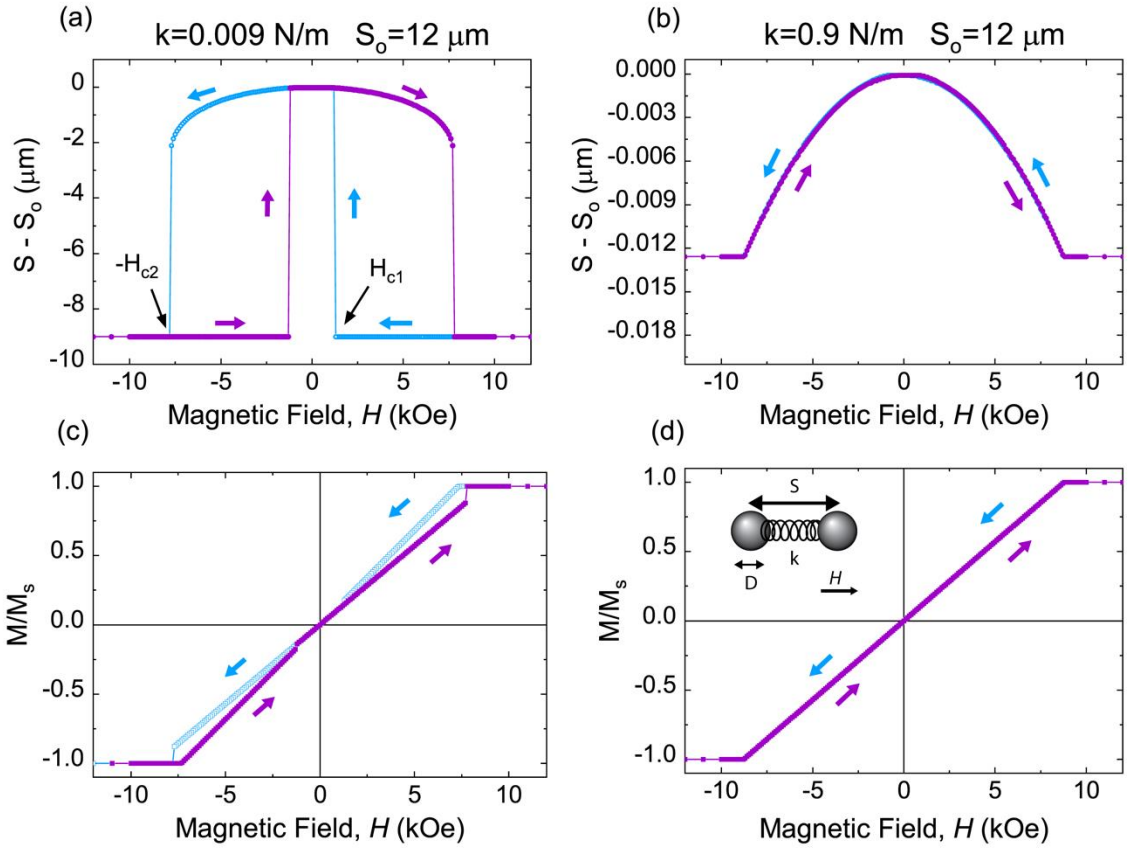


**Figure 4-5** The two-particle magneto-mechanical model results for the same elastic equilibrium separation ($H = 0$) of $S_o = 12$ μm with different stiffness constants: $k = 9 \times 10^{-3}$ N/m (a,c) and $k = 9 \times 10^{-1}$ N/m (b, d). The magnetic field-dependent inter-particle displacement, defined as $(S - S_o)$, and the corresponding major magnetic hysteresis loops are shown in (a,b) and (c,d), respectively. The inset of (d) shows a cartoon schematic of the two-particle model. Reproduced from [15], with the permission of AIP Publishing.

approximate Young's moduli of $E \approx 8\ kPa$ and $\approx 800\ kPa$, respectively, which is representative of MRE sample 1 (softest) and MRE sample 4 (stiffest) considered in the experiments, respectively. For $H$ at or above magnetic saturation, the magnetic particles are saturated and are at their closest distance due to the attractive dipole-dipole forces. When $H$ is reduced below saturation, $m$ decreases since $m$ is proportional to $H_{eff}$ and, consequently, the magnitude of the dipole-dipole force decreases until it reaches zero at $H = 0$. In the softest case (**Figure 4-5a and 4-5c**) the restoring elastic force from the spring is small and the particles touch ($S = D$), which is referred to as the clustered state, at magnetic saturation because the dipole-dipole force exceeds the elastic force trying to pull the particles apart. The particles remain in contact until $H$ is decreased to a critical value, denoted here as $H_{c1}$, where the attractive dipole-dipole force becomes sufficiently small enough that the elastic force can pull the particles apart, as the clustered state is no longer a local minimum energy state, and a jump in $S$ is observed. Decreasing $H$ down further to $H = 0$ causes $S$ to increase gradually until it reaches a maximum of $S = S_o$ at $H = 0$. As the magnetic field is decreased below zero, **H** increase in magnitude but now in the opposite direction, the particles are attracted to each other and $S$ decreases gradually at first until the particles touch once again at $H_{c1}$ since the separated state is no longer an available minimum energy state.

**Figure 4-5c** shows the corresponding magnetic response, which exhibits zero remanent magnetization within the uncertainty of the calculations and a pinched loop shape that is qualitatively similar to what is observed experimentally (**Figure 4-1**) and also to recent modeling results for a similar system [8]. For larger $k$, shown in **Figure 4-5b and 4-5d**, the elastic force is so large that the clustered state is not an available minimum energy

state, resulting in no hysteresis in the particle motion and consequently no magnetic response. When **H** is applied perpendicular to **S** instead of parallel to **S**, the dipole-dipole interactions are repulsive, and no loop widening is observed.

The two-particle modeling results provide insight into the role of attractive inter-particle interactions in the hysteretic magnetic response. However, in a real sample, there is a distribution of particle sizes and equilibrium positions. To better account for the effects associated with an ensemble of particles, a distribution of equilibrium positions ranging from $S_o = 3.2$ to 13.0 μm in steps of 0.2 μm was considered. A weighted average was performed on the calculated hysteresis loops using a Gaussian distribution, having a mean and standard deviation of 4.8 and 6.5 μm, respectively. A zoomed-in view of the first quadrant for the weighted average hysteresis loops calculated for $k = 9 \times 10^{-1}, 9 \times 10^{-2}$,

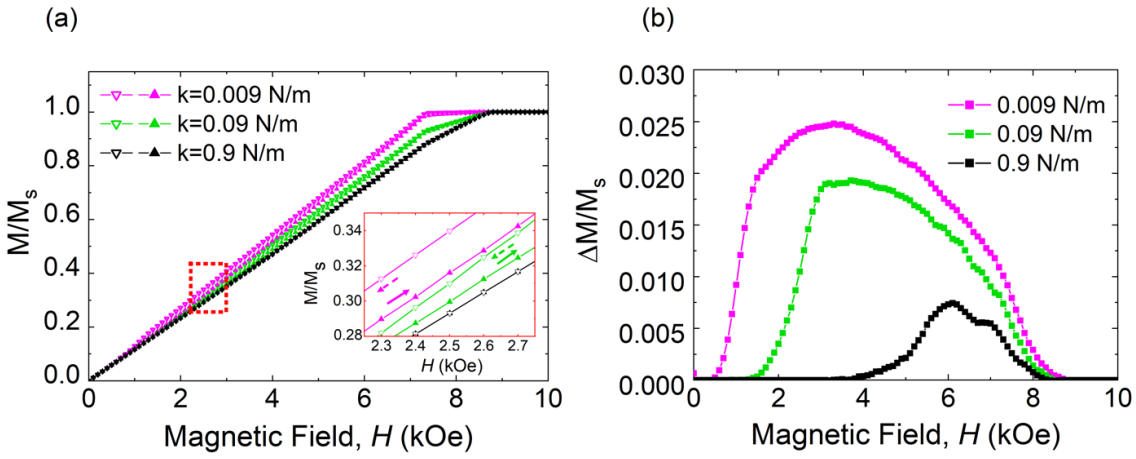


**Figure 4-6** The effect of stiffness constants ($k = 9 \times 10^{-1}$, $9 \times 10^{-2}$, and $9 \times 10^{-3}$ N/m) on magnetic hysteresis loops calculated from the two-particle model by taking a weighted average of a collection of hysteresis loops from a distribution of $S_o$ values ranging from 3.2 to 13.0 μm. (a) The first quadrant of weighted average hysteresis loops with inset showing a zoomed-in view of the loop widening at intermediate fields. (b) Calculated $\Delta(M/M_s)$ vs. $H$ for different $k$'s, where a five-point averaging was applied. Reproduced from [15], with the permission of AIP Publishing.

and $9 \times 10^{-3}$ N/m is shown in **Figure 4-6a**. Increasing $k$ results in a decrease in loop widening, which is highlighted explicitly in **Figure 4-6b** and agrees well with the experimentally observed trends in **Figure 4-2**. The modeling also shows that when $k$ is increased while $S_o$ is decreased, as in the FC case, results in an increase in the zero-field susceptibility consistent with the increase in $\chi/M_s$ at near remanence observed in **Figure 4-3b** as compared to **Figure 4-3a** for MRE sample 1 below $T_m$.

## 4.6 Conclusions

In this chapter, the effects of polymer stiffness and magnetic particle concentration on the magnetization reversal of MREs were investigated experimentally and with modeling. The observed characteristic loop widening in the magnetic hysteresis loops at intermediate field monotonically decreases as the polymer stiffness increases, which can be tuned by varying polymer composition or temperature. Furthermore, hysteresis loops measured in the same ultrasoft MRE at temperatures below the polymer's melting point are identical to the room temperature hysteresis loops measured for rubber-like MREs synthesized with stiffer polymers and the same concentration of magnetic particles. A two-dipole model that captures the magneto-mechanical coupling in MREs shows that the loop widening arises from a bistability of inter-particle displacements along the applied magnetic field direction. Despite the model's simplicity, it produces calculated magnetic hysteresis loops that show a widening trend that qualitatively matches the experimental hysteresis loops for MREs with varying polymer stiffnesses and spacing of magnetic particles. The results presented in this chapter provide guidance for the magnetic field

control of MREs with a wide range of stiffnesses and volume fraction of magnetic particles in biomedical and other applications.

The results presented in this chapter have been published in the peer-reviewed journal Applied Physics Letters Materials entitled "The Effect of Polymer Stiffness on Magnetization Reversal of Magnetorheological Elastomers" [15].

**References for Chapter 4**


[1] G. V. Stepanov, D. Y. Borin, Y. L. Raikher, P. V. Melenev, and N. S. Perov, *Motion of Ferroparticles inside the Polymeric Matrix in Magnetoactive Elastomers*, J. Phys.: Condens. Matter **20**, 204121 (2008).

[2] M. Mayer, R. Rabindranath, J. Börner, E. Hörner, A. Bentz, J. Salgado, H. Han, H. Böse, J. Probst, M. Shamonin, G. J. Monkman, and G. Schlunck, *Ultra-Soft PDMS-Based Magnetoactive Elastomers as Dynamic Cell Culture Substrata*, PLoS ONE **8**, e76196 (2013).

[3] M. R. Jolly, J. D. Carlson, and B. C. Muñoz, *A Model of the Behaviour of Magnetorheological Materials*, Smart Mater. Struct. **5**, 607 (1996).

[4] L. Chen and S. Jerrams, *A Rheological Model of the Dynamic Behavior of Magnetorheological Elastomers*, Journal of Applied Physics **110**, 013513 (2011).

[5] T. Gundermann and S. Odenbach, *Investigation of the Motion of Particles in Magnetorheological Elastomers by X-μCT*, Smart Mater. Struct. **23**, 105013 (2014).

[6] G. Pessot, M. Schümann, T. Gundermann, S. Odenbach, H. Löwen, and A. M. Menzel, *Tunable Dynamic Moduli of Magnetic Elastomers: From Characterization by x-Ray Micro-Computed Tomography to Mesoscopic Modeling*, J. Phys.: Condens. Matter **30**, 125101 (2018).

[7] M. Puljiz, S. Huang, K. A. Kalina, J. Nowak, S. Odenbach, M. Kästner, G. K. Auernhammer, and A. M. Menzel, *Reversible Magnetomechanical Collapse: Virtual Touching and Detachment of Rigid Inclusions in a Soft Elastic Matrix*, Soft Matter **14**, 6809 (2018).

[8] M. V. Vaganov and Y. L. Raikher, *Effect of Mesoscopic Magnetomechanical Hysteresis on Magnetization Curves and First-Order Reversal Curve Diagrams of Magnetoactive Elastomers*, J. Phys. D: Appl. Phys. **53**, 405002 (2020).

[9] A. M. Biller, O. V. Stolbov, and Yu. L. Raikher, *Mesoscopic Magnetomechanical Hysteresis in a Magnetorheological Elastomer*, Phys. Rev. E **92**, 023202 (2015).

[10] A. Yu. Zubarev, D. N. Chirikov, D. Yu. Borin, and G. V. Stepanov, *Hysteresis of the Magnetic Properties of Soft Magnetic Gels*, Soft Matter **12**, 6473 (2016).

[11] A. V. Bodnaruk, A. Brunhuber, V. M. Kalita, M. M. Kulyk, A. A. Snarskii, A. F. Lozenko, S. M. Ryabchenko, and M. Shamonin, *Temperature-Dependent Magnetic Properties of a Magnetoactive Elastomer: Immobilization of the Soft-Magnetic Filler*, Journal of Applied Physics **123**, 115118 (2018).

[12] A. V. Bodnaruk, A. Brunhuber, V. M. Kalita, M. M. Kulyk, P. Kurzweil, A. A. Snarskii, A. F. Lozenko, S. M. Ryabchenko, and M. Shamonin, *Magnetic Anisotropy in Magnetoactive Elastomers, Enabled by Matrix Elasticity*, Polymer **162**, 63 (2019).
[13] A. V. Bodnaruk, V. M. Kalita, M. M. Kulyk, A. F. Lozenko, S. M. Ryabchenko, A. A. Snarskii, A. Brunhuber, and M. Shamonin, *Temperature Blocking and Magnetization of Magnetoactive Elastomers*, Journal of Magnetism and Magnetic Materials **471**, 464 (2019).
[14] J. Osicka, M. Mrlik, M. Ilcikova, B. Hanulikova, P. Urbanek, M. Sedlacik, and J. Mosnacek, *Reversible Actuation Ability upon Light Stimulation of the Smart Systems with Controllably Grafted Graphene Oxide with Poly (Glycidyl Methacrylate) and PDMS Elastomer: Effect of Compatibility and Graphene Oxide Reduction on the Photo-Actuation Performance*, Polymers **10**, 832 (2018).
[15] A. T. Clark, D. Marchfield, Z. Cao, T. Dang, N. Tang, D. Gilbert, E. A. Corbin, K. S. Buchanan, and X. M. Cheng, *The Effect of Polymer Stiffness on Magnetization Reversal of Magnetorheological Elastomers*, APL Materials **10**, 041106 (2022).

# Chapter 5: The Effect of Magnetic Particle Concentration on the Mechanical Properties of Ultrasoft MREs

## 5.1 Introduction

Magnetorheological elastomers have the unique advantage of reversible modulation of their mechanical properties via an applied magnetic field. In particular, ultrasoft MREs with a base elastic modulus of several kPa offer an innovative means to mimic biophysical mechanical cues and regulators of cells *in vitro* [1]. More interestingly, a recent study on ultrasoft MREs with volume fraction $\Phi = 30\%$ of iron particles has revealed over an order of magnitude increase in shear modulus at low magnetic fields $\mu_0 H \approx 100$ mT [1], which is much larger than what has been observed for rubber-like MREs [2,3]. However, this study only examines one concentration of magnetic particles and does not consider field-dependent changes in surface topography. Therefore, a more comprehensive investigation of the effect of magnetic particle concentration on the elastic moduli and surface roughness of ultrasoft MREs is needed.

The goal of this chapter is to systematically investigate the effect of magnetic particle concentration on the mechanical properties of ultrasoft MREs. A series of ultrasoft MREs with $\Phi$ varying from 0% to 23% were characterized by shear rheology, compressive indentation, and interferometry. Furthermore, the mechanical properties of ultrasoft MREs are fit to quadratic functions $\Phi$ and $H$.

## 5.2 The Effect of Magnetic Particle Concentration on the Shear Modulus

**Figure 5-1** shows the bulk rheological response of ultrasoft MREs with varying volume fraction of iron particles as a function of magnetic field strength, frequency, and shear strain. The ultrasoft PDMS-based MREs behave as a chemically cross-linked gel for all magnetic field strengths and a broad range of frequencies. The shear storage modulus measured at 1 Hz and in the linear viscoelastic regime ($\gamma_o = 2\%$), increased quadratically with both increasing volume fraction of iron particles and with magnetic field strength (**Figure 5-1a**). In particular, the largest increase in shear storage modulus was observed for $\Phi = 23\%$ that exhibited an increase of up to $\approx 41\times$, which is an order of magnitude larger than the increase in shear storage modulus $\left({G'(H)}/{G'(H=0)}\right)$ reported for isotropic rubber-like MREs subjected to the same range of magnetic field strengths and magnetic particle concentrations [2,3]. It is also important to note that the shear loss modulus is an order of magnitude smaller than the shear storage modulus indicating the response is mainly elastic. The ultrasoft MREs exhibit a slight frequency dependence in the viscoelastic shear moduli over a frequency range of about three orders of magnitude (**Figure 5-1b**). Interestingly, the shear strain amplitude sweeps from $\gamma = 2 - 20\%$ reveal a softening of the viscoelastic shear moduli (**Figure 5-1c**). The largest decrease is observed for ultrasoft MREs containing $\Phi = 23\%$ at the highest magnetic field strength studied, $95.4\ \mathrm{kA/m}$, showing a decrease in viscoelastic moduli by $\approx 1/3$ ($G' \approx 100 \rightarrow 30$ kPa, $G'' \approx 13 \rightarrow 4$ kPa). Typically, collagen and other biopolymer networks exhibit strain-stiffening behavior [4], but the less common strain-softening behavior has also been reported [5]. The observed strain-softening in ultrasoft PDMS-based MREs is more pronounced as the applied magnetic field strength increases.

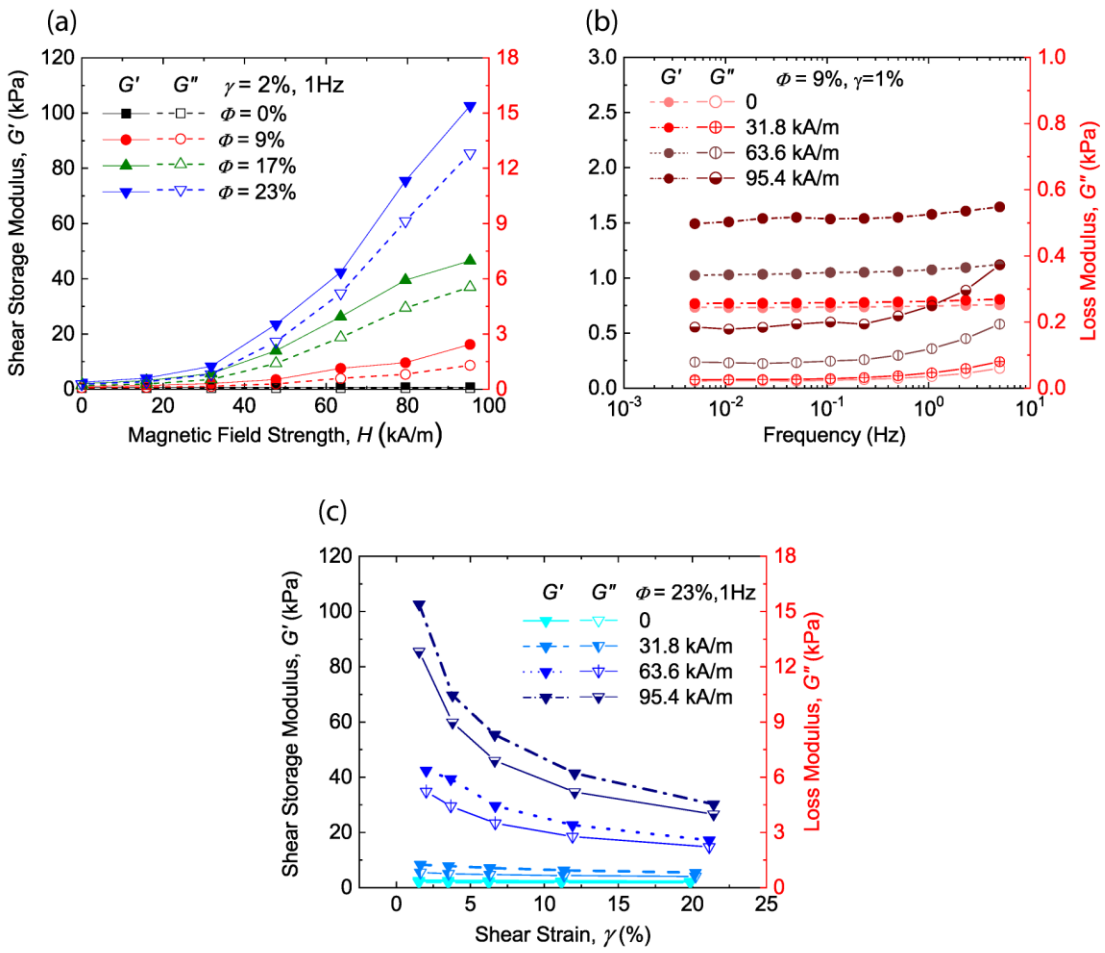


**Figure 5-1** Magnetic field-dependent shear rheology of ultrasoft MREs. (a) Shear storage (solid) and loss (empty) modulus as a function of magnetic field and volume fraction ($\Phi$) of iron particles taken at a frequency of 1 Hz and 2% shear strain. (b) Frequency dependence of the shear moduli for $\Phi = 9\%$ at four different magnetic field strengths. (c) Strain dependence of the shear moduli for $\Phi = 23\%$ at four different magnetic field strengths. Adapted from [3] © IOP Publishing. Reproduced with permission. All rights reserved.

The ability to predict the shear storage modulus as a function of volume fraction of iron particles and magnetic field strength is important for utilizing ultrasoft MREs in biomedical engineering applications, which will be discussed in detail in chapter 6. While analytic models considering fixed position magnetic dipoles have shown success in predicting the magnetic field-dependent increasing in shear storage modulus for rubber-

like MREs [6,7], they fail to predict the large increase observed in ultrasoft MREs. This failure is most likely due to the complex, magnetic field-dependent motion of the iron particles within the polymer matrix as shown in chapter 4. Here, single fit parameter equations with a quadratic dependence on $\Phi$ and $H$ are proposed that predict the mechanical properties of ultrasoft MREs, aiding their integration into the biomedical engineering community.

The inclusion of mechanically rigid iron particles increases the zero-field shear storage modulus of the MREs approximately by the square of the volume fraction of iron particles as shown in **Figure 5-2a**. The dependence of the zero-field shear storage modulus $G_0'$ on the volume fraction $\Phi$ of iron particles can be fit by the following equation,

$$G_0' = 35{,}000\ (\text{Pa})\ \Phi^2 + \ 760\ (\text{Pa}) \tag{5-1}$$

In the magnetic field regime ($H <\approx 100$ kA/m), the shear storage modulus was observed to increase quadratically with respect to the volume fraction of iron particles and applied magnetic field strength (**Figure 5-1a**) and can be fit by the equation,

$$G'(\Phi, H) = \ 760\ (\text{Pa}) + \ 35{,}000\ (\text{Pa})\ \Phi^2 + \alpha \Phi^2 \mu_0 H^2 \tag{5-2}$$

where $G'(\Phi, H)$ is the shear storage modulus of the MRE, $\alpha$ is a fit parameter, $\Phi$ is the volume fraction of iron particles, $\mu_0$ is the vacuum permeability, and $H$ is the applied magnetic field strength. The fit parameter $\alpha = \frac{G'(H) - G_0'}{\Phi^2 \mu_0 H^2} = 134\ (\text{dimensionless})$ was determined by averaging $\alpha$ for each volume fraction of iron particles and applied magnetic field strength. The proposed equation (5-2) fits the experimentally measured data well as shown in **Figure 5-2b** but begins to deviate at volume fractions above the expected percolation threshold, $\Phi_c = 20\%$, for isotropic MREs. At volume fractions above $\Phi_c$, the

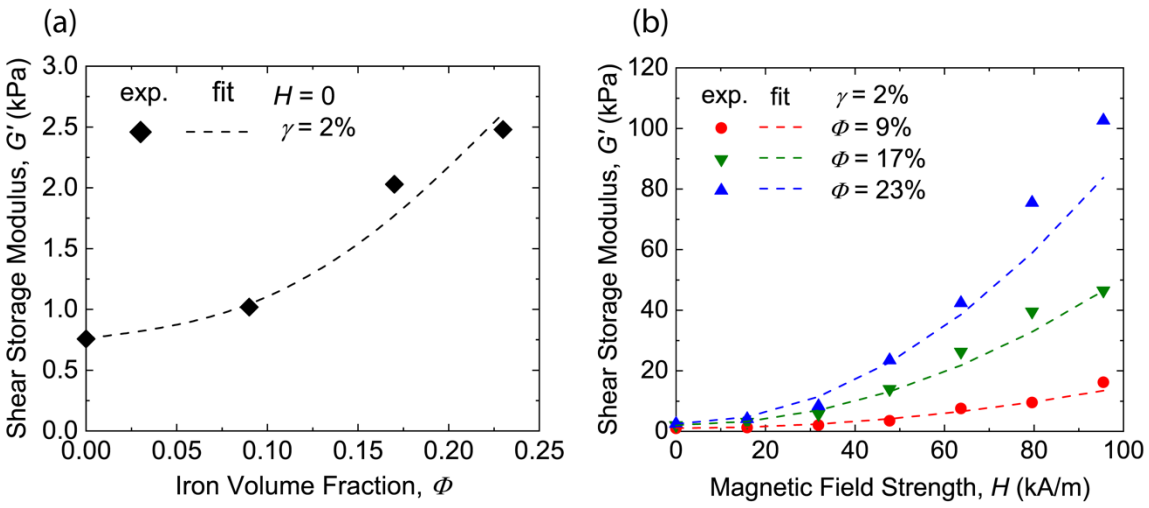


**Figure 5-2** Single fit-parameter equations for shear storage modulus of ultrasoft MREs. (a) The effect of increasing $\Phi$ on the shear storage modulus in the absence of an applied magnetic field ($H = 0$). (b) Comparison of the experimental data (symbol) and fit (dashed) increase in shear storage modulus as a function of magnetic field strength for $\Phi = 9, 17, \text{and } 23\%$. Adapted from [3] © IOP Publishing. Reproduced with permission. All rights reserved.

interparticle contact occurring primarily along the shear direction adds to the bulk rheological response of the MREs [8].

### 5.3 The Effect of Magnetic Particle Concentration on the Young's Modulus

**Figure 5-3** shows the compressive indentation measurements of ultrasoft MREs as a function of volume fraction of iron particles and applied magnetic field strength. Indentation force as a function of the compressive displacement for MREs containing $\Phi = 0$ and 9% are shown in **Figure 5-3a and 5-3b** respectively. MREs with no iron particles exhibit the expected magnetic field-independent indentation force vs depth curve (**Figure 5-3a**). The inclusion of iron particles causes the indentation force vs depth curves to increase monotonically with increasing magnetic field strength (**Figure 5-3b**). The

Young's moduli at each field increment are calculated by fitting the unloading portion of the indentation force vs. depth curves to the JKR adhesive contact model [9] given by the equation,

$$\delta = \frac{1}{R}\left[\frac{2R}{4E}\left(F + 3\Delta\gamma\pi R + \sqrt{6\Delta\gamma\pi RF + (3\Delta\gamma\pi R)^2}\right)\right]^{\frac{2}{3}} \quad (5\text{-}3)$$

where $\delta$ is the indentation depth, R is the radius of the indenter, $E$ is the Young's modulus and the work of adhesion, $\Delta\gamma$, are the fit parameters. The calculated Young's moduli using equation (5-3) are shown in **Figure 5-3c** for MREs containing $\Phi = 0, 9, 17, \text{and } 23\%$ as a function of magnetic field strength. Similarly to the shear storage modulus, the Young's modulus was also found to increase quadratically with increasing volume fraction of iron particles and applied magnetic field strength up to an $\approx 11\times$ increase for $\Phi = 23\%$. The large increase in Young's modulus $\left({}^{E(H)}/_{E(H=0)}\right)$ is an order of magnitude larger than that reported for rubber-like MREs subjected to the same range of magnetic field strengths and volume fractions of iron particles [2,3].

A single fit parameter equation for the Young's modulus can be determined by approximating the MRE as a perfectly elastic material that conserves volume such that $E = 3G'$ [10] resulting in the equation,

$$E(\Phi, H) = 2280\ (\text{Pa}) + 10500\ (\text{Pa})\Phi^2 + 3\alpha\Phi^2\mu_0 H^2 \quad (5\text{-}4)$$

The equation fits the experimental data well as shown in **Figure 5-3c** and exhibits deviation as the volume fraction of iron particles exceeds the estimated percolation threshold of $\Phi_c = 20\%$ for isotropic MREs [8].

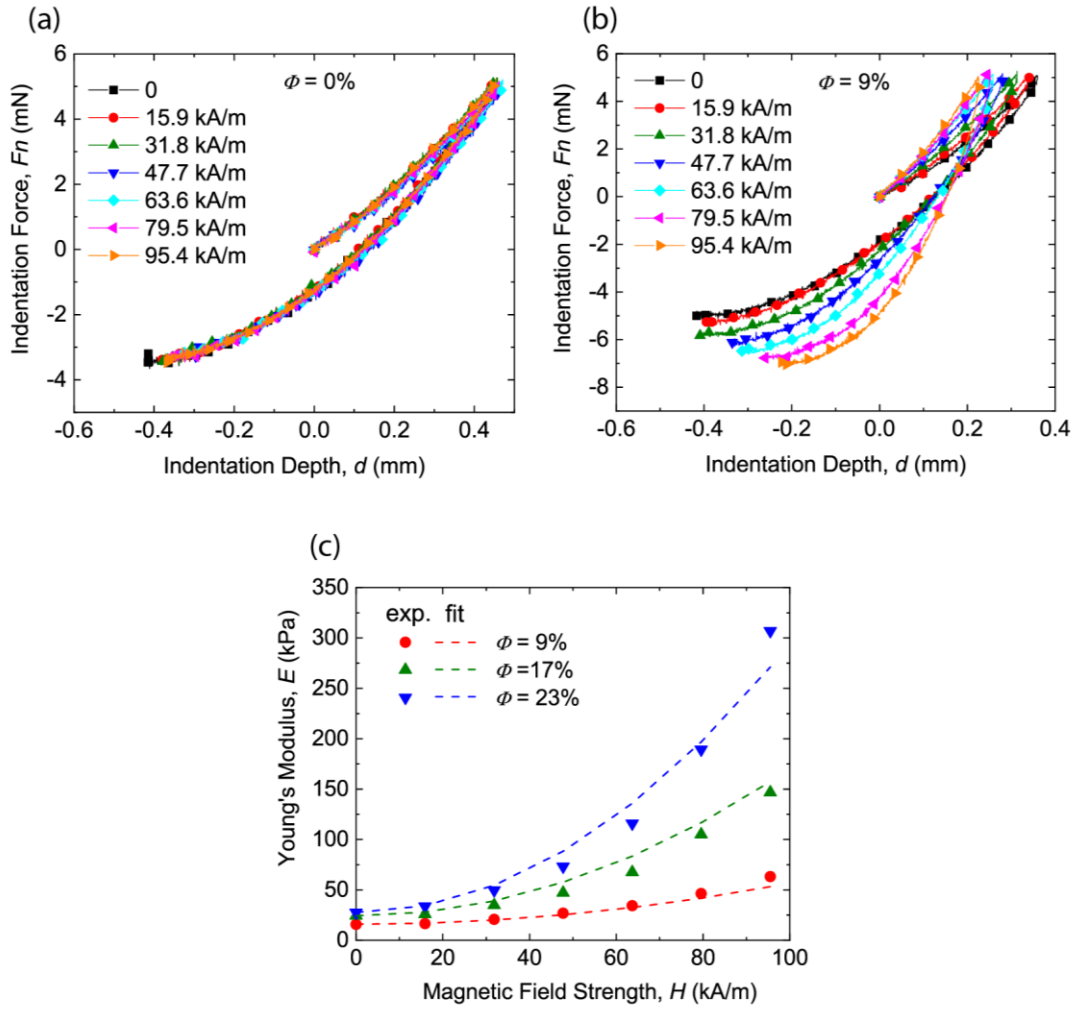


**Figure 5-3** Characterization of the magnetic field-dependent Young's modulus of ultrasoft MREs by compressive indentation. Indentation force vs. indentation depth curves for (a) $\Phi = 0\%$ and (b) $\Phi = 9\%$ for varying magnetic field strengths. (c) Comparison of the experimental (solid) and fit (dashed) increase in Young's modulus as a function of magnetic field strength for $\Phi = 9, 17, \text{and } 23\%$. Adapted from [3] 

### 5.4 The Effect of Magnetic Particle Concentration on the Surface Roughness

**Figure 5-4** shows the surface optical interferometry measurements of ultrasoft MREs as a function of volume fraction of iron particles and applied magnetic field strength. The root-mean-square (RMS) surface roughness, $R_q$, given by the equation [11],

$$R_q = \sqrt{\frac{1}{l_r}\int_0^{l_r} h(x)^2 dx} \tag{5-5}$$

where $l_r$ is the evaluation length, $h(x)$ is the height measured from the mean line at position $x$, was used as a quantitative measure of the surface roughness of the MREs. Surface profiles of the MREs show an increase in $R_q$ at both small and large length scales as a function of volume fraction of iron particles (**Figure 5-4a**) and magnetic field strength (**Figure 5-4b**). Interestingly, $R_q$ was found to also increase quadratically with increasing magnetic field strength (**Figure 5-4c**) up to an $\approx 7\times$ increase for $\Phi = 23\%$.

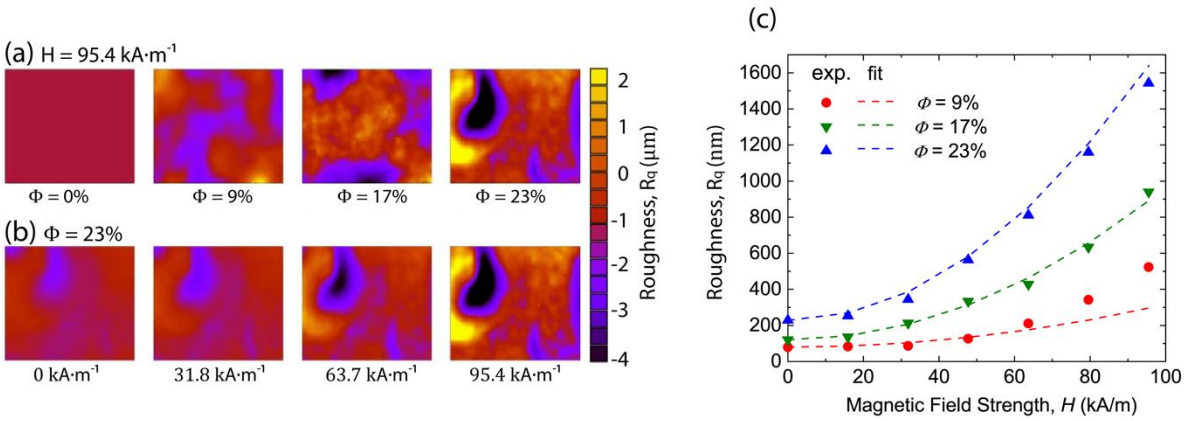


**Figure 5-4** Surface characterization of ultrasoft MREs by white light interferometry. (a) Surface profiles for $\Phi = 0, 9, 17, \text{and } 23\%$ subjected to a magnetic field strength of $H = 95.5\ \text{kA} \cdot \text{m}^{-1}$. (b) Surface profiles for $\Phi = 23\%$ at four magnetic field strengths. (c) Comparison of the experimental (solid) and fit (dashed) increase in RMS surface roughness as a function of magnetic field for $\Phi = 9,17 \text{ and } 23\%$. Adapted from [3] © IOP Publishing. Reproduced with permission. All rights reserved.

The magnetic field-dependent RMS surface roughness that originates from magnetic interaction between the magnetic particles [12], can be fit by the following equation,

$$R_q(\Phi, H) = 12\ (\text{nm}) + 4100\ (\text{nm})\Phi^2 + \beta\Phi^2 H^2 \quad (5\text{-}6)$$

where $\beta = 4100\ (\text{nm} \cdot \text{m}^2\text{A}^{-2})$ is the fit parameter. The surface roughness fit also agrees well with the experimental data suggesting similarities in the underlying mechanisms driving both the magnetic field-dependent changes in moduli (volumetric) and surface roughness (interfacial).

### 5.5 Tuning the Mechanical Properties of Ultrasoft MREs by Magnetic Field

The characterization of the magnetic field-dependent mechanical properties of ultrasoft MREs presented in this chapter provide the framework for utilization as dynamic substrata by the biomedical engineering community. While an MRE containing the largest volume fraction of iron particles ($\Phi = 23\%$) may seem like the perfect catch-all due to the wide range of moduli and surface roughness, limiting the volume fraction of iron particles also has benefits. The tunability of the shear storage modulus, Young's modulus, and RMS surface roughness, defined as $\Delta G'/\Delta H$, $\Delta E/\Delta H$, and $\Delta R_q/\Delta H$ respectively, can be modulated by the volume fraction of iron particles providing different tunability to the applied magnetic field as shown in **Figure 5-5**. As a quantitative example, at a magnetic field strength of $80\ \text{kA m}^{-1}$, an MRE containing $\Phi = 9\%$ ($\Phi = 23\%$) has a tunability of the shear storage modulus of $0.2\ \text{kPa} \cdot \text{m kA}^{-1}$ ($1.4\ \text{kPa} \cdot \text{m kA}^{-1}$), Young's modulus of $0.6\ \text{kPa} \cdot \text{m kA}^{-1}$ ($4.2\ \text{kPa} \cdot \text{m kA}^{-1}$) and RMS surface roughness of $14.6\ \text{nm} \cdot \text{m kA}^{-1}$ ($14.6\ \text{nm} \cdot \text{m kA}^{-1}$). The example provided highlights that MREs with a low

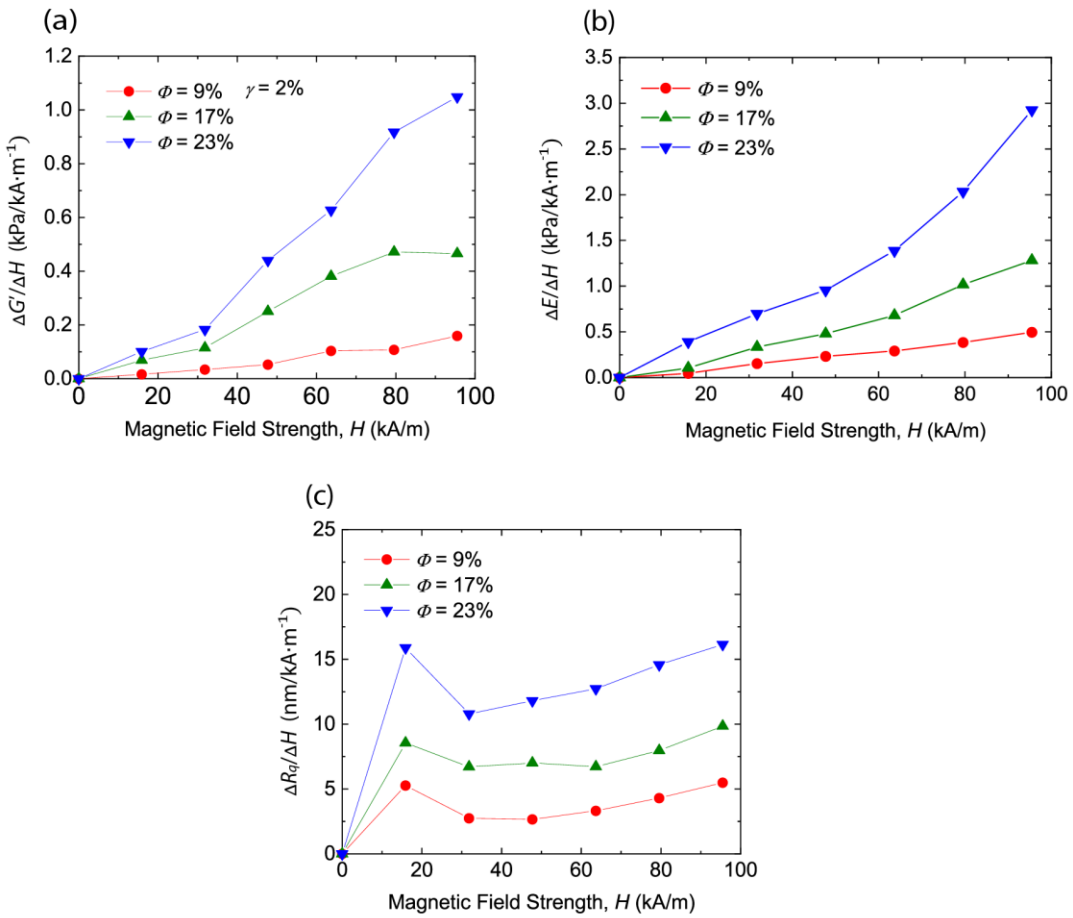


**Figure 5-5** Tunability of the (a) shear storage modulus, (b) Young's modulus, and (c) RMS surface roughness of MREs by magnetic field for $\Phi = 9, 17, \text{and } 23\%$. Adapted from [3] © IOP Publishing. Reproduced with permission. All rights reserved.

volume fraction of magnetic particles have low lower tunability, while conversely MREs with a high volume fraction of magnetic particles have higher tunability. Examples of biomedical applications utilizing the powerful tunability of MREs will be discussed in chapter 6.

## 5.6 Conclusions

This chapter discusses the effects of magnetic particle concentration on the magnetic field-dependent mechanical properties of ultrasoft MREs. The shear storage modulus at 2% shear strain was found to increase up to $\approx 16\times$ for ultrasoft MREs containing $\Phi = 9\%$ iron particles and up to $\approx 41\times$ for ultrasoft MREs containing $\Phi = 23\%$ iron particles. Similarly, the Young's modulus measured by compressive indentation showed an increase of up to $\approx 4\times$ ($\Phi = 9\%$) and $\approx 11\times$ ($\Phi = 23\%$). Surface interferometry revealed a monotonic increase in RMS surface roughness with increasing volume fraction $\Phi$ of magnetic particles and increasing magnetic field strength. The moduli and surface roughness can be fit to quadratic functions of the volume fraction of iron particles and magnetic field strength. These results coupled with the magnetic field control of MREs highlighted in chapter 4 provide the framework for utilizing ultrasoft MREs in a wide range of biological applications.

The results presented in this chapter have been published in the peer-reviewed journal Multifunctional Materials entitled "Magnetic Field Tuning of Mechanical Properties of Ultrasoft PDMS-based Magnetorheological Elastomers for Biological Applications" [13].

## References for Chapter 5


[1] M. Mayer, R. Rabindranath, J. Börner, E. Hörner, A. Bentz, J. Salgado, H. Han, H. Böse, J. Probst, M. Shamonin, G. J. Monkman, and G. Schlunck, *Ultra-Soft PDMS-Based Magnetoactive Elastomers as Dynamic Cell Culture Substrata*, PLoS ONE **8**, e76196 (2013).

[2] A. K. Bastola and M. Hossain, *A Review on Magneto-Mechanical Characterizations of Magnetorheological Elastomers*, Composites Part B: Engineering **200**, 108348 (2020).

[3] M. A. Cantera, M. Behrooz, R. F. Gibson, and F. Gordaninejad, *Modeling of Magneto-Mechanical Response of Magnetorheological Elastomers (MRE) and MRE-Based Systems: A Review*, Smart Mater. Struct. **26**, 023001 (2017).
[4] C. Storm, J. J. Pastore, F. C. MacKintosh, T. C. Lubensky, and P. A. Janmey, *Nonlinear Elasticity in Biological Gels*, Nature **435**, 191 (2005).
[5] N. A. Kurniawan, L. H. Wong, and R. Rajagopalan, *Early Stiffening and Softening of Collagen: Interplay of Deformation Mechanisms in Biopolymer Networks*, Biomacromolecules **13**, 691 (2012).
[6] M. R. Jolly, J. D. Carlson, and B. C. Muñoz, *A Model of the Behaviour of Magnetorheological Materials*, Smart Mater. Struct. **5**, 607 (1996).
[7] L. Chen and S. Jerrams, *A Rheological Model of the Dynamic Behavior of Magnetorheological Elastomers*, Journal of Applied Physics **110**, 013513 (2011).
[8] J.-P. Pelteret and P. Steinmann, *Magneto-Active Polymers: Fabrication, Characterisation, Modelling and Simulation at the Micro- and Macro-Scale* (De Gruyter, 2019).
[9] K. L. Johnson, *Contact Mechanics*, Porc. Inst. Mech. Eng. **223**, 254 (n.d.).
[10] R. G. Wells, *Tissue Mechanics and Fibrosis*, Biochimica et Biophysica Acta (BBA) - Molecular Basis of Disease **1832**, 884 (2013).
[11] D. J. Whitehouse, *Surfaces and Their Measurement* (HPS, London, 2002).
[12] R. Li, X. Li, P. Yang, J. Liu, and S. Chen, *The Field-Dependent Surface Roughness of Magnetorheological Elastomer: Numerical Simulation and Experimental Verification*, Smart Mater. Struct. **28**, 085018 (2019).
[13] A. T. Clark, A. Bennett, E. Kraus, K. Pogoda, A. Cēbers, P. Janmey, K. T. Turner, E. A. Corbin, and X. Cheng, *Magnetic Field Tuning of Mechanical Properties of Ultrasoft PDMS-Based Magnetorheological Elastomers for Biological Applications*, Multifunct. Mater. **4**, 035001 (2021).

# Chapter 6: Biomedical Applications of Ultrasoft MREs

## 6.1 Introduction

This chapter presents several biomedical applications of ultrasoft MREs along with a tissue regeneration application inspired by ultrasoft MREs. First, section 6.2 presents a wide range of biological tissue stiffnesses that can be mimicked using ultrasoft MREs and discusses cellular response to dynamic stiffening of an ultrasoft MRE substrate. Next, section 6.3 presents an extension of ultrasoft MREs into spatial 3D platforms by seeding cells within the polymer matrix. Finally, section 6.4 presents a novel technique for artificially recreating heterogenous cellular distributions through magnetic-field controlled cell motion in hydrogels with enhanced magnetic susceptibility.

## 6.2 Investigating Cellular Responses to Dynamic Mechanical Cues in 2D

### 6.2.1 Tunable Modulus Range of Ultrasoft MREs on the Biological Tissue Stiffness Continuum

The detailed characterization of the magnetic field-dependent changes in the mechanical properties of ultrasoft PDMS-based MREs presented in chapter 5 provides a means to utilize MREs as dynamic 2D cell culture substrates. **Figure 6-1** shows the tunable range of Young's moduli achieved by ultrasoft MREs superimposed on the biological tissue stiffness continuum [1]. As an example, MREs can be used to mimic the onset of diseases that have tissue pathologies typified by an increase in tissue stiffness (e.g.

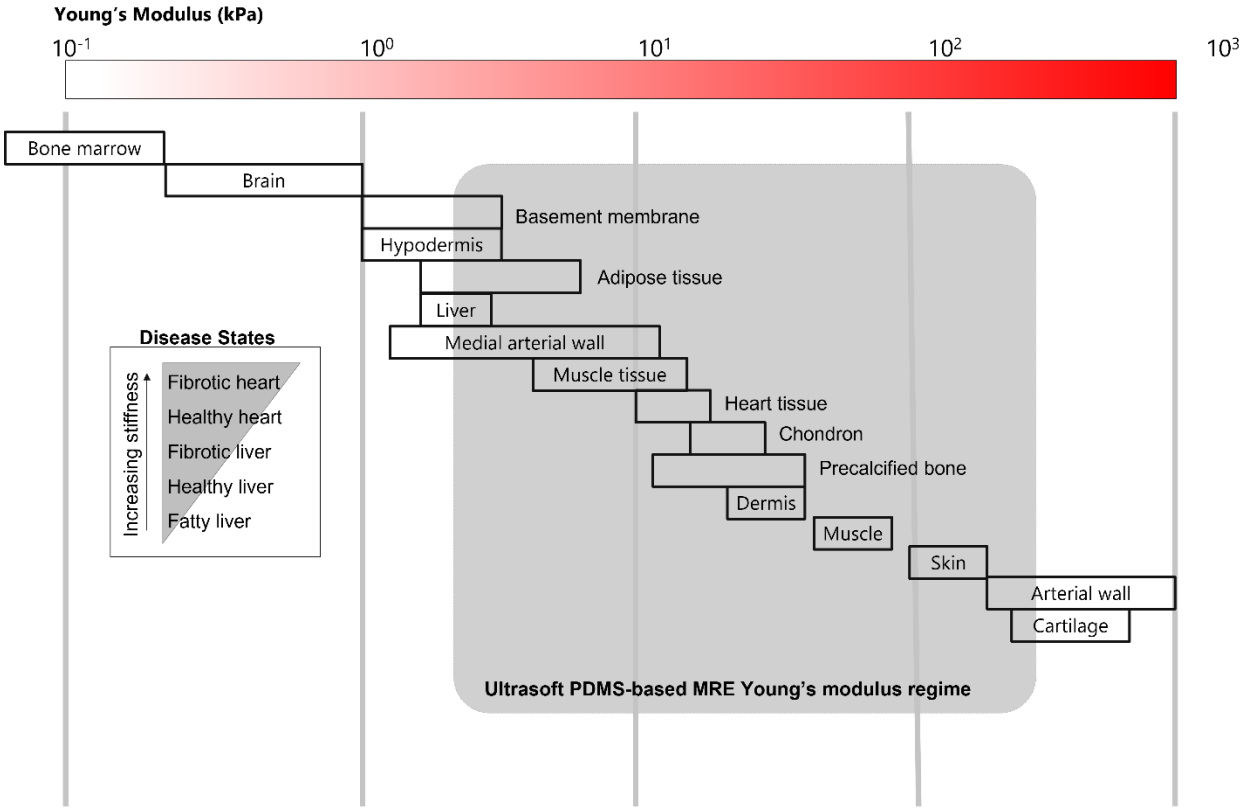


**Figure 6-1** Tunable range of magnetic field-dependent elastic moduli of ultrasoft PDMS-based MREs on the biological tissue stiffness continuum. Adapted from [1] © IOP Publishing. Reproduced with permission. All rights reserved.

atherosclerosis, non-alcoholic fatty liver disease). In particular, ultrasoft MREs can cover the whole range of Young's moduli of myocardium, the muscular tissue of the heart, before ($E \approx 10$ kPa) and after ($E \approx 35 - 70$ kPa) myocardial infarction (i.e. heart attack) [2]. An example to highlight the capabilities of MREs as 2D dynamic substrates is presented from a collaboration with Dr. Elise Corbin and Dr. Alexia Vite, who performed the biological work using ultrasoft MREs to study phenotype changes in cardiac fibroblasts in response to dynamic changes in substrate stiffness.

6.2.2 Stray Magnetic Field from a Rare-earth Permanent Magnet

Specifically for this work, rare-earth permanent magnets were selected as an ergonomic, and cost-effective means to apply a magnetic field to the MRE samples. The stray magnetic field from a cylindrical neodymium iron boride (NdFeB) magnet (1.26" diameter, 0.25" thick, CMS Magnets Inc.) was modeled using Finite Element Method Magnetics (FEMM) and the strength of the field at discrete locations was confirmed experimentally using a hall probe. **Figure 6-2a** shows the simulated stray magnetic field from the NdFeB magnet, which shows a decrease in magnetic field strength with increasing distance away from the top surface of the magnet. In order to tune the magnetic field strength at the MRE location, small non-magnetic spacers were place in-between the MRE and NdFeB magnet. **Figure 6-2b** shows the simulated (line) and experimentally (symbol)

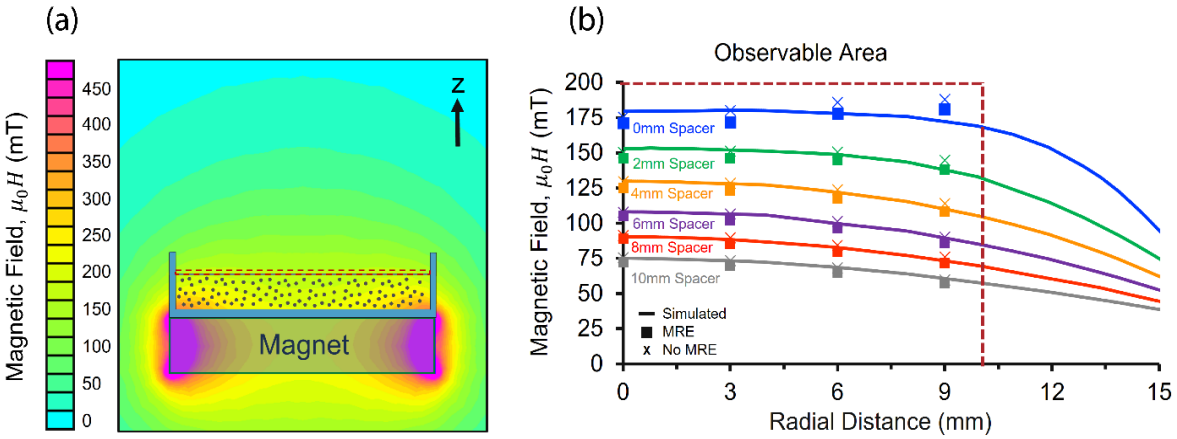


**Figure 6-2** Mapping the stray magnet from a NdFeB magnet. (a) FEMM model of the stray magnetic field from the magnet overlayed on a schematic of the MRE sample used in the biological experiments where a dashed box indicates the location of the cells on the surface of the MRE. (b) The z component of the magnetic field at the surface of the MRE sample as a function of radial distance for each specified spacer distance. Symbols ■ and × represent the magnetic field strength at the location of the cells measured experimentally using a hall probe with and without the MRE sample below, respectively. Adapted with permission from [4]. © 2019 American Chemical Society.

measured magnetic field strengths in the central region of the MRE used for biological measurements. As expected, the magnetic field strength along the axial direction decreases monotonically as the distance between the MRE and magnet increases providing a way to systematically tune the field strength using non-magnetic spacers.

### 6.2.3 Ultrasoft MRE Stiffening Promotes Myofibroblast Activation

Ultrasoft PDMS-based MREs were synthesized with a volume fraction $\Phi = 12\%$ of iron particles and coated with fibronectin to promote cell adhesion to the MRE surface. Cardiac fibroblasts were seeded onto the fibronectin coated MRE surface and their biological response to ramping up and ramping down the MRE stiffness were analyzed (**Figure 6-3**). Cardiac fibroblasts can exhibit a myofibroblast phenotype through mechanical activation, such as changes in stiffness of the extracellular matrix [3], which in this case is mimicked by the MRE. **Figure 6-3a** shows the percent of myofibroblast activation of cardiac fibroblasts as a function of MRE substrate stiffness and **Figure 6-3b** shows the representative images of cardiac fibroblasts on soft ($H = 0$) and stiff ($\mu_0 H = 175$ mT) MREs. Myofibroblast activation was found to monotonically increase from 4% activation up to 12% activation when the MRE Young's modulus of the MRE was increased from $E = 9.3$ kPa up to $E = 54.3$ kPa. Similarly, myofibroblast activation was seen to decrease from 12% down to 4% when the MRE Young's modulus of the MRE was decreased from $E = 54.3$ kPa down to $E = 9.3$ kPa.

The results presented in this section have been published in the peer-reviewed journal ACS Applied Materials and Interfaces entitled "Tunable and Reversible Substrate Stiffness Reveals a Dynamic Mechanosensitivity of Cardiomyocytes" [4].

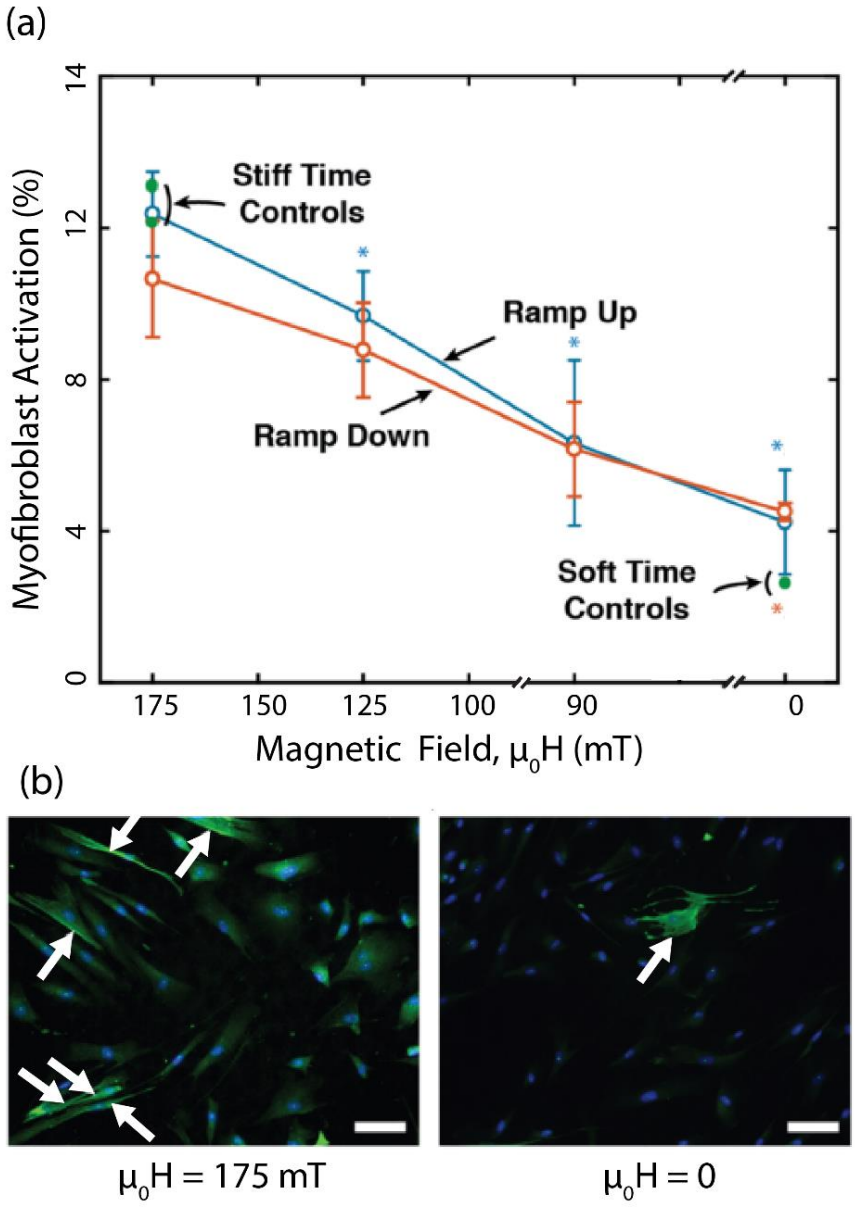


**Figure 6-3** MRE stiffening promotes myofibroblast activation. (a) Myofibroblast activation of cardiac fibroblasts in response to increasing and decreasing MRE stiffness by tuning externally applied magnetic field. * indicates significant difference. (b) Representative images of cardiac fibroblasts where the white arrows point to activated cells (i.e. myofibroblasts). Adapted with permission from [4]. © 2019 American Chemical Society.

### 6.3 Investigating Cellular Responses to Dynamic Mechanical Cues in 3D

Traditionally, cellular response to mechanics of their local microenvironment, known as the extracellular matrix (ECM), has been examined in 2D, but most nonepithelial cell types are fully surrounded by ECM *in vivo* [5,6]. MREs can be extended from 2D to 3D by using hydrogels seeded with both cells and magnetic particles allowing for direct interrogation of dynamic changes in 3D substrate stiffness. An example to highlight this application is presented from a collaboration with graduate student Kiet Tran who performed the synthesis and characterization of 3D hydrogel-based MREs along with the biological experiments.

Normal human astrocytes (NHAs) were seeded at a density of $1 \times 10^6$ cells/mL into 5 mg/mL collagen hydrogels containing 5% carbonyl iron microparticles particles (MP) by weight. The concentration of iron particles was intentionally chosen due to the high viability of cells and to tune the hydrogel stiffness from $G'_{(H=0)} = 0.8$ kPa to $G'_{(H=7{,}700\ \mathrm{Oe})} = 8.5$ kPa, which represents a sufficient increase to investigate changes in cell morphology. Schematics of the experiments are shown in **Figure 6-4(a-c)**. After 11 hours, cells were fixed and stained with DAPI and phalloidin for imaging (**Figure 6-4(d-f)**). Cell morphology was quantified by measuring cell area and cell shape index displayed in **Figure 6-4g** and **6-4h**, respectively. The two controls (**Fig 6-4a** and **6-4b**) were used to compare the effect of the applied magnetic field without the inclusion of magnetic particles, and the effect of magnetic particles without any magnetic field applied on the cells, respectively. No significant difference in cell area or cell shape index is observed between the two controls. Cells seeded with 5% magnetic particles by weight and in $H = 7{,}700$ Oe showed a decrease in cell area and an increase in cell shape index indicating that the cells

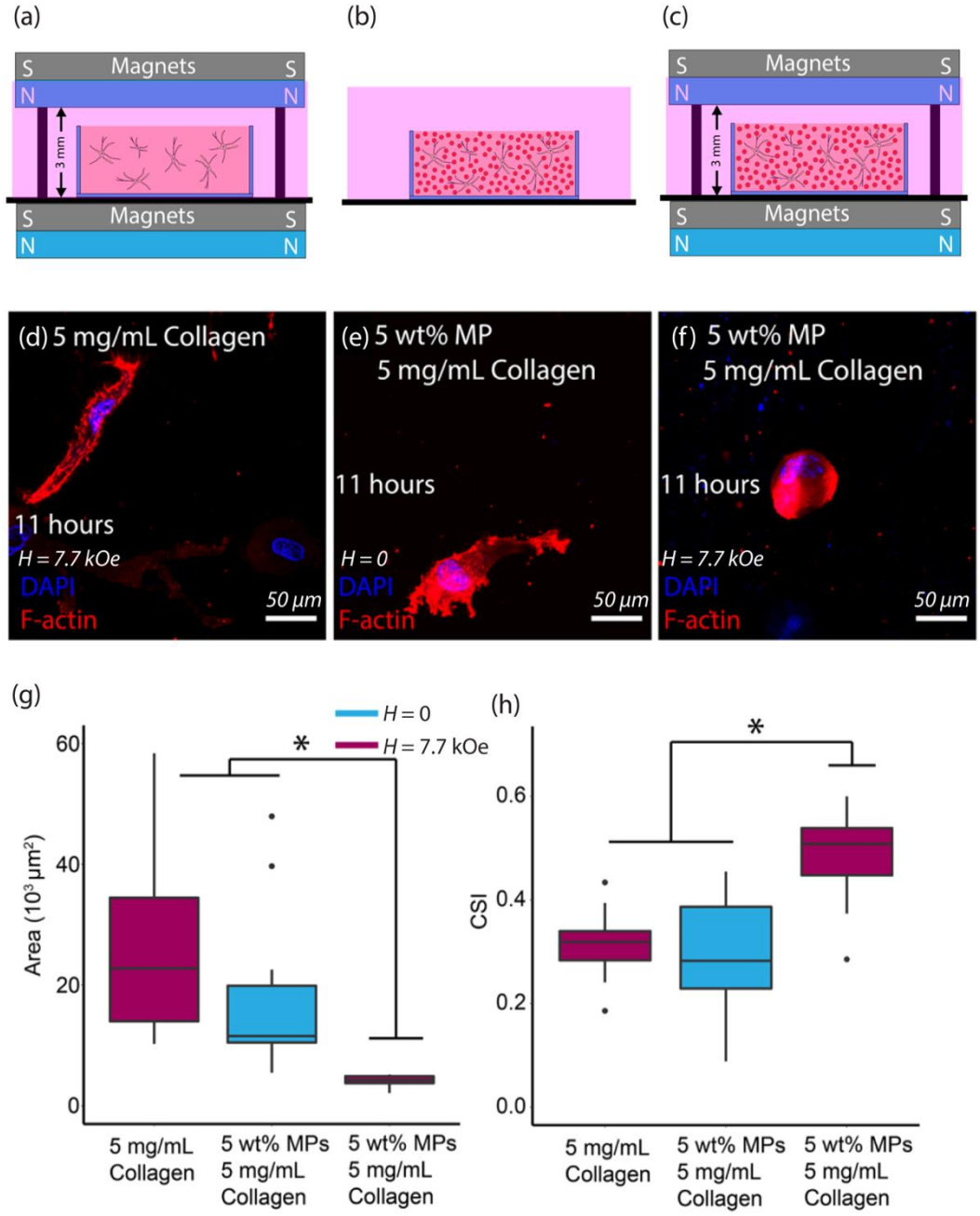


**Figure 6-4** Probing cellular response in 3D using ultrasoft hydrogel-based MREs. (a-c) Schematics of three cell experiments with control (a) 5mg/mL collagen in $H = 7{,}700$ Oe, control (b) 5mg/mL collagen and 5% iron microparticles by weight in $H = 0$ and (c) 5 mg/mL collagen and 5% iron microparticles by weight in $H = 7{,}700$ Oe. (d-f) Representative images of the normal human astrocytes cells after 11 hours for the three conditions. Quantification of (g) cell area and (h) cell shape index (CSI) at 11 hours. $*P < 0.05$, n=15 per condition. Adapted with permission from [7]. © 2021 American Chemical Society.

became more circular. These results are consistent with previous studies using 3D stiff hydrogels [7,8] that show decreased cell spreading due to inability of cells to deform the ECM in 3D highlighting the dynamic capability of ultrasoft MREs in 3D.

The results presented in this section have been published in the peer-reviewed journal ACS Applied Materials and Interfaces entitled "Dynamic Tuning of Viscoelastic Hydrogels with Carbonyl Iron Microparticles Reveals the Rapid Response of Cells to Three-Dimensional Substrate Mechanics" [9].

### 6.4 Artificially Creating Heterogenous Cellular Distributions using Gradient Magnetic Fields

The magnetic field-dependent motion of magnetic particles within the polymer matrix of MREs presented in chapter 4 inspired an exciting approach to position diamagnets, such as living cells, in 3D for engineering complex tissues gradients. In this section, an example of using a gradient magnetic field to create heterogeneous distributions of diamagnetic objects (e.g. beads, cells) in 3D hydrogels is presented from a collaboration with graduate student Hannah Zlotnick who performed most of the experiments. As mentioned in chapter 2, diamagnetic effects are weak and therefore the magnetic force imposed on a diamagnetic object in a gradient magnetic field are usually much smaller than the mechanical forces of the hydrogel environment such as gravity and drag. The diamagnetic effects can be enhanced without altering the diamagnetic cells by enhancing the magnetic susceptibility of the cell-containing solution. Here, a commercially available gadolinium-based magnetic contrast agent, commonly used for magnetic resonance

imaging (MRI), was used to enhance the magnetic susceptibility of the hydrogel and was subsequently washed out after the cells are positioned and the hydrogel is crosslinked.

First, a proof of concept was developed using COMSOL to simulate the gradient magnetic field generated by a NdFeB magnet. Spatial derivates of the magnetic field were calculated from the COMSOL model and used as input for a model consisting of diamagnetic beads suspended in a hydrogel solution. The equation of motion for each bead was solved numerical using MATLAB to determine their time dependent trajectories within the aqueous solution. Next, using the model as guidance, the time-dependent trajectory of diamagnetic polystyrene beads subjected to a gradient magnetic field was imaged experimentally. Lastly, the diamagnetic polystyrene beads were replaced with mesenchymal stromal cells (MSCs) and successfully patterned in 3D.

This novel concept was conceived by co-inventors Hannah Zlotnick, Dr. Robert Mauck, Andy Clark, and Dr. Xuemei Cheng and is currently being reviewed by the United States Patent Office under application number 17/229,829.

### 6.4.1 Proof of Concept using Numerical Simulations

**Figure 6-5a** shows the free body diagram of a diamagnetic object in a hydrogel precursor subjected to a gradient magnetic field along predominately along the z direction. The equation of motion for the diamagnetic object is given by,

$$m\mathbf{a} = \mathbf{F}_{\text{magnetic}} + \mathbf{F}_{\text{drag}} + \mathbf{F}_{\text{bouyancy}} + \mathbf{F}_{\text{gravity}} \tag{6-1}$$

$$\mathbf{F}_{\text{magnetic}} = \left(\frac{V\Delta\chi}{\mu_0}\mathbf{B}\cdot\boldsymbol{\nabla}\right)\mathbf{B} \tag{6-2}$$

$$\mathbf{F}_{\text{drag}} = 6\pi r\eta f_D\,\mathbf{v} \tag{6-3}$$

$$\mathbf{F}_{\text{bouyancy}} = V\rho_f g\hat{\boldsymbol{z}} \tag{6-4}$$

$$\mathbf{F}_{\text{gravity}} = -V\rho_{obj}g\hat{\mathbf{z}} \tag{6-5}$$

where m is the mass, **a** is the acceleration, $V$ is the volume of the diamagnetic object, $\Delta\chi$ is the difference in susceptibility between the object and the hydrogel precursor, $\mu_0$ is the permeability of free space, B is the magnetic flux density, $r$ is the radius of the (spherical) object, $\eta$ is the viscosity of the hydrogel precursor, $f_D$ is the drag coefficient, **v** is the velocity, $g$ is gravity, $\rho_f$ and $\rho_{obj}$ are the densities of the fluid and object respectively. The values for the constants used in the model are listed in **Table 6-1**.

| Variable | Description | Units | Value |
|---|---|---|---|
| $V$ | Object volume | $\mu m^3$ | 523.6 |
| $\Delta\chi$ | Magnetic susceptibility of object - Magnetic susceptibility of fluid | none | $\chi_o = -0.75 \times 10^{-5}$ $\chi_f = 6.4 \times 10^{-5}$ |
| $B$ | Magnetic flux density | T | Input from COMSOL |
| $\mu_0$ | Magnetic permeability of free space | kg m $A^{-2}$ $s^{-2}$ | $4\pi \times 10^{-7}$ |
| $r$ | Radius of object | μm | 5 |
| $\eta$ | Dynamic viscosity of hydrogel precursor | cP | 10 |
| $f_D$ | Drag coefficient | none | 1 |
| **v** | Velocity of object | m $s^{-1}$ | Calculated |
| m | Mass of object | g | $5.5 \times 10^{-7}$ |
| $\boldsymbol{a}$ | Acceleration of object | m $s^{-2}$ | Calculated |
| $\rho_f$ | Density of fluid | g $mL^{-1}$ | 1.06 |
| $\rho_o$ | Density of object | g $mL^{-1}$ | 1.05 |
| g | Gravitational acceleration | m $s^{-2}$ | 9.8 |

**Table 6-1** Variables used in the numerical simulation. The fluid is the Gd containing hydrogel solution prior to crosslinking.

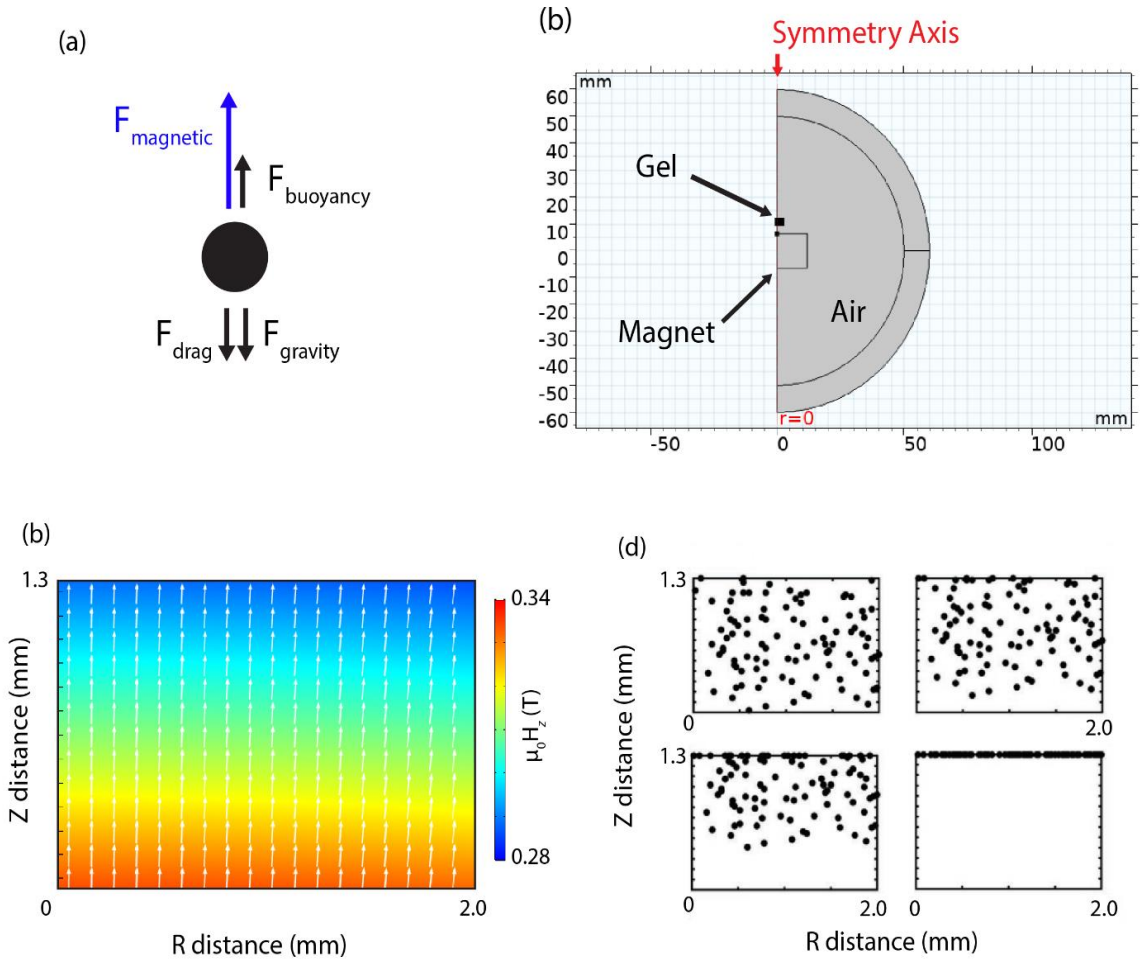


**Figure 6-5** Proof of concept using numerical simulations for creating spatial gradients of diamagnetic particles in a hydrogel solution using a gradient magnetic field. (a) Free-body diagram of the forces acting on a diamagnetic particle in a hydrogel. (b) Modeled 2D axi-symmetric geometry of NdFeB magnet, hydrogel, and surrounding air environment. (c) Simulated stray magnetic field within the hydrogel. (d) MATLAB simulation of the trajectory of diamagnetic particles within a hydrogel as a function of time. (b,c) Adapted from [10] with permission granted by author Hannah Zlotnick.

An axially magnetized, cylindrical NdFeB magnet was selected as the field application device due to its large field strength, low cost, and ergonomic size. To numerical solve equation 6-1, the magnetic field strength and its spatial derivative within the hydrogel is required. COMSOL was used to model the stray field from a cylindrical,

axially magnetized NdFeB magnet having diameter $15/16$" and $1/2$ "thick, remanent flux density $B_{r\,max} = 13{,}200$ Gauss (K&J Magnetics, Inc.). The cylindrical magnet and hydrogel were modeled using the 2D axi-symmetric interface within COMSOL as shown in **Figure 6-5b**. The magnetic field (**Figure 6-5c**) and its spatial derivative was computed at each point on a 20 μm grid throughout a 2D cross section of the cylindrical hydrogel sample having radius 2 mm and height 1.3 mm and used as input for equation 6-1. MATLAB was used to numerically solve equation 6-1 to determine the trajectories of one hundred diamagnetic spheres with properties listed in **Table 6-1**. **Figure 6-5d** shows the resulting positions of the diamagnetic particles at $t = 0, 3, 5$ and 10 minutes. As expected, the diamagnetic particles move towards the top of the hydrogel sample due to the dominate diamagnetic force and after ten minutes all the particles reach the top.

6.4.2 Engineering Gradients of Living Cells in 3D Hydrogels

Next, using the simulation as a guide, un-altered MSCs (bovine, passage 2, 200 million cells $mL^{-1}$) were positioned in a 3D hydrogel to asses viability of creating heterogeneous distributions living cells. MSCs were seeded into a 3D hydrogel containing small ($R = 0.5$ μm) gel marking beads, which due to their small size have negligible magnetic force and thus remain stationary. **Figure 6-6a** shows the results of the 3D magneto-patterning of the MSCs after $t = 0, 2, 5$ and 10 minutes of exposure to the gradient magnetic field matching the simulated field shown in **Figure 6-5**. Five regions of the 3D hydrogel were defined as shown in **Figure 6-6b** and the distribution of cells was quantified (**Figure 6-6c**). Initially, the cells were evenly distributed between the five regions. Exposure to a gradient magnetic field causes the diamagnetic MSCs to move

upwards towards the top of the hydrogel construct (region one). After ten minutes, there are ≈ 30% of the MSCs in region one, and only ≈ 5% in regions five and a clear gradient in the cell density within the hydrogel is observed.

The results presented in this section have been published in the peer-reviewed journal Advanced Materials entitled "Magneto-Driven Gradients of Diamagnetic Objects for Engineering Complex Tissues" [10]

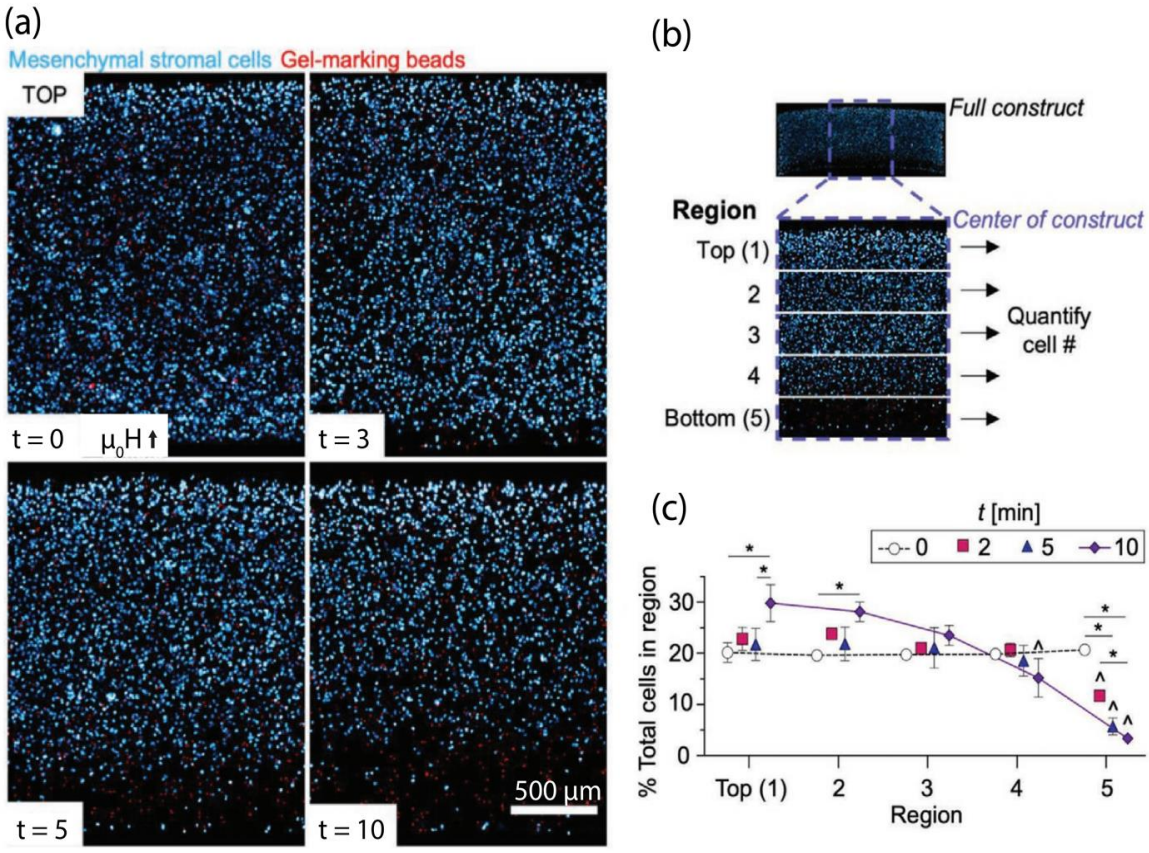


**Figure 6-6** Creating a gradient distribution of cells within a hydrogel using a gradient magnetic field. (a) Distribution of mesenchymal stromal cells (blue) and gel-marking beads (red) within a hydrogel subjected to a gradient magnetic field for 0, 3, 5 and 10 minutes. Adapted from [10] with permission granted by author Hannah Zlotnick.

## References for Chapter 6


[1] A. T. Clark, A. Bennett, E. Kraus, K. Pogoda, A. Cēbers, P. Janmey, K. T. Turner, E. A. Corbin, and X. Cheng, *Magnetic Field Tuning of Mechanical Properties of Ultrasoft PDMS-Based Magnetorheological Elastomers for Biological Applications*, Multifunct. Mater. **4**, 035001 (2021).

[2] P. A. Janmey and R. T. Miller, *Mechanisms of Mechanical Signaling in Development and Disease*, J. Cell Sci. **124**, 9 (2011).

[3] A. A. Gibb, M. P. Lazaropoulos, and J. W. Elrod, *Myofibroblasts and Fibrosis*, Circ. Res. **127**, 427 (2020).

[4] E. A. Corbin, A. Vite, E. G. Peyster, M. Bhoopalam, J. Brandimarto, X. Wang, A. I. Bennett, A. T. Clark, X. Cheng, K. T. Turner, K. Musunuru, and K. B. Margulies, *Tunable and Reversible Substrate Stiffness Reveals a Dynamic Mechanosensitivity of Cardiomyocytes*, ACS Appl. Mater. Interfaces **11**, 20603 (2019).

[5] J. Fu, Y.-K. Wang, M. T. Yang, R. A. Desai, X. Yu, Z. Liu, and C. S. Chen, *Mechanical Regulation of Cell Function with Geometrically Modulated Elastomeric Substrates*, Nat. Methods **7**, 733 (2010).

[6] B. M. Baker and C. S. Chen, *Deconstructing the Third Dimension – How 3D Culture Microenvironments Alter Cellular Cues*, J. Cell Sci. jcs.079509 (2012).

[7] S. R. Caliari, S. L. Vega, M. Kwon, E. M. Soulas, and J. A. Burdick, *Dimensionality and Spreading Influence MSC YAP/TAZ Signaling in Hydrogel Environments*, Biomaterials **103**, 314 (2016).

[8] O. Chaudhuri, L. Gu, D. Klumpers, M. Darnell, S. A. Bencherif, J. C. Weaver, N. Huebsch, H. Lee, E. Lippens, G. N. Duda, and D. J. Mooney, *Hydrogels with Tunable Stress Relaxation Regulate Stem Cell Fate and Activity*, Nat. Mater. **15**, 326 (2016).

[9] K. A. Tran, E. Kraus, A. T. Clark, A. Bennett, K. Pogoda, X. Cheng, A. Cēbers, P. A. Janmey, and P. A. Galie, *Dynamic Tuning of Viscoelastic Hydrogels with Carbonyl Iron Microparticles Reveals the Rapid Response of Cells to Three-Dimensional Substrate Mechanics*, ACS Appl. Mater. Interfaces **13**, 20947 (2021).

[10] H. M. Zlotnick, A. T. Clark, S. E. Gullbrand, J. L. Carey, X. M. Cheng, and R. L. Mauck, *Magneto-Driven Gradients of Diamagnetic Objects for Engineering Complex Tissues*, Adv. Mater. **32**, 2005030 (2020).

## Chapter 7: Conclusions

In this dissertation, the author reports a comprehensive investigation of the magnetic and mechanical properties of ultrasoft magnetorheological elastomers (MREs) and their biomedical applications. Ultrasoft PDMS-based MREs (Young's modulus $E$~kPa) were synthesized by mixing commercial polymer Sylgard™ 527 with magnetically soft carbonyl iron powder at volume fractions of $\Phi = 3, 23, 30$ and 40%. Harder MREs with $E$ ranging over two orders of magnitude were synthesized by adding different amounts of a harder Sylgard™ 184 polymer.

The effects of polymer stiffness and magnetic particle concentration on the magnetic properties of MREs were investigated by magnetometry measurements at temperatures between 300 K and 2 K, in combination of theoretical modeling. Magnetic hysteresis loops of ultrasoft MREs exhibit a characteristic pinched loop shape with almost zero remanence and loop widening at intermediate fields. The observed loop widening decreases monotonically with increasing polymer stiffness, which was tuned by either varying polymer composition or by varying temperature. The hysteresis loops measured in the same ultrasoft MRE sample at temperatures below 230 K are identical to the room temperature hysteresis loops from rubber-like MREs synthesized with stiffer polymers and the same $\Phi$. Furthermore, the observed loop widening decreases as $\Phi$ increases because the particles are closer together, resulting in less available space to move. A two-dipole model shows that the observed loop widening arises from a bistability of inter-particle displacements along the applied magnetic field direction. The model, while simple in

nature, produces calculated magnetic hysteresis loops that quantitatively match the loop widening trends observed experimentally for MREs with varying polymer stiffnesses.

Magnetic field-dependent shear rheology, compressive indentation, and interferometry were employed to explore the effect of magnetic particle concentration on the mechanical properties of ultrasoft MREs. Increasing the iron particle volume fraction $\Phi$ of the ultrasoft MREs from 0 to 23% results in an increase in the shear storage, Young's modulus, and root-mean-square surface roughness by $\approx 41\times, 11\times,$ and $11\times$, respectively, at $H = 95.5$ kA/m (1,200 Oe). The moduli and surface roughness of ultrasoft MREs can be fit by quadratic functions of $\Phi$ and $H$. These equations provide guidance for application of ultrasoft MREs in mimicking the dynamic cellular environment for a wide range of biological systems.

Applications of ultrasoft MREs as dynamic 2D and 3D platforms for mimicking dynamic mechanical changes in the cellular microenvironment were explored. Cardiac fibroblasts cultured on top of an ultrasoft MRE substrate showed increased (decreased) activation to myofibroblasts as the stiffness of the MRE was increased (decreased). Cellular response to dynamic mechanical stimuli in 3D was investigated using ultrasoft hydrogels seeded with normal human astrocytes and magnetic particles, which showed a decrease in cell area and cell shape index as the stiffness of the MRE increased. In addition, the magnetic field-dependent motion of living cells within hydrogels was utilized to successfully engineer heterogenous cellular distributions in 3D for applications in tissue regeneration.

## List of Publications

1. **A.T. Clark**, D. Marchfield, Z. Cao, T. Dang, N. Tang, D. Gilbert, E.A. Corbin, K.S. Buchanan and X.M. Cheng, *The Effect of Polymer Stiffness on Magnetization Reversal of Magnetorheological Elastomers*, (2022), APL Mater. **10** 041106

2. **A.T. Clark**, A.I. Bennet, E. Kraus, K. Pogoda, A. Cēbers, P.A. Janmey, K.T. Turner, E.A. Corbin and X.M. Cheng, *Magnetic Field Tuning of Mechanical Properties of Ultrasoft PDMS-based Magnetorheological Elastomers for Biological Applications*, (2021) Multifunct. Mater. 4 035001

3. Y. Wang, X. Wang, **A.T. Clark**, H. Chen, X.M. Cheng, J.W. Freeland and J.Q. Xiao, *Probing Exchange Bias at the Surface of a Doped Ferrimagnetic Insulator*, (2021) Phys. Rev. Materials 5, 074409

4. R.J. Warozha, A.A. Wilson, B.F. Donovan, **A.T. Clark**, X.M. Cheng, L. An, E. Lee, X. Liu and G. Feng, *Confined Transducer Geometries to Enhance Sensitivity to Thermal Boundary Conductance in Frequency-Domain Thermoreflectance Measurements*, (2021) IPACK2021-66842, V001T08A001; 10p

5. K.A. Tran, E. Kraus, **A.T. Clark**, A.I. Bennett, K. Pogoda, X.M. Cheng, A. Cēbers, P.A. Janmey and P.A. Galie, *Dynamic Tuning of Viscoelastic Hydrogels with Carbonyl Iron Microparticles Reveals the Rapid Response of Cells to Three-Dimensional Substrate Mechanics*, (2021) ACS Appl. Mater. Interfaces 13, 18, 20947-20959

6. H.M. Zlotnick, **A.T. Clark**, S.E. Gullbrand, J.L. Carey, X.M. Cheng and R.L. Mauck, *Magneto-driven Gradients of Diamagnetic Objects for Engineering Complex Tissues*, (2020) Adv. Mater. 32, 2005030

7. E.A. Corbin, A. Vite, E.G. Peyster, M. Bhoopalam, J. Brandimarto, X. Wang, A.I. Bennett, **A.T. Clark**, X.M. Cheng, K.T. Turner, K. Musunuru and K.B. Margulies, *Tunable and Reversible Substrate Stiffness Reveals a Dynamic Mechanosensitivity of Cardiomyocytes*, (2019) ACS Appl. Mater. Interfaces 11, 23, 20603-20614

8. D. Zhou, J. Hao, **A.T. Clark**, K. Kim, L. Zhu, X.M. Cheng and B. Li, *Sono-Assisted Surface Energy Driven Assembly of 2D Materials on Flexible Polymer substrates: A Green Assembly Method Using Water*, (2019) ACS Appl. Mater. Interfaces 11, 33458-33464